Charles University

Faculty of Science

Study programme: Biology

Branch of study: Genetics, Molecular Biology and Virology

Bc. Martina Pružincová

Stability of protein complexes in the cytoskeleton of the eukaryotic flagellum

Stabilita proteinových komplexů cytoskeletu eukaryotického bičíku

Diploma thesis

Supervisor: Mgr. Vladimír Varga, Ph.D.

Prague, 2019

Prohlášení:

Prohlašuji, že jsem závěrečnou práci zpracovala samostatně a že jsem uvedla všechny použité informační zdroje a literaturu. Tato práce ani její podstatná část nebyla předložena k získání jiného nebo stejného akademického titulu.

V Praze, 12.08.2019

Podpis

Acknowledgements

V prvom rade by som chcela veľmi poďakovať svojmu školiteľovi Vladovi, za to, že mi umožnil byť súčasťou svojho tímu a že som vďaka nemu mohla nahliadnuť do sveta vedy. Za jeho prístup a rady. Ďakujem za to, že som sa toho mohla veľa naučiť a že som zistila, koľko sa toho ešte musím a chcem naučiť.

Ďakujem aj všetkým členom laboratória za podporu a pomoc, Peťovi za rozhovory. A špeciálne ďakujem Ludkovi, za to, že mi bol ochotný venovať čas a za ten super script!

Poďakovanie partí aj Dr. Dean, za venované reagencie.

Na záver musím poďakovať svojej rodine za veľkú podporu a ohľaduplnosť. Majke ďakujem, za mnohé naučené a Tomovi za mnohé pochopené. Ďakujem, že si stál pri mne a motivoval ma ísť ďalej.

Ďakujem

Abstract

The cilium/flagellum is a complex organelle protruding from the cell body and functioning in motility, sensing, and signalling. It is composed of hundreds of protein constituents, the majority of which comprise the flagellar cytoskeleton – the microtubule-based axoneme.

Because the flagellum lacks ribosomes, its protein constituents have to be imported from the cell body and delivered to proper locations. Moreover, these proteins have to retain their function over a considerable length of time, despite the mechanical stress caused by flagellar beating and due to environmental exposure. This raises the question whether and where protein turnover occurs.

Previously, it was established that *Chlamydomonas reinhardtii* flagella are dynamic structures (Marshall & Rosenbaum, 2001). In contrast, in the *Trypanosoma brucei* flagellum axonemal proteins are remarkably stable (Vincensini *et al.*, 2018). However, the questions of axonemal assembly and stability were so far investigated only for a small number of proteins and during relatively short periods. Moreover, in these experiments expression of studied proteins was controlled by non-native regulatory elements.

To elucidate the site of incorporation of proteins from all major axonemal complexes and to find out if and where the protein turnover occurs, *T. brucei* as a model organism was selected. *T. brucei* is capable of homology recombination, which enables rapid protein tagging in their endogenous loci. Examined proteins were fused to two tags – a fluorescent protein to monitor total protein in the cell and the HaloTag enabling labelling of the protein molecules present in the cell at a particular time and monitor their behaviour thereafter.

These experiments confirmed that the addition of constituents of all major axonemal complexes to a growing axoneme occurs exclusively at its distal end. Surprisingly, the turnover of these proteins in mature flagella of *T. brucei* was observed. This turnover happens around cytokinesis and exclusively affects a short region at the distal end of the flagellum. Finally, the data indicate differences in relative cytoplasmic pools of the studied axonemal proteins. In conclusion, this work provides a systematic analysis of the axonemal growth and turnover, contribution to the knowledge of these aspects of basic flagellar biology.

Keywords: cilium, flagellum, axoneme, turnover, protein incorporation**,** *Trypanosoma brucei*, HaloTag

Abstrakt

Cília/bičík je komplexná organela vystupujúca z tela bunky, ktorá môže mať niekoľko funkcií, ako napríklad pohybovú, senzorickú alebo signálnu. Bičík je zostavený zo stoviek proteínov, ktorých väčšina tvorí kostru – mikrotubulárnu axonému.

Pretože bičík neobsahuje ribozómy, proteíny, ktoré sa podieľajú na jeho stavbe a funkcii, musia byť dovážané z tela bunky a inkorporované na správne pozície. Navyše, tieto proteíny si musia zachovávať svoju funkciu počas dlhého obdobia, a to napriek tomu, že sú vystavené mechanickému a environmentálnemu stresu. Tieto skutočnosti vzbudzujú otázku, či a kde dochádza v bičíku k výmene proteínov.

Predchádzajúce štúdie bičíkov na *Chlamydomonas reinhardtii* prezentovali, že bičík je dynamická štruktúra (Marshall & Rosenbaum, 2001). Naopak, štúdie na *Trypanosoma brucei* ukázali, že bičíky tohto organizmu sú pozoruhodne stabilné (Vincensini *et al.*, 2018). Avšak to, akým spôsobom sa bičík vytvára a stabilizuje, bolo doteraz skúmané iba na veľmi malom počte proteínov a iba v krátkych časových intervaloch. Navyše, tieto experimenty využívali expresiu študovaných proteínov s neprirodzenými regulačnými mechanizmami.

Na objasnenie detailov spôsobu fungovania proteínovej obmeny v bičíku bola v tejto práci použitá *T. brucei*. Jedným z dôvodov výberu tohto modelového organizmu bolo to, že *T. brucei* má schopnosť homologickej rekombinácie génov, čo umožňuje rýchlu produkciu značených proteínov. Na označenie týchto proteínov boli použité fluorescenčné značky, ktorými bolo pozorované celkové množstvo proteínu v bunke a takzvaný HaloTag, ktorý umožňoval označenie proteínov nachádzajúcich sa v bunke v jedinom konkrétnom čase.

Prezentované experimenty ukázali, že proteíny všetkých hlavných axonemálnych komplexov sa zabudovávajú výlučne zo vzdialeného konca bičíka. Jedným z prekvapivých zistení tejto práce bolo pozorovanie proteínovej obmeny vo vyzretom bičíku. K tejto obmene dochádza počas cytokinézy a to výlučne v oblasti na vzdialenom konci bičíka. Ďalším zaujímavým pozorovaním je, že skúmané axonemálne proteíny majú rozlične veľké cytoplazmické zásoby. V závere táto práca predstavuje systematickú analýzu rastu a proteínovej obmeny hlavných axonemálnych komplexov a prispieva tak k lepšiemu pochopeniu biológie bičíka.

Kľúčové slová: cília, bičík, axonéma, proteínová obmena, inkorporácia proteínov, *Trypanosoma brucei*, HaloTag

Table of Contents

List of abbreviations

ACS1	axonemal capping structure 1
ATP	adenosine triphosphate
BB	basal body
CA	central apparatus
CaM	Calmodulin
cl	clone
CP	central pair
CSC	Spoke Associated Complex
DCR2	Nexin-dynein regulatory complex 2
DMSO	dimethyl sulfoxide
ELFO	electrophoresis
FAZ	flagellum attachment zone
FC	flagella connector
FRAP	fluorescence recovery after photobleaching
gDNA	genomic DNA
HAT	human African trypanosomiasis
HH	Hedgehog
IDA	inner dynein arms
IFT	intraflagellar transport
KD	knock down
kDNA	kinetoplast DNA
LECA	Last Eukaryotic Common Ancestor
MIPs	microtubular inner proteins
mNG	mNeonGreen
MT	microtubule
MTD	microtubular doublets
MTT	mitotracker
nDNA	nuclear DNA
N-DRC	nexin-dynein regulatory complex
ODA	outer dynein arms
ORF	open reading frame
pBLAST	protein Basic Local Alignment Tool
PCD	primary ciliary dyskinesia
PCR	Polymerase chain reaction
pDNA	plasmid DNA

PFR	paraflagellar rod
PFs	protofilaments
PKD	polycystic kidney disease
POI	protein of interest
RNAi	RNA interference
RSPs	radial spokes proteins
RSs	radial spokes
RT	room temperature
SDS-PAGE	sulfate – polyacrylamide gel electrophoresis
TRP	trypanin related protein
TZ	transition zone
UTR	untranslated region

1 Introduction

Eukaryotic flagella or cilia (the terms are used interchangeably) are highly evolutionarily conserved microtubule-based organelles protruding from the cell surface.

The cilia are present in a number of organisms, from protists to mammals. In humans, the cilia are found on nearly all polarised types of cells. They typically appear either in arrays as motile cilia or individually as primary sensory cilia. They are multifunctional, hence their malfunctions lead to many phenotypically variable pleiotropic disorders in humans, collectively termed as ciliopathies.

The cilia consist of hundreds of structural proteins that are organised into specialised regions. At the proximal end the basal body is present, which transits via the transition zone into the axoneme, terminated by the distal tip. The axoneme is the core structure of the cilium and is composed of nine microtubular doublets usually surrounding the central pair of microtubules and associated structures.

For the presence of this organelle it is crucial to retain its constitution. This can be achieved either by high stability of protein constituents or by their turnover. Originally, it was proposed that the axonemal structure is comparatively stable *in vitro* (Tilney & Gibbins, 1968). However, subsequent cell fusion experiments of a biflagellate single cell alga *Chlamydomonas reinhardtii* showed that axoneme is a dynamic structure with both elongation and turnover happening exclusively at its distal end (Johnson & Rosenbaum, 1992; Marshall & Rosenbaum, 2001; Song & Dentler, 2001).

Due to challenging reverse genetics in *C. reinhardtii*, the turnover was demonstrated only for a limited number of axonemal proteins so far. Despite that, these findings formed the prevailing view that the axonemes of cilia in other organisms are also dynamic and undergo turnover. To further validate this hypothesis *Trypanosoma brucei* was employed as a model organism; *T. brucei*, the causative agent of human African trypanosomiasis (HAT), offers molecular biology approaches unparalleled among flagellated organisms. Foremost, the ability of effective homology recombination enables rapid and scalable tagging of proteins in their endogenous loci.

Leveraging this high experimental tractability, these findings were revisited in *T. brucei* – the eukaryote evolutionary distant to *C. reinhardtii* – for a number of proteins from a variety of axonemal complexes.

2 Aims of the thesis

The main aims of presented thesis are to determine – by studying a number of axonemal constituents – the site of axonemal growth, wheather protein turnover occurs, and if so to elucidate where does it happen.

3 Literature review

3.1 Cilia/Flagella

The discovery of the microscope in 1675 has enabled the observation of living cells allowing the description of first organelles and determination of their function. It was Antony Van Leeuwenhoek who had observed and described “little legs” of protozoan that were adapted for nimble motion, which later came to be known as cilia (Satir, 1995).

Technical progress in life sciences led to an increased recognition of these iconic organelles. Throughout history, the cilia came across many names and classifications because of their diverse organisation, structure, length, or function. Nowadays, cilia and eukaryotic flagella are considered being the same organelle. Based on their structure and function, they can be broadly divided into two categories: 1/ Motile cilia and flagella, which generate movement of cells or surrounding fluids. These have a complex structure reflecting the ability to generate highly defined motion. They can be present as a single organelle per cell, such as in the case of a mammalian sperm, or can occur in bundles on the surface of multiciliated cells, for example in the airway epithelium (Ishikawa, 2017). 2/ Non-motile cilia, which have a less complex structure, as they do not possess the machinery for motility. These are cellular antennas with sensory or signalling functions (Bloodgood, 2009). As they appear even in multiciliated cells preceding the occurrence of motile cilia they were termed the primary cilia (Sorokin, 1968), the terminology, which will be used throughout this thesis.

It should be noted that despite similarities, such as the elongated shape and generation of motion, the eukaryotic flagella/cilia are not considered being homologs of bacterial flagella and archaeal archaella. Protein composition, internal structure and the mode of movement differ markedly between these flagella. In general, ciliary beating is driven from alongside the cilia. Whereas, the prokaryotic rotating movement of the flagellum is generated from a basal motor complex on its proximal region. Hence, eukaryotic, bacterial, and archaeal flagella are different organelles with unique evolutionary history (Jékely & Arendt, 2006; Khan & Scholey, 2018).

The cilia (Fig. 3.1.) are found in many eukaryotic species, from protists to humans, suggesting a cilium was present in the Last Eukaryotic Common Ancestor (LECA). However, it has been lost in several lineages during the evolution, most notably in flowering plants and some fungi,

such as *Saccharomyces* spp. (Pazour, 2004). In mammals including humans, almost every cell type develops a single primary cilium in growth arrest conditions (Satir *et al.*, 2010).

On the other hand, in some invertebrates, such as the model organism *Drosophila*, only a few types of cells possess cilia, including spermatocytes and sensory neurons (Keil, 2012).

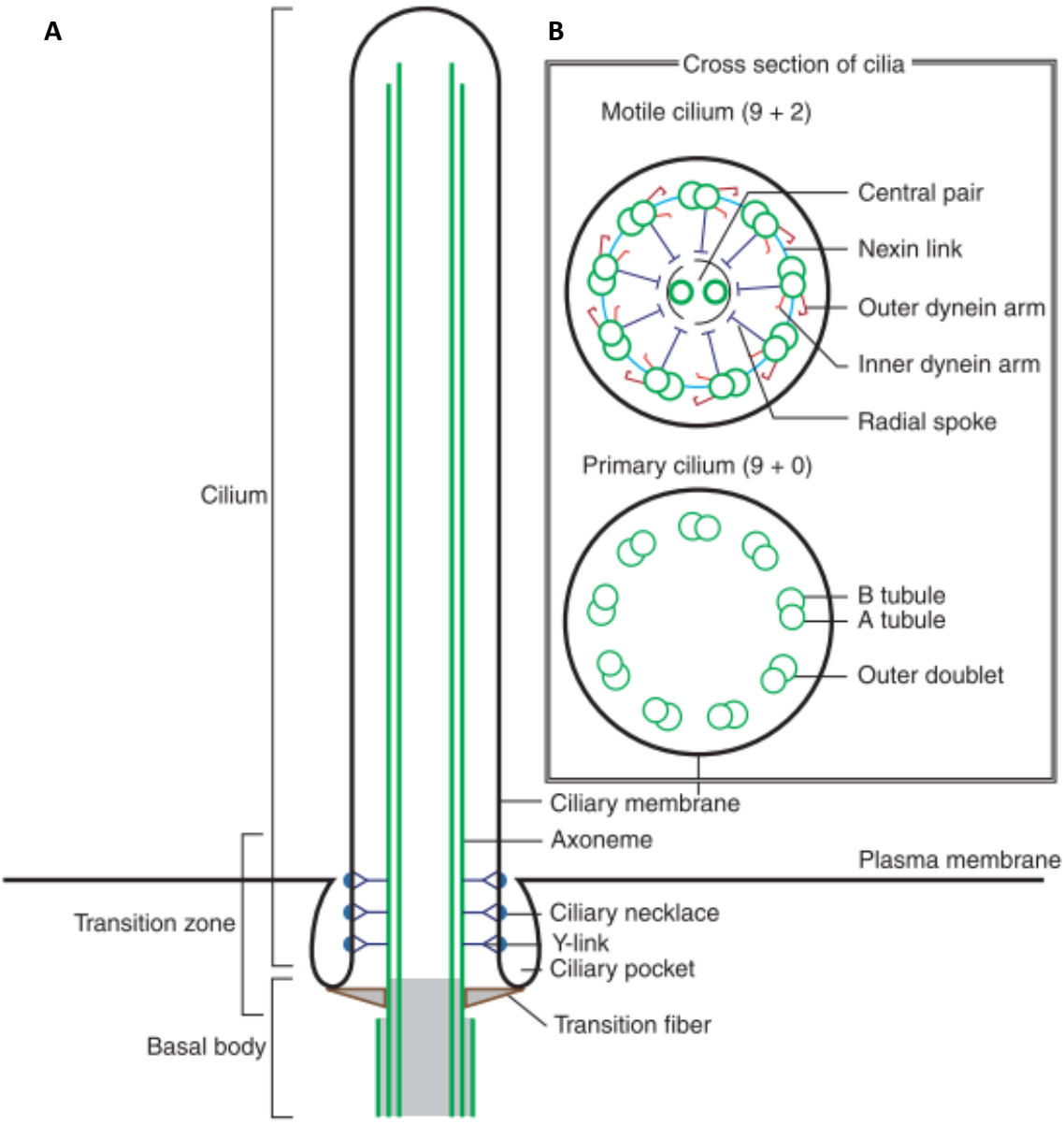

Figure 3.1. Schematic diagrams demonstrating the architecture of cilia. A) Schematic view on the longitudial section of the primary cilium showing its basic composition. **B**) Schematic view on the cross-section of a motile cilium (9+2) and a primary cilium (9+0) with their constituents. Adapted from Ishikawa & Marshall, 2017.

3.2 Basic ciliary composition and structure

Electron microscopy enabled a deeper understanding of ciliary structures. The principal structure is the microtubule (MT) -based cytoskeleton, the so-called axoneme, which is enveloped by a flagellar membrane. On cross-section, the canonical pattern of the axoneme is visible (Fig. 3.1.). In motile cilia, the arrangement consists of nine microtubular doublets (MTD) surrounding two central microtubule singlets (also known as the central pair (CP)), the so-called 9+2 arrangement firstly described in Manton, 1952. Each doublet is formed by a complete A-microtubule consisting of 13 protofilaments (PFs) and an incomplete B-microtubule containing 10 PFs (Nicastro *et al.*, 2011).

Most eukaryotes share this 9+2 MT pattern of axoneme conformation, which persists since the LECA (Carvalho-Santos *et al.*, 2011). However, there are variations among species. For example, particular insect sperm flagellum exhibits a 10+2 pattern (Dallai *et al.*, 1996).

An arrangement, where the central pair of microtubules is missing, the so-called 9+0 arrangement, has been thought to be a hallmark of non-motile cilia (Fig. 3.1B). However, there are exceptions to this simplified model. For instance, motile 9+0 cilia are present in the embryonic node (Okada *et al.*, 2005) and spermatozoa of eel (Gibbons *et al.*, 1983). On the other hand, non-motile cilia known as kinocilia with 9+2 pattern can be found in the inner ear (Flock & Duvall, 1965; Dabdoub & Kelley, 2005).

Along its length, a cilium can be divided into regions: a proximal part extended to the axoneme, capped with a distal part. Cilium is mostly enwrapped by a ciliary membrane.

3.2.1 Ciliary membrane

The axoneme is surrounded by the ciliary membrane. The ciliary membrane does not enclose the entire organelle but merges with the cytoplasmic membrane exposing the base of the cilium to the cytoplasm. However, the ciliary membrane differs in its composition from the rest of cell membranes, e.g. containing specialised signalling components (Garcia *et al.*, 2018). Near the base of some cilia is an invagination or depression of membrane known as the ciliary pocket, which is a continuous transition between the ciliary membrane and the plasma membrane. Simultaneously, it separates them (Garcia *et al.*, 2018).

3.2.2 Proximal part of the cilium

The basal body (BB) located on the very base of the cilium is a nucleation centre for a cilium during ciliogenesis (cilium formation). It consists of nine MT triplets (complete 13 protofilaments A-microtubule, and incomplete 10 protofilaments B- and C-microtubules). The BB is anchored to the membrane mainly via transition fibers. Distal to those is the transition zone (TZ). TZ comprises of Y-links fibers and ciliary necklace and creates a transition between the BB and the axoneme. In the TZ the MT triplets transit to doublets and the CP is nucleated. Another fundamental function of the TZ is that it serves as a ciliary gate selectively allowing proteins to enter and exit the cilium (Garcia-gonzalo & Reiter, 2016; reviewed by Gonçalves & Pelletier, 2017).

3.2.3 Distal part of the cilium

The distal part of the cilium has been known to represent a domain with unique protein composition and specific processes – the ciliary tip (Varga *et al.*, 2017; reviewed by Soares *et al.*, 2019). Composition of the tip seems to be diverse among organisms or tissues. Several scenarios have been observed differing in the length of the CP, A-tubules and B-tubules, as well as in presence and ultrastructure of structures capping the microtubules (reviewed by Croft *et al.*, 2018). A ciliary tip is a place where robust signalling occurs in primary cilia (Wheway *et al.*, 2018). From the distal tip, extracellular vesicles are shedded for spreading signals (Wang & Barr, 2018). Importantly, it has been proposed that the ciliary tip is the main site of axoneme building material delivery by the intraflagellar transport (IFT) machinery. In accordance, the tip appears to be the site of a new material incorporation during ciliary growth (Johnson & Rosenbaum, 1992).

3.2.4 Intraflagellar transport

Proteins synthesised in the cell body are transported to the ciliary tip by the IFT machinery, which forms IFT trains, using MTDs as railway. Anterograde IFT trains driven by a kinesin-2 motor move on B-microtubules from the base to the flagellar tip. Retrograde trains – driven by dynein motors – move along A-microtubules (Stepanek & Pigino, 2016).

3.3 Composition of axoneme

In a cross-section of a cilium, different axonemal components can be recognised (reviewed by Ishikawa, 2017). In the direction from the axonemal centre to the periphery the following are present: central apparatus (CA) surrounded by nine radial spokes (RSs), which connect it to nine microtubular doublets (MTD). Furthermore, dynein arms are attached ot MTDs: inner dynein arms (IDA) are oriented to the inner circumference of MTDs, and outer dynein arms (ODA) are located on the outer circumference of MTDs (Ishikawa, 2017). Additional components such as regulatory hubs, nexin links, and different projections are discussed later in present chapter.

A longitudial view of an axoneme shows its complexes organisation along the long axis with well-conserved axonemal repeating units (Fig. 3.2.C). IDAs and RSs pattern repeat itself every 96-nm, while ODAs are ordered in 24-nm repeats (Nicastro *et al.*, 2007; Oda *et al.*, 2014). CA structures repetitions are found in 16-nm or 32-nm periodicity (Mitchell, 2003).

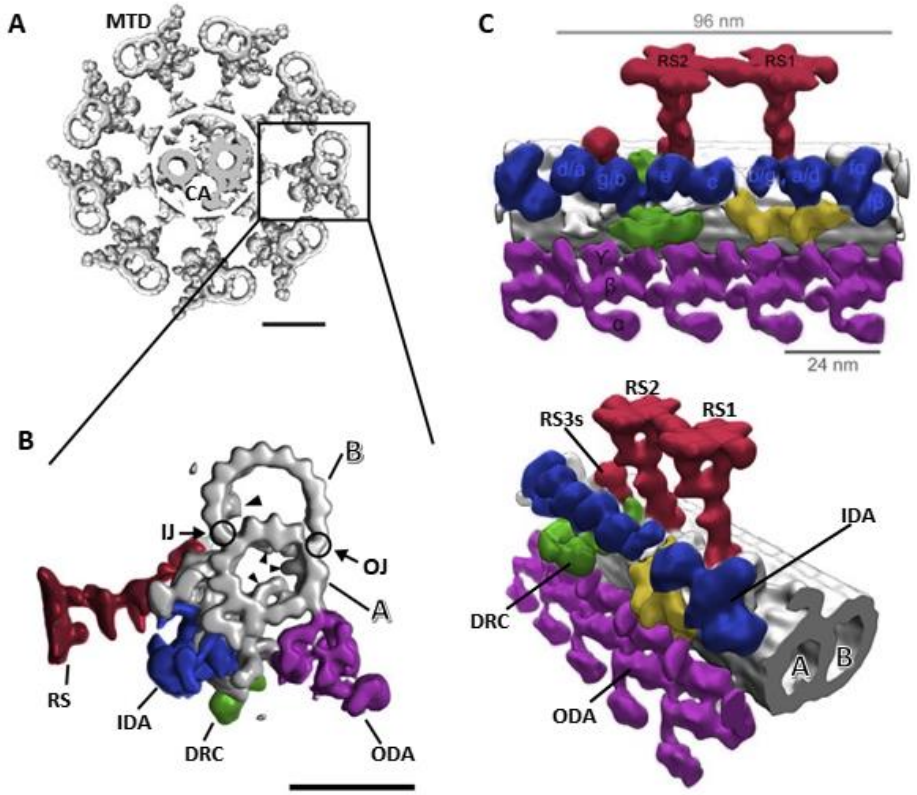

Figure 3.2. 3D reconstruction of axonemal components in *C. reinhardtii*. A) Cross-section through the axoneme showing its 9+2 structure of MTDs and CA, with their associated structures (B). MTD = microtubular doublet, CA = central apparatus. Scale bar 50 nm. **B**) Magnification of MTD with associated structures showing radial spoke (RS, red), inner dynein arm (IDA, blue), dynein regulatory complex (DRC, green), outer dynein arm (ODA, purple). Inner junction (IJ), outer junction (OJ), A-microtubule (A), B-microtubule (B), arrowheads indicating microtubular inner proteins (MIPs) are in grey. Scale bar 25 nm. **A,B**) Adapted from (Owa *et al.*, 2019) and recoloured. **C**) Longitudial view on MTD (grey) with associated structures: ODAs (purple), IDAs (blue), Intermediate and light chains of IDAs (yellow), DRC (green). Two RSs (red) are in *C. reinhardtii* fully built, whereas RS3 forms stump (RS3s). Adapted from (Pigino *et al.*, 2011) and recoloured.

3.3.1 Microtubular doublets

Microtubules are constructed from α- and β-tubulin heterodimers forming basic 8-nm repeating units from which other larger repeats of axonemal structures mentioned above are derived. In comparison with cytoplasmic microtubules, axonemal ones are significantly more stable. This stability is attributed to tubulin post-translational modifications and/or microtubule-associated proteins (Orbach & Howard, 2019). Microtubular inner proteins (MIPs) bounded to the interior site of MTDs play a significant role in MTDs assembly and stability (Ichikawa *et al.*, 2017; Owa *et al.*, 2019).

Some of these proteins are associated with a very stable portion of the MTD, that is recognised as a connection between A- and B-microtubules – the protofilament ribbon. The ribbon region consist of A11-A12-A13 protofilaments (Ichikawa *et al.*, 2017). Several proteins were described to associate with the protofilament ribbon, for example Rib72 (Ikeda *et al.*, 2003).

A- and B-microtubules are enclosed on two sites by outer and inner junctions. Inner junction structure protein FAP20 localises to all MTDs alongside the whole axoneme in *C. reinhardtii* (Yanagisawa *et al.*, 2014), as well as in *T. brucei* (Hodges *et al*., 2011), and is involved in stabilisation of the axoneme (Owa *et al.*, 2019). Interestingly, in contrast to other studied proteins it was proposed, that FAP20 is incorporated into the flagellum from the proximal end and this process is IFT independent (Yanagisawa *et al.*, 2014).

3.3.2 Radial spokes

Radial spokes are T-shaped complexes emanating from the MTDs towards the CP where they serve as mechanochemical converters. Alongside the axoneme, triplets of radial spokes (RS1, RS2, and RS3) repeat with a 96-nm periodicity. RS1 and RS2 are very similar in composition, except for a specific densities at RS2 base, where it associates with the nexin-dynein regulatory complex (N-DRC) (Pigino & Ishikawa, 2012).

3.3.2.1 Radial spokes proteins

According to data obtained from *C. reinhardtii* RS mutants, 17 radial spokes proteins (RSPs), along with six additional polypeptides, constitute RSs. These proteins are highly organized in a RS. RSP1, 4, 6, 9, 10 constitute the head of a RS (the part of the structure adjacent to the CP). RSP2, HSP40 (=RSP16), and RSP23 constitute the RS neck. Remaining proteins (RSP3, 5, 7, 8, 11 – 15, 17 – 22) were recognised as constituents of the RS stalk (Yang *et al.*, 2006; Zhu *et al.*, 2017). Of these RSP3 seems to be particularly important as it acts as a scaffold for the other proteins and binds directly to the RS neck via RSP2 protein (reviewed by Zhu *et al.*, 2017).

There are variations in compositions of RSs between species. While in *T. brucei*, one *RSP4/6* gene is present, in humans and *C. reinhardtii* two homologs (*RSP4* and *RSP6*) exist, which originated from *RSP4/6* duplication event (Curry *et al.*, 1992; Eriksson *et al.*, 2001).

3.3.2.2 Nexin-dynein regulatory complex

RSs are associated on the MTD site with the nexin-dynein regulatory complex (N-DRC), which is involved in activation of dynein motors. Within 96-nm repeat, one N-DRC complex is present and it associates with RS2 complex. A central role in assembly and function for N-DRC linker was proposed to DRC4 subunit. The main human gene for DRC4 subunit is *Gas11* (Bower *et al.*, 2013). *T. brucei* ortholog is trypanin related protein (TRP) Tb927.9.15050 (El-Sayed *et al.*, 2005). In *C. reinhardtii* it was shown that DRC4 is as a cargo of the IFT machinery, and is mainly incorporated into the axoneme at the distal end. However, occasional incorporation of DRC4 subunit alongside the axoneme was also described (Wren *et al.*, 2013). In *C. reinhardtii*, knock-downs of DRC4 as well as another N-DRC subunit – DCR2 are characterised by disruption of flagellum beating, but in diverse manners, suggesting their distinct roles within the complex (Bower *et al.*, 2018). Nexin-dynein regulatory complex 2 (DCR2) in *T. brucei* is represented by CMF70 (Tb927.11.7240) (Kabututu *et al.*, 2010).

At the base of the RS is an adaptor protein complex called the Calmodulin (CaM) and Spoke associated Complex (CSC), which contains CaM protein and CaM-binding proteins: CaM-IP2 (FAP61), -IP3 (FAP91), and -IP4 (FAP251) (Dymek & Smith, 2007). CSC stabilise RS2 and RS3 and dock them to DMT. This makes them crucial for ciliary motility (Heuser *et al.*, 2012).

3.3.3 Central apparatus

Pair of complete singlet MTs (C1 and C2) together with associated projections (Fig. 3.3.) form the central apparatus (CA). CA initiates around the TZ and extends towards the distal end of an axoneme, creating its 9+2 pattern (Lechtreck *et al.*, 2013). Two central MTs are connected one to another and stabilised through the bridge structure. This connection is mediated by PF20 protein whose deletion causes missing CP 9+0 phenotype. On the other hand, PF16 is responsible for C1 stabilisation and its deletion causes 9+1 phenotype. Mutation in Hydin (present in the C2b projection) protein leads to destabilisation of C1b and C2c projections and loss of C2b projection. However, missing Hydin cannot be detectable by revealing cilia ultrastructure by transmission electron microscopy in patients with PCD – primary ciliary

dyskinesia (Olbrich *et al.*, 2012). All of these mutations are responsible for motility impairment or loss (Carbajal-González *et al.*, 2013).

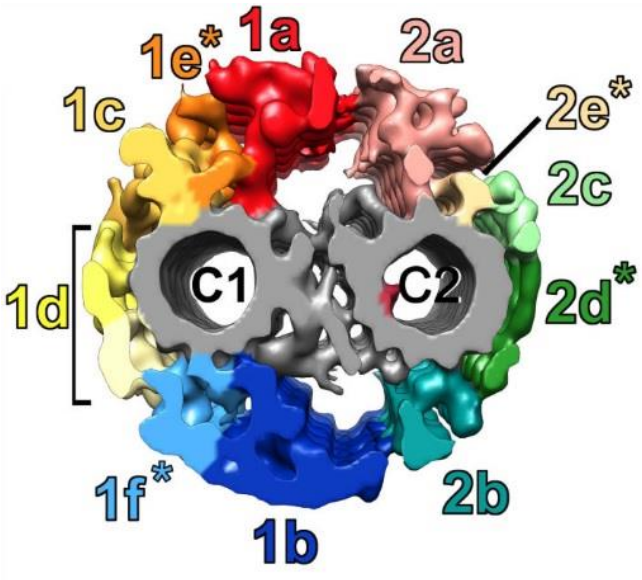

Figure 3.3. Cross-section through the central apparatus. Central apparatus consist of two singlet microtubules: C1 and C2 (grey) with their associated projections (in colours). Adapted from (Carbajal-González *et al.*, 2013).

3.3.4 Axonemal dynein arms

Axonemal dynein arms are molecular motors, which convert chemical energy of ATP hydrolysis into mechanical force generating sliding on adjacent doublets on each other which is translated into axonemal bending and flagellar beat. Occupying every MTD, they are anchored to the A-microtubules and interact with B-microtubules of an adjacent doublet. There are two types of the dynein arms, inner (IDAs) and outer (ODAs), facing inner and outer sides of the axoneme, respectively (Fig. 3.2.). IDAs function is to control beating form and magnitude, whereas ODAs are responsible for beat frequency. Within the 96-nm repeat – one main inner arm (I1/f) and six additional monomeric inner arms are periodically aligned. Four identical outer arms are placed in the 96-nm repeat. One of them is connected to IDA, and other ones are associated with MTD differently (King, 2016). However, axoneme dynein arms constituents along the axoneme may occur asymmetrically (Edwards *et al.*, 2018). Dynein arms are comprised of subsets of large heavy-chain motors, which are the actual ATPases, and accessory intermediate-chains, and light-chain. There are two genes coding for OAD heavy chains in humans – OADα and OADβ (Pazour *et al.*, 2006). An example of an IAD heavy-chain protein in humans is DNAH10 (Pazour *et al.*, 2006) is homologous to trypanosomal IAD protein (Tb927.4.870) (Wickstead & Gull, 2007).

3.4 Function and Dysfunction of cilia in humans

In mammals four types of cilia were identified based on their structure. In specialised tissues there are combinations of motile cilia and non-motile cilia present, with axonemal structure 9+2 or 9+0 (Fliegauf *et al.*, 2007).

3.4.1 Motile cilia

3.4.1.1 Multiple motile 9+2 cilia

One of the main ciliary functions is to create motion. Motile 9+2 cilia grouped to bundles on the surface of epithelial cells constitute multiciliated epithelia. Their role is to generate a synchronized beating movement, which drives fluid flow in a particular direction. The motile cilia fulfil their function in different epithelia throughout the mammalian body, and their dysfunctionalities cause several health problems and diseases.

Specifically, the role of respiratory cilia is mucus transportation resulting in mucociliary clearance of the tracheobronchial tree (Wanner *et al.*, 1996). Aberrant beat frequency or number of cilia can lead to an accumulation of mucus. Failure of the mucus clearance leads to the accumulation of pathogens, particles, and toxins, which causes respiratory tract infection and chronic respiratory problems (Wallmeier *et al.*, 2014). Although, historically, signalling functions were attributed to primary cilia. It becomes apparent that they are also present in motile cilia. The respiratory cilia are suggested to have noncanonical Hedgehog (HH) signalling function since they contain HH signalling components (Mao *et al.*, 2018). Moreover, they can share both mechanosensory and chemosensory properties (Bloodgood, 2010), as is in the case of bitter taste receptors on motile airway cilia (Shah *et al*., 2009).

Similarly, motile 9+2 cilia in the middle ear and Eustachian tubes function in mucociliary clearance of the tympanic cavity (Ohashi *et al.*, 1985). Ciliary malfunction leads due to the accumulation of excessive fluid with foreign particles to otitis media, the inflammation of the middle ear (Li *et al.*, 2014).

Ependymal cilia are present in the ventricles of the central nervous system. They contribute to the regular movement of cerebrospinal fluid forming ependymal flow and maintenance of brain homeostasis. Another function is linked to the generation of a concentration gradient of signal molecules, which results in guidance and relocation of neuroblasts – primitive nerve

cells (Sawamoto *et al.*, 2006). Loss of cilia function can lead to cerebrospinal fluid accumulation in the brain ventricles, which may result in hydrocephalus (Banizs *et al.*, 2005).

Female and male reproductive tracts (fallopian tube in females and efferent ducts in males) are also covered with cilia (Yeung *et al.*, 1991; Lyons *et al.*, 2006).

Fallopian tube cilia are important for female fertility. The proper ciliary beat frequency was considered as a dominant feature important for gamete and embryo transport through the fallopian tube (Xia *et al.*, 2018). Ectopic pregnancy and fertility problems were observed as a consequence of motile cilia defect (Lyons *et al.*, 2006; Blyth & Wellesley, 2008).

Multiciliated cells also line efferent ducts of the male reproductive system. They are considered to assist in the transportation of yet non-motile spermatozoa from the testis to the epididymis (Afzelius, 2004). Another proposed function is the creation of reflux, which releases sperm when these are in the desired concentration (Winet, 1980).

Compromised motility of cilia often leads to respiratory problems and infertility. This is due to a highly similar structure and composition of respiratory cilia, efferent ducts cilia, and sperm flagella.

3.4.1.2 Motile 9+2 monocilia

Probably the best known motile single cilium is the sperm flagellum. It generates movement of the entire sperm cell through the female reproductive tract and thereby ensures fertilisation. Sperm immotility (sperm flagella dyskinesia) is often accompanied by cilia motility problems in other tissues (Neugebauer *et al.*, 1990; Toyama *et al.*, 2009).

3.4.1.3 Motile 9+0 cilia

Motile cilia with the 9+0 structure are found in the node of mammalian embryos during early developmental stages. Through their conical beating in rotational movement, nodal cilia are generating a flow of fluid, which was termed the nodal flow. The nodal flow is critical for the correct development of body asymmetry. Embryos lacking the nodal cilia exhibit randomised left-right asymmetry (Nonaka *et al.*, 1998; Nonaka *et al.*, 2002). This can lead to partial or complete mislocalisation of internal organs.

3.4.2 Non-motile cilia

3.4.2.1 Non-motile 9+0 cilia function

Non-motile primary cilia with the arrangement of 9+0 are present on the surface of almost all polarised cells in vertebrates. Immotile single primary cilia mainly function as sensory and

signalling organelles. Important signalling pathways such as Wnt, Notch, Hippo, PDGFRα, mTOR, GPCR, and HHs have been associated with the primary cilia (Wheway *et al.*, 2018). Defects in these cilia result in a wide range of diseases, which are described below.

3.4.2.2 Non-motile 9+0 cilia

Renal cilia exhibit sensory function by sensing urine flow. Two proteins were shown to be involved in mechanosensitivity - polycystin-1 and polycystin-2, encoded by *PKD* (Polycystic kidney disease) *1* and *PKD2* genes, respectively. Mutations in these genes cause PKD (Nauli *et al.*, 2003; Gresh *et al.*, 2004). Additionally, mutant *PKD1* gene causes the cardiovascular system and skeletal defects during development (Boulter *et al.*, 2001).

Photoreceptor cells of the retina (rods and cones) contain the connecting cilium, the distal segment of which is the place where sensor proteins – opsins localise. The dysfunctionality of connecting cilium leads to retinal degenerative diseases and blindness (Gilliam *et al.*, 2012).

3.4.2.3 Non-motile 9+2 cilia

Kinocilium in the inner ear acts to polarise actin-based stereocilia, which sense vibrations. Loss of kinocilia function leads to hearing impairment (Okamoto *et al.*, 2017).

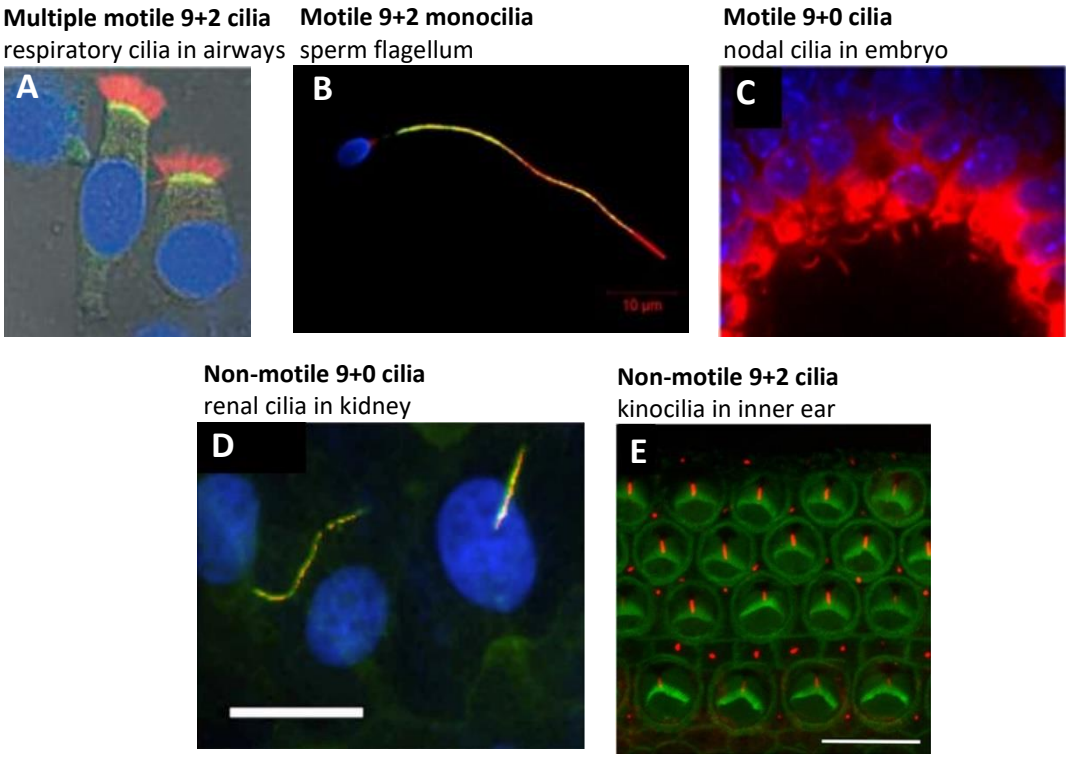

Figure 3.4. Examples of different cilia types in vertebrates
Immunofluorescence images of different types of cilia (red). **A**) **Multiple motile 9+2 cilia** = respiratory cilia in airways; antibody stained γ-tubulin (green) is marking the microtubule organizing centers. Adapted from (Fliegauf *et al.*, 2005). **B**) **Motile 9+2 monocilia** = sperm flagellum; stained with antibody gainst SPAG6 (green). Adapted from (Dong *et al.*, 2018). **C**) **Motile 9+0 cilia** = nodal cilia in embryo. Adapted from (Hadjantonakis *et al.*, 2008). **D**) **Non-motile 9+0 cilia** represent by renal cilia in kidney; with fluorescence localisation of Dopamine receptor type 5 (green). Adapted from (Upadhyay *et al.*, 2014). **E**) **Non-motile 9+2 cilia** = kinocilia in inner ear; stereocilia (actin-based) were labeled with phalloidin (green). Adapted from (Okamoto *et al.*, 2017). As ciliary marker (red) was used: DNAH5-specific antibody (**A**) and acetylated α-tubulin (**B-E**). Nuclei were stained with Hoechst (**A-C,E**) or DAPI (**D**). Scale bars represent 10 μm.

3.5 Ciliopathies

Ciliary malfunctions lead to syndromes collectively known as ciliopathies. Ciliopathies are phenotypically variable disorders affecting motile and/or non-motile cilia (Kempeneers & Chilvers, 2018).

One of the most common ciliopathies affecting ciliary motility was named Kartagener syndrome (Kartagener, 1933). Typical clinical symptoms include frequent respiratory problems as pneumonia, colds, sinusitis, bronchitis, and ear infections as a result of disturbed mucociliary clearance. The syndrome was also associated with *situs inversus* in half of the cases. To symptoms also belongs male infertility caused by sperm immotility (Afzelius, 1976). Other described symptoms include otitis media, hydrocephalus, and brain dysplasia (Panigrahy *et al.*, 2016).

A Kartagener syndrome, like immotile-cilia syndrome, belongs to a group of diseases called primary ciliary dyskinesia (PCD). PCD is an inherited recessive autosomal disorder with the prevalence ranging from 1:2,000 to 1:40,000 live births, although PCD is under-diagnosed in Europe (Kuehni *et al.*, 2010). Mutations affect ciliary structural proteins, or cytoplasmic proteins serving as functional units in pre-assembling complexes of ciliary proteins (Mitchison *et al.*, 2012). PCD manifestations range from changes to cilia beat frequency and pattern to cilia immotility or their complete absence. Diagnosis of the disease commonly involves characterisation of changes in cilia ultrastructure by TEM, where absence of structures is apparent. Usually, subunits, which participate in the ciliary movement are affected. For instance, outer and inner dynein arms, nexin links, radial spokes, central pair of MTs, and the basal body (Kempeneers & Chilvers, 2018) (for detail explanation see Chapter).

On the other hand, non-motile primary cilia are not affected by genetic disruptions of components of motile cilia mentioned above. The majority of non-motile ciliopathies represent sensory ciliopathies, when signal transduction function in sensory cilia is disrupted. Primary ciliopathy symptoms may include kidney, liver, pancreas, and bone defects, and defects in development of heart or central nervous system. Furthermore, obesity, diabetes mellitus, cystic disorders, polydactyly, and dwarfism can occur. These symptoms can occur in combination in different diseases and syndromes such as Alström syndrome, Bardet-Biedl

syndrome, Joubert syndrome, Meckel-Gruber syndrome, polycystic kidney disease, retinitis pigmentosa, Senior-Løken syndrome, Usher syndrome and others (Wheway *et al.*, 2018).

3.6 Assembly and Turnover of the ciliary cytoskeleton

As there are no ribosomes in the cilia, all protein constituents (probably up to one thousand protein species) have to be imported from the cell body (Lechtreck *et al.*, 2017). How do they move within the flagellum to reach the site of their ultimate localization? Given that a cilium is a slender (hundreds of nm) and long (tens of μm) organelle, diffusion is not expected to be an efficient mean of transport. Indeed, it was demonstrated that there exists a machinery dedicated for transport of material into the cilium, along it, and out of the cilium (Kozminski *et al.*, 1995). Moreover, it has been demonstrated by pioneering experiments with fusing (mating) *C. reinhardtii* cells, that tagged axonemal proteins expressed in one of the fusing cells appear exclusively at the distal end of growing flagella of the second fusing cell (Marshall & Rosenbaum, 2001; Lechtreck *et al.*, 2013). These experiments established the distal end exclusive for addition of material into the axoneme. This model was since then universally accepted and extrapolated to other eukaryotic flagella. However, in fact, the distal end exclusive addition was so far experimentally demonstrated only for a limited number of axonemal proteins in *C. reinhardtii* (Marshall & Rosenbaum, 2001; Song & Dentler, 2001) and for axonemal and non-axonemal cytoskeletal proteins in *T. brucei* (Subota *et al.*, 2014; Vincensini *et al.*, 2018). Moreover, these experiments had certain limitations, such as the potential overexpression of the proteins due to using non-native regulatory elements or leakiness of inducible systems (Marshall & Rosenbaum, 2001; Vincensini *et al.*, 2018).

Motile cilia cover the airway surface forming ciliated epithelial cells (see Chapter 3.4.1.1), which are considered terminally differentiated cells (Rawlins & Hogan, 2008). These cells are long lived, and their renewal rate is remarkably slow in comparison to other tissues; their steady-state replication index is app. 1% per 24 hours (Stripp & Reynolds, 2008). Motile cilia on the surface of these cells perform mucociliary clearance by mechanical work – beating. The mechanical stress related to the beating is likely to cause over time damage to their proteins, which may be exacerbated by pathogens, pollutants etc. these cilia are exposed to (Wanner *et al.*, 1996). Similarly, cells of some flagellated protists such as *T. brucei* are likely to live for days constantly using their flagellum for cell motility (Langousis & Hill, 2014). Hence, mechanisms enabling protein turnover are likely to operate in these organelles facilitating their maintenance.

In some cilia, such as in *C. reinhardtii*, an IFT – dependent tubulin turnover occurring exclusively at the distal end of steady-state axonemes was demonstrated by fusion experiments (Marshall & Rosenbaum, 2001). In *T. brucei*, on the other hand, it was demonstrated by a fluorescence recovery after photobleaching (FRAP) experiment that there is no significant turnover of an axonemal dynein intermediate chain up to two hours post photobleaching (Vincensini *et al.*, 2018). To be able to reconcile these findings, experiments on a longer time scale and with a larger number of axonemal proteins are needed.

3.7 Model organism *Trypanosoma brucei brucei*

T. brucei is a flagellated diploid protozoan parasite belonging to Kinetoplastidae order. The main characteristic of the kinetoplastida group is the possession of kinetoplast, a specifially structured mitochondrial DNA, called kinetoplast DNA (kDNA) throughout this thesis. There are three subspecies of *T. brucei*. While *T. b. brucei* causes Nagana disease of cattle and is not infective for humans, *T. b. gambiense* and *T. b. rhodiense* are pathogens of humans causing African sleeping sickness, also known as Human African trypanosomiasis. This parasite undergoes a complex life cycle with complex morphological changes. During *T. brucei* transmission, mammalian hosts are infected by the parasite through an insect vector – tsetse fly, *Glossina* spp. In the vector, *T. brucei* first assumes procyclic form in the midgut. Afterwards, the parasites migrate through tissues of the fly, which is accompanied by a defined series of morphological changes, ultimately colonizing salivary glands, where they turn into metacyclics, ready to infect the mammalian host. After transmission into a mammalian host, trypanosomes are found in the blood and adipose tissue as a bloodstream form (Matthews, 2005; Trindade *et al.*, 2016).

3.7.1 Procyclic form

Currently, bloodstream and procyclic forms can be cultured in in vitro laboratory conditions. In this work, procyclic form cells were used (Chapter 0.0), because they are more amenable to genetic manipulations and other experimental approaches (Berriman *et al.*, 2005).

3.7.1.1 Advantages of T. brucei *as a model*

The major advantages of using *T. brucei* as a model are following. *T. brucei brucei* procyclic cells are easy to culture in liquid medium. The genome of *T. brucei* brucei has been sequenced and assembled. Almost no introns are presented in *T. brucei* genes (for more information, see review Vesteg *et al.*, 2019). A potent RNAi machinery operates in this organism, allowing for inducible depletion of a gene of interested in modified cell lines (Barnes *et al.*, 2012). Moreover, an effective DNA recombination pathway enables tagging of genes in their endogenous loci, thereby not interfering with regulation of their native expression (Gibson *et al.*, 2015).

Importantly, *T. brucei* is characterised by a well-defined cell morphology tightly linked to cell cycle progression. It also enables studying a mature and a nascent flagellum in a single cell (Vaughan & Gull, 2008).

3.7.2 Cell cycle of *T. brucei*

The procyclic trypanosome form is representing a trypomastigote type of a cell, which is undergoing defined changes during its cell cycle, retaining flagellum for a whole time. Main criteria, for determining different stages, are position and morphology of cell structures and order of their division, namely: nuclear DNA (nDNA), kDNA, flagella, and corresponding basal bodies. Basal body structure connected to kinetoplast represents a starting place of flagellum growth (Hayes *et al.*, 2014). Schematically, composition of *T. brucei* cell and its relevant features is shown in Fig. 3.5.

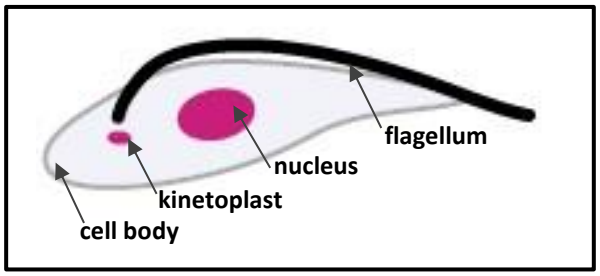

Figure 3.5. Schematic model of a *T.brucei* cell
Schematic representation of a *T.brucei* cell showing its crucial parts: cell body (light grey), flagellum (black), kinetoplast and nucleus (magenta).

In procyclic trypanosomes, the new flagellum presence and its length, kinetoplasts and nucleus division are tightly linked to the cell cycle status of an individual cell. The new BB and the nascent daughter flagellum are positioned posterior to the mother flagellum (Fig. 3.6.).

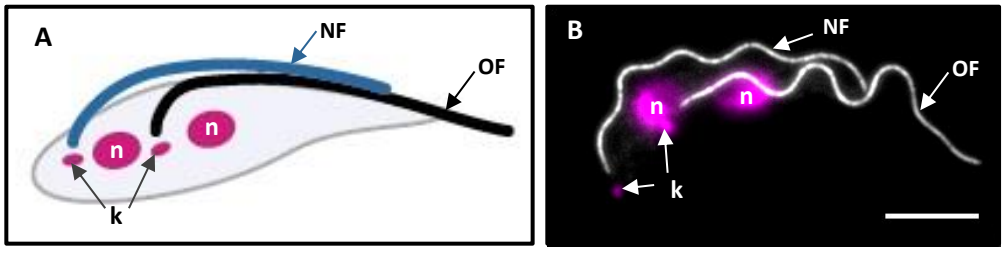

Figure 3.6. Dividing 2F2K2N *T. brucei* cell showing flagella positioning
A) Schematic representation of a *T. brucei* cell in 2F2K2N stage of cell cycle. NF = new flagellum (blue), OF = old flagellum (black), k = kinetoplast (magenta), n = nucleus (magenta). **B**) Fluorescence image showing 2F2K2N *T. brucei* cell. Daughter/new flagellum (NF) and mother/old flagellum (OF) are in white. DAPI (magenta) is visualising DNA: n = nucleus, and k = kinetoplast. Scale bar represents 5 μm.

At the beginning of the cell cycle (Fig 3.7.), a *T. brucei* cell is characterised by the presence of one flagellum, one kinetoplast, and one nucleus (1F1K1N) in interphase (Fig. 3.5.). After duplication of the BB, at the beginning of S phase, the production of a new flagellum is initiated. As the new – flagellum elongates the kDNA divides, forming a 2F2K1N cell. Towards the end of the cell division, mitosis (2F2K2Nm) occurs producing a 2F2K2N cell (McKean, 2003; Benz *et al.*, 2017). Cell division culminates by the cleavage furrow starting from anterior-most point of the new flagellum attachment to the cell body and proceeds towards the posterior cell end (2F2K2Nc), giving rise to two similar but not identical cells (Abeywickrema *et al.*, 2019).

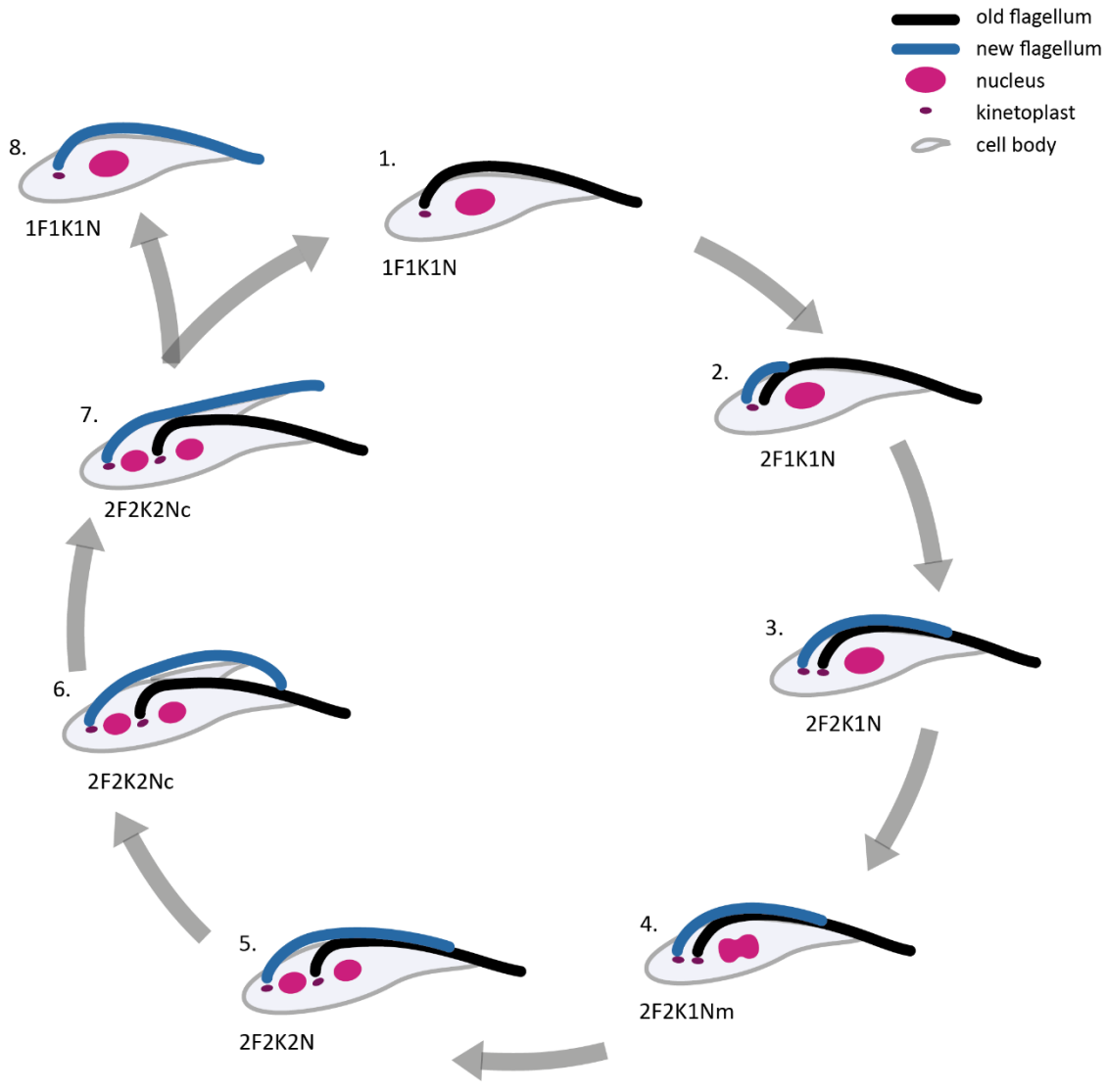

Figure 3.7. Schematic model of the *T. brucei* cell cycle
Schematic representation of a crocyclic cell undergoing cell cycle showing its different stages. Cell body (light grey), old flagellum (black), new flagellum (blue), kinetoplast (purple), and nucleus (magenta).

3.7.3 Flagellum of *T. brucei*

T. brucei flagellum possesses structures common to other eukaryotic flagella, as described in the section 3.3. Its flagellum, however, has some specific features described below.

3.7.3.1 Flagellar pocket

The flagellar pocket of *T. brucei* is an extreme example of the ciliary pocket found also in other ciliated organisms. In *T. brucei* this pocket forms a deep membrane invagination around the very proximal part of the flagellum. The endo/exocytosis take place exclusively in the flagellar pocket in trypanosomes (Absalon *et al.*, 2008).

3.7.3.2 Flagellum attachment zone

The region, via which a flagellum is laterally attached to the cell body, is called the flagellum attachment zone (FAZ). This cytoskeletal structure extends from the flagellar pocket and continues along almost an entire flagellum length, towards the anterior end of the cell. FAZ is critical for determining and maintaining morphology of a *T. brucei* cell (Sunter *et al.*, 2015). FAZ is formed by a filament under the cytoplasmic membrane; cell body to flagellar membrane junctions morphologically comparable to a cell-to-cell adhesion structure – *macula adherens*; and FAZ fibres linking the junctions to the seventh axonemal MTD in the flagellum (Hayes *et al.*, 2014).

3.7.3.3 Paraflagellar rod

The paraflagellar rod (PFR) is emerging from the flagellar pocket, and runs parallel to the axoneme underneath the ciliary membrane. This lattice-like protein structure consists of approximately twenty proteins (Lacomble *et al.*, 2009), of which PFR1 (73 kDa) and PFR2 (69 kDa) are the most predominant. PFR is connected to the fifth and sixth axonemal MTDs. The main PFR function is proposed to be related to the flagellar motility and thereby cell motion. Therefore, PFR is essential for parasite life and pathogenicity (Deflorin *et al.*, 1994; Koyfman *et al.*, 2011).

3.7.3.4 Peri-axonemal structure containing CFAP43

CFAP43 and CFAP44 proteins are located between PFR and MTDs. These two proteins are essential for maintaining a precise flagella organisation. Interestingly, although the PFR to MTDs connection is trypanosome-specific, orthologs of these proteins are present also in mammalian sperm, and mutations in them result in multiple morphological abnormalities of the sperm flagella along with infertility in humans (Coutton *et al.*, 2018).

3.7.3.5 The flagella connector

One specification of *T. brucei* is the presence of the flagella connector (FC) structure, which connects the tip of the new flagellum to the side of the old flagellum. As the new flagellum elongates, the FC moves along the old flagellum, thereby helping it to inherit a similar helical pattern on the cell body surface (Moreira-Leite, 2001). The FC has an asymmetric structure and composition, with specific proteins constituting its new flagellum, old flagellum and membrane junction zones. On the other hand, at the tip of both flagella axonemal capping structure 1 (ACS1) protein is present (Varga *et al.*, 2017).

4 Material and Methods

All used reagents are listed in Supplementary Table 9.8.

4.1 DNA manipulation techniques

4.1.1 Polymerase chain reaction

Polymerase chain reaction (PCR) was applied for generation of inserts used for vector construction. Furthermore, "long primer PCR" was used for "long primer PCR tagging". To increase specificity and yield of a PCR products "touchdown PCR" was used. Determination of annealing temperature for different primer pairs was achieved by "gradient PCR". This PCR also allowed the use of one PCR program with different reactions containing primer pairs for different annealing temperatures. "Colony PCR" was used for identification of bacterial colonies with vectors containing correct inserts, which were further validated by sequencing. "Tagging-validation PCR" allowed detection of the correctly tagged gene in cell lines.

DNA amplification was performed using the BioRAD C100 Touch™ Thermal Cycler. All the PCR approaches are disclosed below. DNA primers used in every PCR application are listed in the Supplementary Tables 9.2. – 9.7.

4.1.2 Horizontal gel electrophoresis

Horizontal gel electrophoresis (ELFO) was used for size determination of DNA molecules, verification of DNA product presence after PCR, and separation of desired DNA molecules from others.

Due to the natural negative charge of DNA, DNA molecules move from the negatively charged cathode towards the positively charged anode, in an electrophoresis cell. The ionic buffer Triss-Acetate-EDTA (TAE) (1X) was used for creating an electric field. TAE (1X) was prepared from 50X TAE (2 M Trizma base, 5.71% acetic acid, 50 mM EDTA). Agarose gel 1% (w/v) served as a matrix for molecule migration. Agarose was dissolved in TAE (1X) by boiling in a microwave. After the temperature of the gel decreased to app 50°C, "RedSafe™ Nucleic Acid Staining Solution" (iNtRON) (1 µL per 20 mL of gel) was added. Still warm gel was cast to the gel-casting tray and loading wells were created by a comb. Next, the cooled gel was placed to electrophoresis cell, and samples were loaded into wells. As a loading buffer 6X Gel Loading Dye, Purple (NEB) was usually used. To estimate DNA molecule sizes molecular-weight markers- 100 b and/or 1 kb DNA Ladder (NEB) were used. Electrophoresis was performed at 5 V per 1 cm of distance between anode and cathode. Visualisation of DNA was carried out by an ultraviolet transilluminator.

4.1.3 DNA extraction from agarose gel and purification of PCR products

For DNA extraction from agarose gels or purification of PCR products the FavorPrep™ GEL/PCR Purification Kit (Favorgen®) or the QIAquick Gel Extraction Kit" (Qiagen) were used. In both cases, the manufacturer manual was followed. The DNA elution step was performed with the use of ddH_2O.

4.1.4 DNA concentration measurement

The concentration of DNA (ng/µL) was measured by spectrophotometer "NanoDrop® ND-1000" (Thermo Fisher Scientific) with NanoDrop 1000 v3.8.1 software. For calibration ddH_2O was used.

4.1.5 DNA sequencing

Verification of the correct DNA sequence was done by sequencing, which was carried out by a sequencing facility. Samples for sequencing were prepared in 10 µL volumes: 5 mM primer and 400 – 500 ng of DNA template. All sequencing primers are listed in the Supplementary Table 9.6.

4.1.6 Restriction digest

The restriction digest was carried out in 50 µL volumes using 10X NEBuffers (NEB) and 10 units of two restriction enzymes, which are listed in the Table 4.1. A typical amount of DNA was 1 µg. The reaction was usually carried out for 1 hour at 37°C in a dry block heater. The reaction was stopped by inactivation by heating.

Table 4.1. List of used restriction enzymes; pDNA = plasmid DNA

Enzyme	Manufacturer	Catalogue #	Buffer	Concentration	Usage
BamHI	NEB	R0136S	Neb 3.1	20 U/µL	pDNA construction
BstXI	NEB	R0113S	Neb 3.1	10 U/µL	pDNA linearization
HindIII	NEB	R0104S	Neb 2.1	20 U/µL	pDNA construction
NotI	NEB	R0189S	Neb 3.1	10 U/µL	pDNA linearization
NotI-HF	NEB	R3189S	Cut smart	20 U/µL	pDNA construction
KpnI-HF	NEB	R3142S	Cut smart	20 U/µL	pDNA construction
XbaI	NEB	R0145S	Cut smart	20 U/µL	pDNA construction

4.1.7 DNA ligation

Linearized DNA molecules treated by restriction enzymes and purified were ligated together according to ligation protocol (20 µL reaction): 10X T4 DNA Ligase Buffer (NEB), vector DNA, insert DNA, nuclease-free water and T4 DNA Ligase (NEB). Vector:insert ratio was 1:3. An amount of used DNA was calculated as follows: volume of insert DNA [µL] = {[(50 x size of the insert in kb)/size of the vector in kb]x3}/conc. of the insert in ng x μL^{-1}; the volume of vector DNA [µL] = 50/conc. of the vector in kb. The ligation step was performed at room temperature (RT) for 2 hours (hrs).

4.1.7.1 3-way ligation

Vector:insert1:insert2 ratio was experimentally established to 1:2:2. Volumes of DNA vector and inserts were calculated based on the same formula as in the case of ligation with only one DNA insert. The 3-way ligation was performed at RT for 2 hrs or at 16°C for 4 hours.

4.1.8 Oligonucleotide phosphorylation

Synthesized and dehydrated oligonucleotides (oligos) were dissolved in water to 100 μM concentration. A phosphorylation reaction was mixed according to Table 4.2 and incubated for 1 hour at 37°C, followed by deactivated at 75°C for 10 min.

Table 4.2. Oligonucleotide phosphorylation reaction (20 μL)

Reagent	Final concentration	Amount [μL]
Oligo (100 μM)	10 μM	2
T4 PKN buffer A (10 X)	1X	2
T4 polynucleotide kinase	10 U	1
ddH_2O		15

4.1.9 Oligonucleotide annealing

Oligonucleotides were mixed according to Table 4.3.A and the annealing performed according to Table 4.3.B.

Table 4.3.A Oligonucleotides annealing reaction (50 μL)

Reagent	Final concentration	Amount [μL]
FW oligo (10 μM)	5 μM	2.5
RV oligo (10 μM)	5 μM	2.5
ddH_2O		45

Table 4.3.B Temperature program for oligos annealing

Step	Temperature	Duration	Repetition
Denaturation	95°C	5'	
Annealing	-1°C	1'	70 cycles
Infinitive hold	4°C	∞	

4.2 Bacterial techniques

4.2.1 Bacterial strain

Molecular cloning methods were performed using *E. coli* DH5α strain (F⁻ *endA1 glnV44 thi-1 recA1 relA1 gyrA96 deoR nupG purB20* φ80d*lacZ*ΔM15 Δ(*lacZYA-argF*)U169, hsdR17($r_K^- m_K^+$), λ⁻) cultured in 20 g/L lysogeny broth (LB) – Miller Broth medium (10 g/L NaCl). The medium was provided by the media facility at Institute of Molecular Genetics.

4.2.2 Transformation of *E. coli*

For transformation of plasmid DNA into *E. coli* an adjusted protocol of the heat shock method was adapted (Froger & Hall, 2007). In the first step, the 50 µL of competent DH5α *E.coli* cells were thawed on ice for 10 – 20 min. Then, ligation mixture (maximum 10% of the final volume) was added, and cells were kept for 30 min on ice. Next, the heat shock at 42°C for 45 – 50 sec was performed. Cells were placed on ice for 2 min. Then 200 – 250 µL of LB medium was added. The cell culture was incubated for 30 min to 1 hour at 37°C in shaking incubator (185 rpm). The culture was then spread on plates with LB agar and ampicillin and incubated overnight at 37°C. After the incubation, separate colonies were picked from a plate and transferred into 20 µL of a liquid LB medium with ampicillin.

4.2.3 Colony screening by PCR

For identification of positive colonies by PCR, the colony PCR reaction was set up according to Table 4.4.A was PCR performed acc. to the Table 4.4.B. Results were evaluated by ELFO on agarose gel.

Table 4.4.A Colony PCR reaction (10 µL)

Reagent	Final concentration	Amount [µL]
10X standard Taq reaction Buffer	1X	1
dNTPs (10 mM)	0.2 mM	0.2
Colony prep.		1
Primer FW (10 µM)	0.2 mM	0.2
Primer RV (10 µM)	0.2 mM	0.2
Taq DNA polymerase		0.05
ddH_2O		7.35

Table 4.4.B PCR program for colony PCR

Step	Temperature	Duration	Repetition
Initial denaturation	95°C	2'	
Denaturation	95°C	30''	30 cycles
Annealing	55-62°C*	40''	
Elongation	68°C	1' per kb	
Final extension	68°C	5'	
Infinitive hold	4°C	∞	

(*Annealing temperature depended on individual primer pair)

4.2.4 Miniprep isolation

After the identification of a positive bacterial colony cells were seeded into 5 mL of LB liquid medium with ampicillin using 50 mL falcon tube with a not tightly screwed lid. The culture was incubated overnight at 37°C in a shaking incubator at 230 rpm. Thereafter, 50 uL portion of cell suspension was taken for a glycerol stock preparation (Chapter 4.2.5). The remaining cell suspension was treated according to the QIAprep Spin Miniprep Kit (QIAGEN) manufacturers manual or using the FavorPrep™ Plasmid Extraction Mini Kit (Favorgen). The DNA elution step was performed with the use of ddH_2O. pDNA was stored at -20°C.

4.2.5 Bacterial stock preservation

A 50 µL sample of an overnight liquid culture of *E. coli* was mixed with glycerol (40%, 50 µL) to a final concentration of 20%. Bacterial glycerol stocks were stored in cryogenic tubes (#D1015, KRD) at -80°C in a deep freezer.

4.3 Primers design

Primers for sequencing were designed manually by searching plasmid sequences using ApE – plasmid Editor. Additionally, other online tools were used: Tm calculator (NEB), Reverse Complement convertor (bioinformatics.org), and Kinetoplastid Genomic Resource (tritrypdb.org). Primers were chosen for optimized sequences based on these criteria: a %CG pairs content, matching annealing temperatures (within 5°C), and a length in nucleotides.

4.4 Plasmid vectors design and construction for gene tagging approaches

Design and adaptation of pEnT5 (Supplementary Fig. 9.2.) and pPOT (Supplementary Fig. 9.1.) plasmids intended for trypanosome genes tagging – general plasmid vectors maps were generated by pDNA design online tool (benchling.com) and are provided in Supplementary.

4.4.1 Modification of series of pPOT tagging vectors

Two versions of pPOT vectors were obtained from Dr. Samuel Dean, University of Oxford (Dean *et al.*, 2015). Both pPOTv4 and pPOTv7 contained the gene for blasticidin resistance for selection of transgenic trypanosomes, mNeonGreen (mNG) gene, and HaloTag gene. DNA sequences for tags and blasticidin resistance were adjusted to reflect the trypanosome amino acid code usage. In addition, plasmids were designed for N- or C- terminal tagging.

4.4.1.1 Construction of pPOTv7 vector with TC tag

The TC tag is a six amino acid tag. For its construction two phosphorylated oligonucleotides were annealed, namely MP056 and MP057 (Chapter 4.1.9). Subsequently, created dsDNA was inserted into the pPOTv7 backbone via KpnI and BamHI restriction sites. The TC-tag insert is depicted in the Figure 4.1.

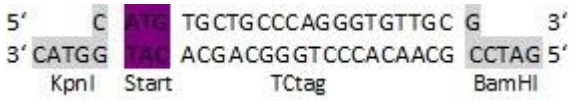

Figure 4.1. TC-tag insert containing KpnI site, polymerisation start, TCtag sequence, and BamHI restriction site.

4.4.2 Modification of series of pEnT5 tagging vectors

One of the two approaches used for generation of transgenic trypanosome cell lines was tagging by series of pEnT5 vectors. These had to be prepared by the classical method of molecular cloning.

As in the previous case, *T. brucei* genes of interest were tagged by both mNeonGreen and HaloTag. As a source of the DNA encoding for the tags the plasmid pPOTv4 was used. It was needed to get this DNA region from pPOTv4 and transfer it as an insert into a pEnT5 plasmid. Using primers Varga527 and Varga533 (Supplementary Table 9.7.) the potential insert was made by touchdown PCR (see Table 4.5.A and 4.5.B). Resultant PCR product (Fig. 4.2) was loaded on a gel (Fig. 4.3) to check the proper PCR amplification.

Table 4.5.A Touchdown PCR reaction (50 µL)

Reagent	Final concentration	Amount [µL]
10X HiFi Reaction buffer (ROCHE)	1X	5
10 mM dNTPs	0.2 mM	1
100% DMSO	2%	1
pDNA (25 ng/µL)	25 ng	1
Primer FW (100 µM)	2 µM	1
Primer RV (100 µM)	2 µM	1
ddH_2O		40
HiFi Expand Polymerase (ROCHE)		1

Table 4.5.B PCR temperature program for touchdown PCR

Step	Temperature	Duration	Repetition
Initial denaturation	94°C	5'	
Denaturation	94°C	15''	30 cycles
Annealing	62°C → 56°C	30''	
Elongation	72°C	2'	
Final extension	72°C	2'	
Infinitive hold	4°C	∞	

(Black arrow indicates a gradually decrease temperature.)

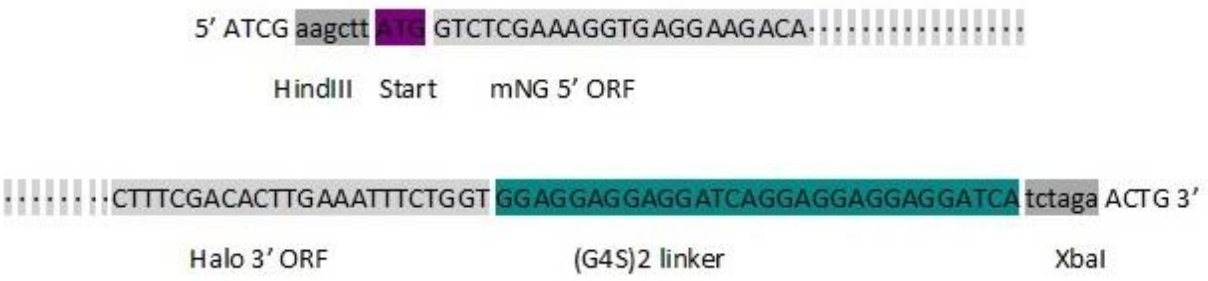

Figure 4.2. Sites of insertion of the PCR product into pEnT5 backbone- the 5' site shown on the top and the 3' site on the bottom.

Figure 4.3. Result of inserts preparation. An image of a gel after ELFO. Expected size of mNG-Halo insert = 1,655 nt, and Halo insert = 941 nt.

4.4.2.1 Plasmid backbone preparation

Backbones were made from existing pEnT5 plasmid constructs. Tags exchange was made by excision of a redundant sequence, which was removed by cutting with HindIII, XbaI enzymes. Subsequently, it was replaced by the mNG-HaloTag insert. In the case of tagging with only HaloTag, a pEnT5 plasmid with Halo insert was made in a similar way as described before (Chapter 4.4). For this primers Varga527 and Varga534 were used.

pEnT5 constructs for tagging the following three proteins of interest had already been present in the laboratory α tubulin (Tb927.1.2360) – kinesin FCP4/TbKin15 (Tb927.10.890) – and ACS1 (Tb927.7.6180). In these cases, only the fluorescent protein tag needed to be exchanged for the mNeonGreen-Halo tag. However, in the case of kinesin FCP4/TbKin15 a HindIII restriction site in the integration targeting sequence was identified (in addition to the HindIII site flanking the sequence of the tag). Hence, the pEnT5-mNG-HaloTag plasmid backbone was cleaved with XbaI (instead of HindIII) and BamHI, leading to excision of TY epitope tag sequence in addition to vector linearization.

4.4.2.2 Plasmid vector construction

In the case of construct for tagging proteins which had not been available in the laboratory previously a 3-way ligation needed to be carried out, in order to ligate together integration targeting sequences (a 3' part of 5'UTR and an 5' part of an ORF sequence), and plasmid backbone (pEnT5-mNG-HaloTag cleaved with HindIII and XbaI) (Chapter 4.1.6). The targeting sequences were prepared by PCR on the genomic DNA isolated from SmOxP927 strain cells. PCR primers used for amplification are specified in Supplementary Table 9.3. An annealing temperature for every primer pair was determined by gradient PCR (Tables 4.6.A and 4.6.B).

Table 4.6. Gradient PCR reaction (10 μL)

Reagent	Final concentration	Amount [μL]
10X HiFi Reaction buffer (ROCHE)	1X	2
10 mM dNTPs	0.2 mM	0.2
gDNA	50 ng	0.1
Primer FW (10 μM)	5 μM	0.5
Primer RV (10 μM)	5 μM	0.5
ddH_2O		6.6
HiFi Expand Polymerase (ROCHE)		0.1

Table 4.6. PCR program for gradient PCR

Step	Temperature	Duration	Repetition
Initial denaturation	98°C	5'	
Denaturation	98°C	15''	30 cycles
Annealing	gradient Tm	30''	
Elongation	72°C	30'' per kb	
Final extension	72°C	3'	
Infinitive hold	4°C	∞	

gradient Tm = for each PCR reaction was used different temperature in accordance with temperature gradient

4.5 Inducible RNA interference

Inducible knockdown cell lines were prepared by insertion of linearized pQuadra vector, including a gene-specific fragment of approximately 500 nucleotides, into the *T. brucei* genome (see Chapter "Vector linearization"). pQuadra represents an Tet-inducible dsRNA Expression System (Inoue *et al.*, 2005) allowing for an inducible expression of double-stranded RNA. Cleavage of this dsRNA leads to the formation of short fragments complementary to mRNA – the product of the gene to be silenced. Primers for amplification of gene-specific fragments (Supplementary Table 9.5.) were designed using the web-based tool "RNA-it" (Redmond *et al.*, 2003). RNAi was induced by the addition of doxycycline (0.5 µL/mL final) to the culture medium. Selection of transformants was performed via the phleomycin resistance (see Table 4.10).

4.5.1.1 RNAi knock down cell lines

Two RNAi knock down cell lines were produced- 1. A cell line with RSP4/6 protein tagged by mNG and HaloTag capable of an inducible expression of siRNAs targeting RSP4/6 mRNA. 2. cell line with RSP3 protein tagged by mNG and HaloTag capable of RNAi against RSP3 mRNA.

4.6 Other plasmid vectors used

4.6.1 pGEM®-T Easy Vector System for the cloning of PCR products

This system was used when the yield of PCR product was not sufficient for cloning via restriction sites. In that case, an amplification of the PCR product using the pGEM®-T Easy Vector System based on blue/white selection on indicator plates was used.

Ligation solution (10 µL reaction) was prepared with 5X T4 ligation buffer using 25 ng of pGEM®-T Easy Vector and the maximum possible amount of PCR product/insert. The reaction was filled with nuclease-free water to a final volume of 10 µL and set for 1 hour at RT. After transformation, bacterial culture was spread on LB/ampicillin agar plates treated by IPTG and X-Gal. A successful insertion of PCR fragment into vector led to β-galactosidase coding sequence disruption and therefore white – recombinant colonies appeared.

4.7 Gene tagging approaches

4.7.1 Long primer PCR tagging

In order to avoid the protracted process of classical molecular cloning for plasmid preparation the long primer PCR tagging method Dean *et al.* (2015) was used at later stages of the project.

This approach is enabled by the very efficient homologous recombination pathway in *T. brucei*, which requires only 50 nucleotide-long targeting sequences. For each protein to be tagged a pair of 100 nucleotide long primers were designed. These contain 80 nucleotide sequence for targeting the

integration into the *T. brucei* genome; for N-terminal tagging those correspond to the 3' part of 5' UTR and 5' part of ORF, respectively). In addition, a 20 nucleotide sequence for annealing on a respective site in the so-called PCR only tagging (pPOT) plasmids (Dean *et al.*, 2015) is included. A product resulting from a PCR with the primers of a pPOT vector contains a sequence coding for a tag and for antibiotics resistance in addition to the integration targeting sequences. A variety of pPOT plasmids is available, with different combinations of tags and resistance markers, making the system rather flexible. Figure 4.4 illustrates how does the Long primer PCR tagging approach work.

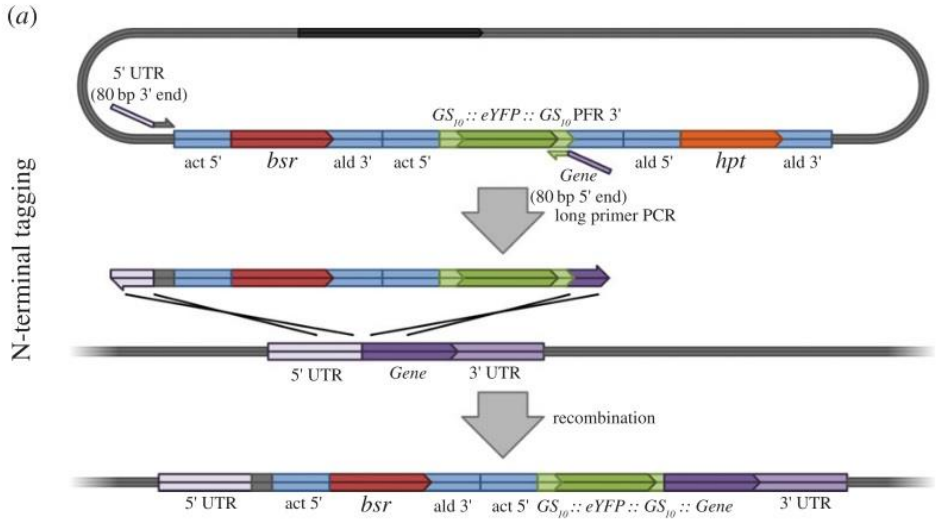

Figure 4.4. Long primer PCR tagging – N-terminal tagging. Using a pair of primers containing 5'UTR and 5' of ORF sequence in a PCR reaction with pPOTv4 plasmid generates an insert flanked by homologous sequences, which integrate into a specific position of the genome by homologous recombination. Adapted from Dean *et al.*, 2015.

4.7.1.1 Long primer PCR

Using different versions of pPOTs and specific primers for tagging particular genes, long primer PCR was performed under the conditions specified in Tables 4.7.A and B. Note: Due to presence of long primers DNA polymerase was added after heating the sample to 94°C.

Table 4.7.A Long primer PCR reaction (50 μL)

Reagent	Final concentration	Amount [μL]
10X HiFi Reaction buffer (ROCHE)	1X	5
10 mM dNTPs	0.2 mM	1
100% DMSO	2%	1
pDNA (25 ng/μL)	25 ng	1
Primer FW (100 μM)	1 μM	0.5
Primer RV (100 μM)	1 μM	0.5
ddH_2O		40
HiFi Expand Polymerase (ROCHE)		1

Table 4.7.B PCR program for long primer PCR

Step	Temperature	Duration	Repetition
Initial denaturation	94°C	5'	
Denaturation	94°C	15''	30 cycles
Annealing	65°C	30''	
Elongation	72°C	2'	
Final extension	72°C	7'	
Infinitive hold	4°C	∞	

The resulting DNA fragment was directly transfected into *T. brucei* cells by electroporation (Chapter 4.9 Transformation and screening of *T. brucei* cell lines).

Sequences of primers for tagging by Long primer PCR tagging were retrieved from the primer database for tagging each gene of the *T. brucei* genome previously generated by Dr. Samuel Dean (University of Oxford). Primers used in this thesis are listed in the Supplementary Table 9.2.

4.8 *T. brucei* cell lines

4.8.1 Cell lines generation

Cell lines were generated by modifying the SmOxP927 strain of *Trypanosoma brucei brucei* procyclic cells. The SmOxP927 strain is a robust strain, which survives experimental electroporation rather well. In addition, as it has been modified to express T7 RNA polymerase and tetracycline repressor, it enables inducible RNAi (Poon *et al.*, 2012). For more information about produced cell lines, see the Supplementary Table 9.1.

4.8.2 Trypanosome cultivation and handling

Trypanosome cell lines were grown at 28°C. Their density was kept between 3×10^5 cells/mL and 3×10^7 cells/mL. For cultivation SDM-79 medium supplemented with 10% FBS (Brun & Schönenberger, 1979) was used.

All open manipulations of trypanosome cell lines were performed under sterile conditions in a laminar flow cabinet Bio II Advance (Telstar). Cell density was monitored using the cell counter Z2™ COULTER COUNTER® Analyzer (Beckman Coulter Life Sciences). For dilution of measured samples ISOTON® II Diluent solution was used.

4.8.2.1 SDM79 (+ 10% FBS) medium

Premix of SDM79 Powder (25.48 g per liter), and Sodium Bicarbonate (2 g per litter) were dissolved in ddH_2O using H4000-SE Magnetic Stirrer (Benchmark Scientific). Afterwards, the pH was adjusted to 7.3 by Sodium Hydroxide using the pH meter PL-700PV(S) Bench Top Meter (GOnDO Electronic). Thereafter, autoclaved haemin solution (7.5 µg/mL final in 50 mM NaOH) and heat non-inactivated FBS (10% v/v final), were added. In the end, the medium was filtered using 0.22 µm Millipore filter and transferred directly to sterilized borosilicate bottles. The medium was stored at 4°C for a month.

4.8.3 Storing of trypanosome cells

T. brucei cell lines in the exponential phase of growth at approximately 1.5 x 10^7 cells/mL in SDM79 (+ 10% FBS) medium were transferred to Nunc™ cryogenic tubes (#375418, Thermo Scientific™ and subsequently sterile glycerol (10% final) was added. Cells were frozen in a deep freezer (-80°C) and for long-term storage they were stored in liquid nitrogen.

4.8.4 Defrosting of trypanosome cells

After obtaining the cryogenic tube from a liquid nitrogen storage, the tube was filled with a cold (4°C) SDM79 (+ 10% FBS) medium. Thereafter, an entire volume of the cryogenic tube was gently transferred into a cultivation flask containing 10 mL of cold SDM79 (+ 10% FBS) medium and placed into a 28°C incubator.

4.8.5 Disposing of trypanosome cells

For disposal of the parasite, 10% v/v bleach was used. Afterwards, both solid and liquid waste were autoclaved.

4.9 Transfection, selection and screening of *T. brucei* cell lines

4.9.1 Vector linearization

Before the transfection of trypanosome cells (Chapter), vectors had to be linearized. For pEnt5 and pQuadra linearization, NotI and BstXI restriction enzymes were used, respectively. A linearization reaction (60 µL) was mixed on ice according to Table 4.8, and subsequently incubation at 37°C for 90 min. The enzyme was inactivated by heat for 25 min at 75°C. Linearization was validated by ELFO (Chapter 4.1.2). All enzymes used are disclosed in the 4.1.

Table 4.8. Plasmid pEnT5/pQuadra linearization

Reagent	Stock	Final
NEB 3.1 buffer	10 X	1 X
Enzyme	10,000 U	12 U
pDNA		6 µg
ddH_2O		to 60 µL

4.9.2 Transfection of *T. brucei* by electroporation

Stable cell lines were generated by electroporation method. DNA was in a form of a linearized plasmid or a PCR product. For one transfection reaction 1 x 10^7 cells were resuspended in 500 µL of cold 1X electroporation buffer (Table 4.9.A and 4.9.B) and transferred in an electroporation cuvettes (#732-2269, VWR). Following addition of DNA, the electroporation was carried out three times using the BTX

ECM 830 electroporator (BTX®) was set to: Voltage – 2,000 V; Pulse length – 100 μs; Pulses – 1; Interval – 100 ms; Polarity – unipolar.

Table 4.9.A 3X Electroporation buffer

Reagent	Stock	Final
Na_2HPO_4	0.5 M	200 mM
NaH_2PO_4	1 M	70 mM
KCl	1 M	15 mM
Hepes pH 7.3	1 M	150 mM
Qs with dH_2O		to 100 mL

Table 4.9.B 1X Electroporation buffer

Reagent	Stock	Final
3X Roditi Buffer	3X	1X
$CaCl_2$	1.5 mM	150 μM
Qs with dH_2O		to 1 mL

Transfected cells were transferred to 10 mL of prewarmed SDM79 (+10% FBS) medium. After 8 to 16 hrs, an appropriate selectable antibiotic, based on the antibiotic resistance conferred by an electroporated DNA, was added (according to the Table 4.10).

Table 4.10. List of antibiotics

Antibiotics	Manufacturer	Catalogue #	Final concentration	Usage
Blasticidin	InvivoGen	ant-bl-1	20 μg/mL	tagging with pPOT
G418 (geneticin)	InvivoGen	ant-gn-5	20 μg/mL	tagging with pPOT
Hygromycin	InvivoGen	ant-hg-1	50 μg/mL	tagging with pEnT5
Phleomycin	InvivoGen	ant-ph-1	5 μg/mL	KD selection
Doxycycline hyclate	Sigma-Aldrich	D9891-1G	0.5 μg/mL	RNAi induction

4.9.2.1 Handling of transfected cells

Handling of mixed cell population

To obtain clonal populations of transfected *T. brucei* cell lines these were cloned. First, cells were diluted to a density of 1 cell per mL in 20 mL of medium (10 mL of fresh SDM79 medium + 10% FBS mixed with 10 mL of a preconditioned medium plus a selection antibiotic) The preconditioned medium is a medium in which *T. brucei* cells were grown to a stationary phase (around 4 x 10^7 cells/mL) and subsequently cleared of cells by centrifugation and filtration. It has been known to increase the probability of a successful cell division at low cell densities.

Cells diluted in the medium were transferred to a sterile reservoir and pipetted using a multichannel pipette to a 96-well culture plate (200 μL of medium per well). Subsequently, the plates were placed in a wet chamber and cultivated at 28°C. After approximately 10 days a population of dividing cells could be observed in some wells.

4.9.3 Screening of trypanosoma cell lines

After obtaining clones of *T. brucei*, these were screened for positive ones by fluorescence microscopy (see Chapter 4.16).

Results were confirmed by a comparison to the localization database of mNeonGreen fluorescently tagged trypanosome proteins Tryptag.org (Dean *et al.*, 2017).

4.10 gDNA isolation

Isolation of *T. brucei* genomic DNA (gDNA) was performed using the DNeasy® Blood & Tissue Kit" from QIAGEN® following manufacturer's instructions for tissue manipulation. For one isolation 11 mL of *T. brucei* cells in the stationary phase of growth were used. An initial incubation lasted 1 hour and 10 mins at 56°C. Prepared gDNA was stored in 50 µL aliquots at -20°C.

4.11 Tagging validation PCR

An integration of a linearized vector or a PCR product for gene tagging was validated by "tagging validation PCR" (Tables 4.11.A and 4.11.B). Each primer pair was designed such that one primer annealed within an ORF of the respective gene while the other one within the sequence of a tag (see Supplementary Table 9.4.).

Table 4.11.A Tagging validation PCR reaction (10 µL)

Reagent	Final concentration	Amount [µL]
2X ALLin™ Red Taq Mastermix (highQu)	1X	5
gDNA	300 ng	0.2-0.8*
Primer FW (10 µM)	0.4 mM	0.4
Primer RV (10 µM)	0.4 mM	0.4
Qs with ddH_2O		to 10

(* Amount of gDNA depended on an individual concentrations)

Table 4.11.B PCR program for tagging validation PCR

Step	Temperature	Duration	Repetition
Initial denaturation	95°C	2'	
Denaturation	95°C	15''	40 cycles
Annealing	55-65°C*	15''	
Elongation	72°C	15'' per kb	
Final extension	72°C	3'	
Infinitive hold	4°C	∞	

(*Annealing temperature depended on individual primer pair)

4.12 TC-tag labelling

TC-tag (tetracysteine) is specifically binding ReAsH™-EDT_2 reagent (Invitrogen) that becomes fluorescent after interaction with TC-tag. Prior and during labelling, tagged cells were cultivated in SDM79 medium without added serum, because ReAsH is non-specifically binding to serum proteins. After incubation (45 – 60 min) with ReAsH (2 µM final in DMSO) cells were washed twice and treated by BAL wash buffer (Invitrogen) in serum free medium.

4.13 HaloTag labelling

4.13.1 Preparation of biotinylated flagella

Protocol for biotinylation of flagella had to be developed. First, it was determined that biotinylation of Halo-tagged axonemal proteins does not work in living cells. Hence, it was performed on the cytoskeletal fractions prepared as described in the Chapter 4.18. The cytoskeletal fraction was washed in 1X phosphate buffered saline (PBS) (1 mL) and harvested by centrifugation (4,500g, 6 min). The resulting pellet was gently resuspended in 500 µL of 1,000X diluted PEG-Biotin Ligand (Promega) in PBS. Incubation was performed for 45 min at RT, followed by two washing steps with 1 mL PBS. Centrifugation and pipetting led to depolymerisation of subpellicular microtubules leaving relatively clean flagellar cytoskeletons. These could be stored at 4°C for several days. To validate biotinylation of HaloTag-tagged proteins, the samples were incubated at RT for 30 min with Streptavidin – Cy5 Conjugate (Life Technologies) 500X diluted in PBS and visualized by fluorescent microscopy.

4.13.2 TMR ligand and Coumarin ligand staining of HaloTag tagged protein

Live *T. brucei* cells (tagged by HaloTag) in medium were treated by 100X diluted in medium Coumarin ligand or TMR (2,6-dideoxy-4-thiomethyl-beta-d-ribohexopyranoside) ligand (10X diluted in DMSO) for 1 hour in dark conditions at 28°C. Then, three washes in medium were performed in order to wash off non-bounded Coumarin ligand or TMR ligand.

4.13.3 Time course TMR labelling experiment

A well grown culture (app 1 x 10^7 cells per mL in medium SDM79 + 10% FBS) of a POI::mNG-HaloTag tagged cell line was diluted to 1 x 10^6 cells/mL and distributed into 34 wells (200 µL each) on a 96 well plate as described in Figure 4.5.A. Thereafter, TMR ligand (1,000X final dilution) was added to 6 wells and incubated from 45 min to 1 hour (Fig. 4.5.B). After the incubation, TMR-treated cells were washed three times with a fresh medium (with centrifugation at 900g, 4 min between the washes) to remove unbound TMR ligand and transferred into fresh wells (Fig. 4.5.C). Cells for time point t0 = 0 hours after TMR incubation were immediately harvested by centrifugation and further proceeded for imaging like in Chapter 4.15. Simultaneously, cell density was determined as a mean value of cell densities measured for 4 independent wells. For further time points (t1 = 2 hrs, t2 = 4 hrs, t3 = 16 hrs, t4 = 24 hrs, t5 = 48 hrs) cells for imaging and cell density measurements were processed as for t0. However, in addition, at these time points a control cell culture for a direct intensity comparison, which corresponded to t0, was set up. In this case, the cells were incubated with TMR ligand and mitotracker (MTT) for an hour before the respective time point was taken.

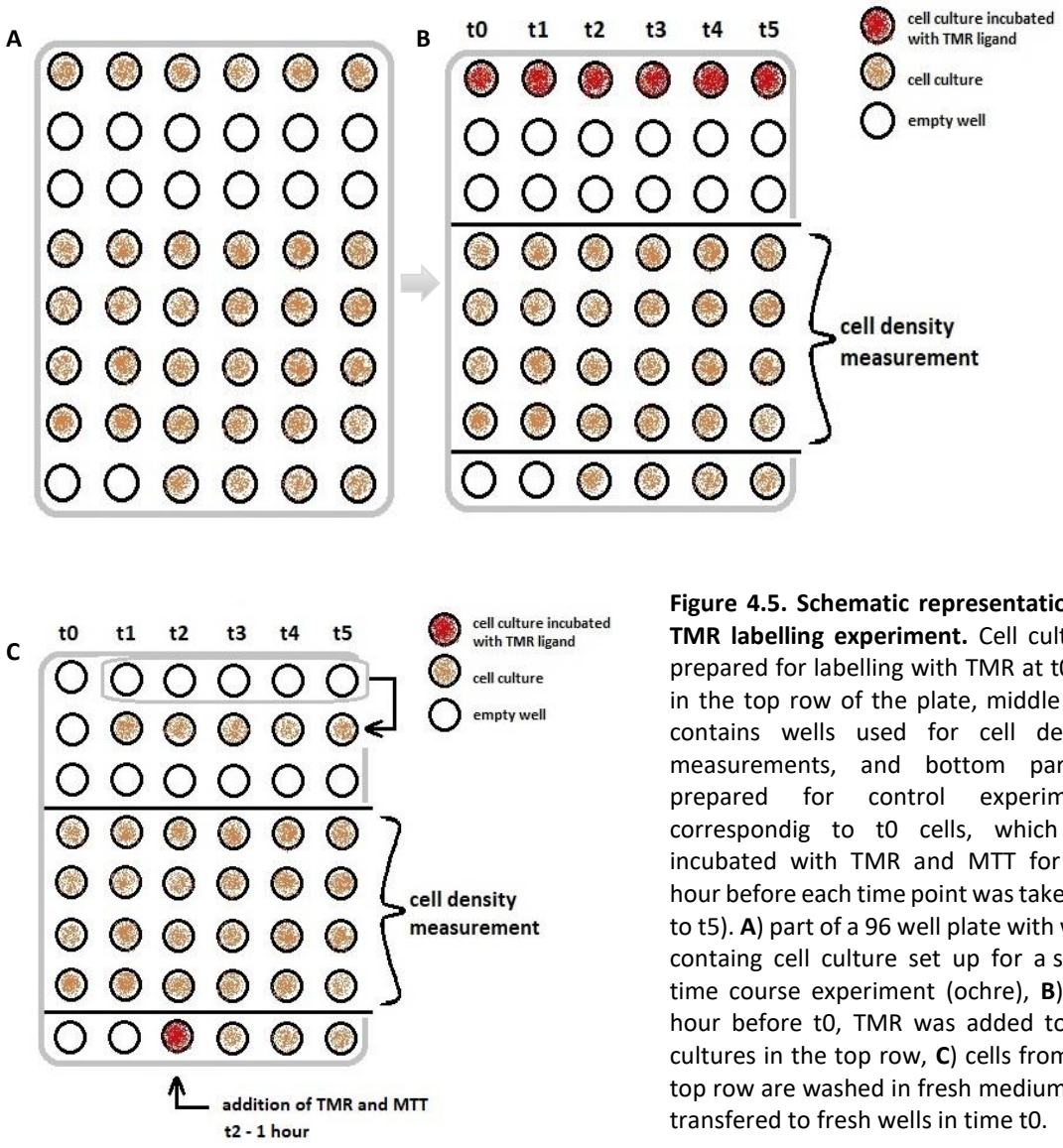

Figure 4.5. Schematic representation of TMR labelling experiment. Cell cultures prepared for labelling with TMR at t0 are in the top row of the plate, middle part contains wells used for cell density measurements, and bottom part is prepared for control experiments correspondig to t0 cells, which are incubated with TMR and MTT for one hour before each time point was taken (t2 to t5). **A**) part of a 96 well plate with wells containg cell culture set up for a single time course experiment (ochre), **B**) one hour before t0, TMR was added to cell cultures in the top row, **C**) cells from the top row are washed in fresh medium and transfered to fresh wells in time t0.

4.14 Fluorescence staining

Preparation of two cell populations imaged in the same field of view by staining mitochondria in one population to distinguish between them.

4.14.1 Hoechst staining of DNA

Staining of DNA by Hoechst 33342 Solution (#62249, Thermo Fisher). One cell population was stained with Hoechst from experimentally set timing: 1 to 10 min (working solution 1 µg/mL), both in PBS or medium. Then, cells were washed two times and mixed with an unstained population of cells. After the fixation step, cells were observed under the microscope.

4.14.2 Mitotracker staining of mitochondria

Two fluorescent dyes staining mitochondria were tested for this purpose. Mitotracker CMX Ros (final conc. 20 nM) and mitotracker Deep Red (final conc. 50 nM) (both gift from Dr. Tomáš Mráček, Institute of Physiology CAS, CR). Incubation of living cells in a medium with a dye was carried out for 45 min in the

dark at 28°C. Next, 1 mL of PBS was added and cells were centrifuged for 5 min at 900g. Than two PBS washes followed (900g, 5 min), continued by methanol fixation step.

4.14.3 Immunofluorescence assay

Cells were harvested at 48, 66, and 72 hrs after RNAi induction (see Chapter 4.5.1.1). Afterwards, cells were settled on a glass slide in wells with hydrophobic borders (Chapter 4.15). Glass slides were treated by blocking solution (10% FBS in PBS v/v) for 1 hour in the dark. Individual wells were incubated with a primary antibody (See Table 4.12) diluted by 1% BSA in PBS (1 hour at RT in the dark). Subsequently, 5 min washes were conducted for five times by immersing the slides in a Coplin jar with fresh 1X PBS. Afterwards, the secondary anti Mouse IgG H + L647 antibody (250 x diluted in 1% BSA in PBS) was used for 1 hour at RT in the dark. Washes were performed like in the case of primary antibodies. Glass slides ware subsequently mounted as in Chapter 4.15.

Table 4.12. List of antibodies

Antibody	Organism/Host	Clonality	Type	Manufacturer	Catalogue #
Anti-HaloTag® pAb	Rabbit	Polyclonal	primary	Promega	G9281
L8C4 (α-PFR2) (Kohl *et al.*, 1999)	Mouse	Monoclonal	primary	From K.Gull	//
mNeonGreen antibody	Mouse	Monoclonal	primary	Chromotek	32f6-100
MAb25	Mouse	Monoclonal	primary	from D. Robinson	//
M2DH62 (Abeywickrema *et al.*, 2019)	Mouse	Monoclonal	primary	From K.Gull	//
HRP anti-mouse IgG	Rabbit	Monoclonal	secondary	Sigma	A9044
Alexa 647 anti-Mouse IgG (H+L)	Goat	Polyclonal	secondary	Thermo Scientific	A21235

4.15 Preparation of samples for microscopy

4.15.1 Methanol fixation

Microscopy slide glass (76 x 26 mm, Thermo Scientific) was rinsed in ethanol (clean, 70%) and set to dry in a dust-free chamber. On one side of the glass slide, chambers were drown with a hydrophobic barrier pen (Dako). Meanwhile, cells were collected by centrifugation, washed with PBS and resuspended to approximately 1 x 10^7 cells/mi in PBS. 50 µL of cell suspension were then pipetted into chambers with a hydrophobic border. Cell adhesion to the surface of the glass slide was monitored under an inverted light microscope (Zeiss Axio Vert.A1). Depending on the cell density, cells were let to adhere from 30 sec to 5 min. Thereafter, an excess of PBS was removed from the glass slides, which were immersed in -20°C methanol in a Coplin jar. Methanol incubation was carried out for 20 min at -20°C. Afterwards, the slides were immersed in PBS in a Coplin jar for minimum of 20 min. Fixed cells on slides were stored in PBS (1X) for up to 2 days at 4°C.

4.15.2 Mounting samples for microscopy

Immediately after removing an excess of PBS approximately 5 µL of a mounting medium was added to every sample. The composition of the mounting medium was as follows: glycerol (90%), Dabco (10% w/v 1,4-diazobicyclo(2,2,2)octane in glycerol), and a fluorescent stain DAPI (4′,6-diamidino-2-phenylindole) (Sigma) for counterstaining DNA. In cases of the DNA staining with Hoechst fluorescent dye (Chapter 4.14.1), a mounting medium without DAPI was used. DAPI-Fluoromont-G mounting medium (Southern Biotech) was also used. Samples were covered with a coverslip (thickness, company), which were attached to a slide using nail polish.

4.16 Fluorescence microscopy

4.16.1 Image acquisition

All the imaging was carried out on AXIOPLAN 2 imaging microscope (Carl Zeiss, ser# 3511001456), with a 40X Plan-NEOFLUAR, 1.3 Oil, and 100X Plan-APOCHROMAT, 1.4 Oil objective lenses (Carl Zeiss). Acquisition of images was performed using a Zyla 4.2 sCMOS camera (ANDOR) and Micro-manager software. An immersion oil Immersol™ 518 F (Carl Zeiss) with a refractive index of 1.518 was used. Also, microscope cover glasses (Marienfeld) give RI = 1.5.

Filter sets used for fluorescence imaging are specified in Table 4.13. For a multi-channel acquisition images were taken in the order as present in Table 4.13 (from top to bottom). In addition, a phase contrast image of each field of view was also obtained.

Table 4.13. List of fluorescent filter sets and their EX/EM spectra

Fluorescent filter	Zeiss filter set	Excitation [nm]	Beam splitter [nm]	Emmision [nm]	Exposure time [ms]
TRITC	43	BP545/25	FT570	BP605/70	2,000
FITC	38	BP470/40	FT495	BP525/50	2,000
Cy5	26	BP575-625	FT645	BP660-710	200 - 300
DAPI	49	G363	FT395	BP445/50	30

4.16.2 Image correction

To correct for an unevenness of fluorescent illumination images in the FITC and TRITC channels with soluble fluorescein (100 mg/mL in water) or rose Bengal (100 mg/mL in water) were acquired. Using Z-projection tool the mean intensity was calculated for 20 images of each channel to create a median flat-field image. Similarly, for both channels, the so-called dark images were acquired (no light reaching the camera) and their average calculated. Next, the dark image was subtracted from mean flat-field image for both channels. The obtained correction image was subtracted from every acquired image.

4.16.3 Image analysis

Images were processed and analysed by Java based program ImageJ (Schneider *et. al*, 2012). Flagella were manually outlined by the segmented line tool (width 8) using the mNG fluorescence image. The line has been drawn from the centre of the kinetoplast towards flagellar tip and beyond (Fig. 4.6.). Generated intensity plots were transferred to Excel, where they were analysed. Further, background values were measured separately for each flagellum in both (TRITC and FITC) fluorescent channels. An average background value was subtracted from every intensity value of a flagellum. Created data sets were normalized to the 0 – 1 range [(value - min)/(max - min)].

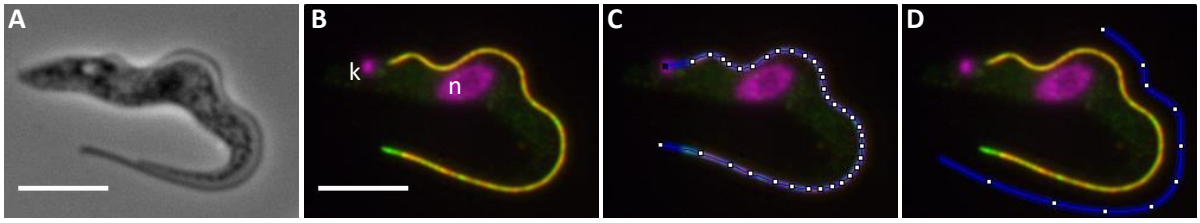

Figure 4.6. Intensities measurements of fluorescently marked flagellar protein of interest (POI)
Example of intensities measurements in both green and red channels for flagellum (**C**) and background (**D**). **A**) Phase contrast photo of a *T. brucei* cell that was analysed. **B-D**) Fluorescence images of analysed *T. brucei* cell, where POI is tagged endogenously (green) and subsequently same POI is marked in t0 by fluorescence TMR label (red). DAPI (magenta) is visualising DNA: n = nucleus, and k = kinetoplast. The cell is in 4 hours after labelling with TMR and washing excess of it out of the cell. **C**,**D**) All measurements were done in ImageJ. **C**) The blue line (width 8) has been drawn from the middle of the kinetoplast towards flagellar tip, crossing green signal. Data for both intensities were obtained. **D**) The blue line (width 8) has been drawn near the flagellum for measurement of background intensities for both fluorescent channels. Scale bars represent 5 μm.

4.16.3.1 Selection of cells for analysis

In general, all flagella with TMR signal within a particular image were taken for analysis. However, flagella with particularly blurred signal in their distal half (due to being out of focus) or those overlapping in their distal half with another flagellum were omitted from image analysis.

4.17 Analysis of fluorescence intensity signal

To analyse the fluorescence intensity profile automatically, a custom-made R script, written and developed by Luděk Štěpánek Ph.D., was used. This approach is described in the Chapter Result in detail.

4.18 Cytoskeletal preparation

2 x 10^8 *T. brucei* cells were collected by centrifugation (1,500g for 10 min, @RT). Cells in the pellet were washed with PBS (1X). After centrifugation (1,500g for 10 min, @RT) supernatant was carefully discarded by pipetting. Cells were treated (for 3 min) with PEME buffer (100 mM PIPES, 2 mM EGTA, 1 mM $MgSO_4$, 0.1 mM EDTA, pH 6.9) with the addition of 0.5% IGEPAL® (Sigma-Aldrich), protease inhibitors (Table 4.14), and DNase – Benzonase (1 µL). Cytoskeleton fraction was pelleted by centrifugation (3,000g for 5 min, @RT), and washed with PBS (1X).

Table 4.14. Protease inhibitors

Protease inhibitor	Manufacturer	Catalogue #	Final conc.
Leupeptin hemisulfate salt	Sigma	//	50 μM
Pepstatin A	Sigma	P5318-25MG	7.5 μM
PMSF	Roche	10837091001	500 μM
E-64-d	Enzo Life Sciences	BML-PI107	5 μM

4.19 Protein separation and detection

For separation and detection of tagged proteins, sodium dodecyl sulfate – polyacrylamide gel electrophoresis (SDS-PAGE) (Laemmli, 1970) and Western blot methods were adapted. Three types of western blot protocols were tested; turbo blotting, semi-dry blotting, and wet blotting. The best results were obtained by the wet-blot protocol.

4.19.1 Sample preparation

Approximately 2 x 10^8 cells were harvested by centrifugation (1,500g for 10 min @RT). Then the cells were washed with PBS and spun at 1,500g for 10 min @RT. Pelleted cells were first treated like in the chapter 4.18., except for the PBS wash in the last step. Subsequently, cells were fractionated. From the soluble protein fraction, a sample of 100 μL was collected and supplemented with 5X SDS Sample Buffer (Table 4.15) to final concentration 1X. Another 50 μL of soluble protein fraction was stored for protein concentration measurements. The pellet was dissolved in 48 μL of 1X PBS. 10 μL of the pellet was retained for protein concentration measurement. The rest of the pellet fraction was supplemented with 5X SDS Sample Buffer to final concentration 1X. Subsequently, samples in 1X SDS Sample Buffer were heated to 85°C for 4 min.

Table 4.15. 5X SDS sample buffer

Reagent	Final concentration	Amount
Tris-HCl pH 6.8 (1 M)	225 mM	4.5 mL
Glycerol (100%)	20%	4 mL
SDS (20%)	5%	5 mL
Bromophenol blue	0.05%	10 mg
β-mercaptoethanol (100%)	1 M	1.5626 mL
Qs with ddH_2O		20 mL

4.19.2 SDS-PAGE

In the case of semi-dry and turbo blot, manually casted gels were used. While, in the case of wet blot, pre-cast Mini-PROTEAN® TGX™ 4 – 15% (Bio-Rad Laboratories; cut. # 456-1085) gels were used.

4.19.2.1 Polyacrylamide gel casting

Polyacrylamide gels were prepared using Mini-PROTEAN® Short Plates equipment from Bio-Rad with 1.5 mm integrated spacers. First, separating gel was casted according to Table 4.16.A and set to solidify for 20 min. After that, upper stacking gel (Table 4.16.B) was casted. A comb was inserted and the gel was set to solidify for 30 min at RT.

Table 4.16.A Lower separating gel (10%)

Reagent	Final concentration	Amount [µL]
ddH_20		3,043
Tris (0.5 M, pH 6.8) + SDS		1,875
acrylamide:bisacrylamide (29:1) (30% w/v)	10%	2,500
TEMED		8
APS (10% w/v)	0.01%	75

Table 4.16.B Upper stacking gel (4%)

Reagent	Final concentration	Amount [µL]
ddH_20		1,814
Tris (0.5 M, pH 6.8) + SDS		750
acrylamide:bisacrylamide (29:1) (30% w/v)	4%	400
TEMED		6
APS (10% w/v)	0.01%	30

4.19.2.2 Sample loading

Before loading on the gel, samples in 1X SDS Sample Buffer were heated to 85°C for 3 min. As a protein size marker, Color Prestained Protein Standard (#P7712L, NEB) was used (Fig. 4.7). A cell equivalent of 1 x 10^7 cells and 3 x 10^7 cells was loaded for a soluble and pellet fractions, respectively.

4.19.2.3 SDS-PAGE protocol

Vertical electrophoresis was running in 1X running buffer (diluted from 10X; acc. to Table 4.17) with constant voltage of 100 V in a Mini Bio-Rad electrophoresis apparatus (Bio-Rad).

Table 4.17. 10X running buffer

Reagent	Final concentration	Amount
Trizma (1 M)	250 mM	30.285 g
Glycine (1 M)	1.92 M	144.13 g
SDS (20%)	1%	50 mL
Qs with ddH_2O		1,000 mL

4.19.3 Western blot

In semi-dry and wet blotting approaches, 1X transfer buffer for large proteins was used (prepared according to Tables 4.18.A and 4.18.B).

Table 4.18.A 10X transfer buffer

Reagent	Final concentration	Amount
Tris (1 M)	250 mM	30.285 g
Glycine (1 M)	1.92 M	144.13 g
Qs with ddH_2O		to 1,000 mL

Table 4.18.B 1X transfer buffer for large proteins

Reagent	Final concentration	Amount [mL]
10X transfer buffer	1X	100
SDS (20%)	0.01%	0.5
Methanol (100%)	2%	20
Qs with ddH_2O		to 1,000

4.19.3.1 Turbo blotting

A prepared blotting sandwich (3X tissue, a nitrocellulose membrane, SDS-PAGE gel, 3X tissue) was wetted by 1X turbo blotting buffer (48 mM Tris, 20 mM Hepes, 20% EtOH). A set program for 1.5 MM Gel, 10 min employed using a Trans-Blot® Turbo™ Transfer system (Bio-Rad).

4.19.3.2 Semi-dry blotting

A blotting sandwich (3X filter paper, a nitrocellulose membrane, SDS-PAGE gel, 3X filter paper) was rinsed in 1X transfer buffer (Table 4.18.B) and placed to a TE77X semi-dry transfer unit (Hoefer). Protein transfer was performed for 90 min at 34 mA/gel.

4.19.3.3 Wet blotting

A prepared blotting sandwich (sponge, 3X wet chromatographic paper, SDS-PAGE gel, nitrocellulose membrane, 3X wet chromatographic paper, sponge) was soaked in 1X transfer buffer (Table 4.18.B) and enclosed in a plastic holder (Bio-Rad). A tank was filled with 1X transfer buffer and a the holder with the blotting sandwich was placed into it together with a filled ice container. Protein transfer was performed for 2 hrs at 360 mA (constant).

4.19.4 Ponceau staining of membranes

After the transfer, membranes were stained for 3 min with Ponceau staining (AdvanStain Ponceau - Advansta) to validate the transfer. Afterwards, membranes were washed 3 times in 5% milk in PBS-T (Table 4.19.) by shaking for 5 min at RT.

Table 4.19. PBS-T recipe

Reagent	Final concentration	Amount [mL]
10X PBS	1X	500
ddH_2O		4,500
Tween 20	0.10%	5

4.19.5 Blocking of membranes

The membrane was incubated in 10% milk in PBS-T for 1 hour at RT on a shaker. Alternatively, incubation was performed in 5% milk (in PBS-T) O/N at 4°C. Afterwards, three washes (5 min, at RT) with 1% milk in PBS-T were performed on a shaker.

4.19.6 Incubation with primary antibody

Membranes were incubated for 1 hour while shaking with the primary antibody- Mouse monoclonal antibody to mNeonGreen protein ([32F6] Chromotek) 1,000X diluted in 1% milk in PBS-T. Then, three washes of 15 min with 1% milk in PBS-T were performed.

4.19.7 Incubation with secondary antibody

Membranes were incubated with the secondary antibody– Rabbit anti-mouse IgG whole M conjugated with HRP (#A9044, Sigma) diluted 5,000X 1% milk in PBS-T for 1 hour sealed in a plastic foil bag. Thereafter, three washes for 15 min with PBS-T on shaker were performed.

4.19.8 Detection of proteins by chemiluminescence

Horseradish peroxidase (conjugated to the secondary antibody) was visualized by Enhanced Chemiluminescence Substrate (#NEL103001EA, PerkinElmer). Signal detection was carried out by Azure cSeries 300 using cSeries Capture software.

4.19.9 Visualisation of proteins in gels

This protocol was applied for visualisation of proteins in the polyacrylamide gel e.g. to determine the efficiency of the transfer to membranes. Immediately after the transfer, polyacrylamide gels were soaked in water three times (5 min each). Then, the gels were incubated in ddH_2O, acetic acid and metOH in a ratio 4:1:5. After that, gel was stained with Coomassie Brilliant Blue R-250 Staining Solution (Bio-Rad, #1610437/#1610436) for 1 to 2 hours at RT on a shaker. Finally, the gels were destained in a solution of dH_2O, acetic acid, and metOH in ratio 6.75:0.75:2.5, until areas of the gels without proteins became devoid of the dye.

5 Results

5.1 Selection and identification of axonemal proteins to be included in the study

Proteins for this study were selected according to the information from available literature sources. First, representatives from every major axonemal component were picked. Among those medically important proteins were preferred (see the chapter about ciliopathies).

Following proteins were selected: TMD associated proteins from ribbon Rib72 (Tb927.10.7690) (Nguyen *et al.*, 2013) and inner junction FAP20 (Tb927.10.2190) (Hodges *et al*., 2011); RS proteins for head RSP4/6 (Tb927.11.4480), neck RSP2 (Tb927.5.2850), and stalk RSP3 (Tb927.11.1150); N-DRC proteins of two subunits DRC4 (Tb927.9.15050) (El-Sayed *et al.*, 2005), and DCR2 (Tb927.11.7240) (Kabututu *et al.*, 2010); CA proteins from bridge structure PF20 (Tb927.10.13960), C1 projection – PF16 (Tb927.1.2670), and C2b projection – Hydin (Tb927.6.3150) (Dawe *et al.*, 2007); proteins of both axonemal dynein arms: ODA – ODA2 (Tb927.3.930) (Edwards *et al.*, 2018), and IDA – IAD (Tb927.4.870) (Wickstead & Gull, 2007); peri-axonemal structure component CFAP43 (Tb927.4.5380) (Coutton *et al.*, 2018); and PFR protein PFR2-2 (Tb927.8.4980) (Lacomble *et al.*, 2009).

Subsequently orthologs of these proteins were identified in *T. brucei*. All the polypeptide sequences were obtained from the National Center for Biotechnology Information (NCBI) database. Basic Local Alignment Tool (BLAST) was used for identification of a protein encoded by the *T. brucei* genome with the Reciprocal-best-BLAST (RBB) match. With this approach the following trypanosome proteins were identified: Hydin Tb927.6.3150, pBLAST human to *T. brucei*, first hit with values: E value = 5e-111, identity = 29%. PBLAST *T. brucei* to human: E value = 2e-110, identity = 29%, the second best hit. This was previously published by Dawe *et al.*, 2007. FAP20 Tb927.10.2190, pBLAST human to *T. brucei* - first hit: E value = 1e-122, ident = 83%. PBLAST *T. brucei* to human - first hit: E value = 1e-124, ident = 81%. This was previously published by (Hodges *et al.*, 2011). Others were characterised by tritrypdb.org database.

In *T. brucei* genome, a large duplication and transposition event resulted into formation of partial duplicated chromosomes 4 and 8 (Jackson, 2007). This led to generation of two paralogous genes – Tb927.4.5380 and Tb927.8.4720. Hence, it was necessary to recognize between them. gDNA of created cell line was isolated, PCR was done with primers MP058 (in

tag gene) and MP061 (in gene of interest). Subsequent PCR product was sent for sequencing, which confirmed that the correct sequence has been tagged by mNG-HaloTag construct.

5.2 Preparation of *T. brucei* cell lines expressing fluorescently tagged axonemal proteins

Cell lines expressing tagged proteins from endogenous loci were prepared via homologous recombination using either linearized vectors or PCR products (see materials for details). Examples of both types of prepared DNA are shown in Fig. 5.1.

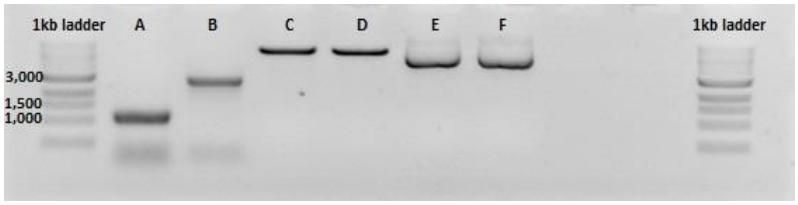

Figure 5.1. Example of control ELFO of DNA used for tagging approaches. A,B) Long primer PCR reaction; **C,D**) linearized pDNA – vector after restriction; **E,F**) cccDNA - vector before restriction. **A**) A long primer PCR product from pPOTv7 for tagging of α-tubulin (Tb927.1.2360) with TC tag. **B**) A long primer PCR product from pPOTv7 for tagging of DRC4 (Tb927.9.15050) with mNG-HaloTag. **C,E**) pDNA construct of pEnT5 for tagging of Hydin (Tb927.6.3150) with mNG-HaloTag. **D,F**) pEnT5 tagging of FAP20 (Tb927.10.2190) with mNG-HaloTag. 1kb ladder = DNA length marker in nt.

SmOxP927 cells were transfected with vectors or PCR products by electroporation, followed by cloning and selection with antibiotics (see 4.9.). Resulting clonal cell lines were examined under a microscope and observed protein localisations compared to the Tryptag.org database of localisations of fluorescently tagged proteins encoded in the genome of *T. brucei*. For all tagged proteins the localizations were consistent with the Tryptag.

Integration of the tagging cassette into the correct place in the genome was validated by PCR (see 4.12.) on isolated genomic DNA using a primer specific for the tag and a primer specific for the tagged ORF (Fig. 5.2.).

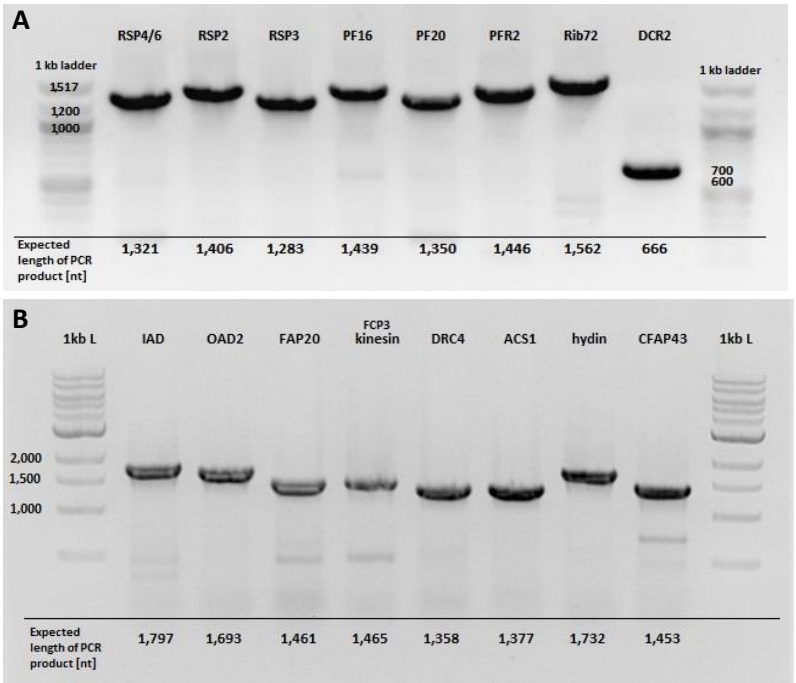

Figure 5.2. Validation of correct integration of tagging cassettes into the genome by PCR and ELFO. A,B) Visualisation of PCR products in the agarose gel after separation by ELFO. 1kb Ladder was used (DNA fragments length on left in nt). See Table 5.1.

Table 5.1. Proteins tagged by mNG-HaloTag and their gene DB accession numbers with estimated "tagging validation PCR" products lengths in nt.

Protein name	Gene DB accession number	PCR product length [nt]
RSP4/6	**Tb927.11.4480**	1,321
RSP2	**Tb927.5.2850**	1,406
RSP3	**Tb927.11.1150**	1,283
IAD	**Tb927.4.870**	1,797
OAD2	**Tb927.3.930**	1,693
PF16	**Tb927.1.2670**	1,439
PF20	**Tb927.10.13960**	1,350
FAP20	**Tb927.10.2190**	1,461
FCP3	**Tb927.10.890**	1,465
DRC4	**Tb927.9.15050**	1,358
DCR2	**Tb927.11.7240**	666
PFR2-2	**Tb927.8.4980**	1,446
Rib72	**Tb927.10.7690**	1,562
ACS1	**Tb927.7.6180**	1,377
Hydin	**Tb927.6.3150**	1,732
CFAP43	**Tb927.4.5380**	1,453

5.3 Western blot validation of expression of tagged POI

To test whether tagged POIs were expressed, SDS-PAGE and western blot analysis of cytoskeletal fraction using antibody against the mNG tag was performed for a selected POIs. As shown in Fig. 5.3. tagged proteins PF20, FAP20, ACS1, DCR3, PF16, DRC4, RSP4/6, PFR2, OAD2, IAD, CFAP43, and Rib72 were expressed and were of a predicted molecular weight (see Table 5.2.). Tagged Hydin was present, but its molecular weight was considerably lower than expected. The nature of this discrepancy is unclear, but may be caused by proteolytic processing of the protein. Of those assessed by western blotting protein RSP2 could not be detected; this could be caused by the inability of these proteins to be separated by SDS-PAGE or transferred to a membrane. Alternatively, this could reflect their levels being below the detection range of the used approach.

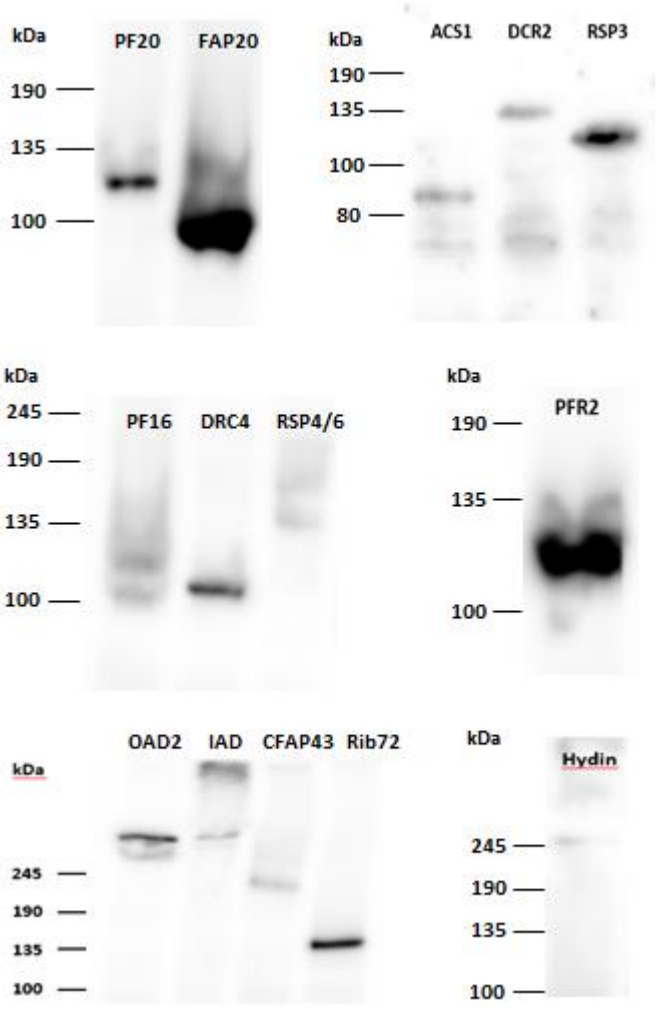

Figure 5.3. Set of western blots. Loaded proteins from pellet fraction with protein marker in kDa.

Table 5.2 List of protein of interest molecular weight (Mw) in kDa including Mw of added tags

Protein name	Gene DB accession number	Molecular weight [kDa]	Mw with tags [kDa]
RSP4/6	**Tb927.11.4480**	66.92	128.04
RSP2	**Tb927.5.2850**	57.6	118.72
RSP3	**Tb927.11.1150**	39.39	100.51
IAD	**Tb927.4.870**	510.19	571.31
OAD2	**Tb927.3.930**	531.5	592.62
PF16	**Tb927.1.2670**	56.14	117.26
PF20	**Tb927.10.13960**	65.58	126.7
FAP20	**Tb927.10.2190**	34.6	95.72
DRC4	**Tb927.9.15050**	54.18	115.3
DCR2	**Tb927.11.7240**	58.68	119.8
PFR2-2	**Tb927.8.4980**	69.61	130.73
Rib72	**Tb927.10.7690**	82.85	143.97
ACS1	**Tb927.7.6180**	29.96	91.08
Hydin	**Tb927.6.3150**	501.1	562.22
CFAP43	**Tb927.4.5380**	164.98	226.1

5.4 Validation of tagging of correct proteins by RNAi depletion

To further validate that correct proteins were tagged, cell lines with inducible RNAi against two RSP proteins (RSP3 and RSP4/6) were created in the respective tagged background. Two RNAi competent clonal cell lines were analysed for each of the proteins. In Fig. 5.4. two cells fixed 48 hours after RNAi induction are displayed. There is no mNG signal detected in the flagellum of the cell on the left, indicating that RSP4/6 protein is not present in this cell due to RNAi. However, this cell does still form a flagellum, as apparent from the phase contrast image and from immunofluorescence staining with an antibody against PFR (Fig. 5.4B). On the other hand, the cell on the right possesses a strong mNG signal in both old and new flagella. It has been reported that in the used parental cell line, SMOXP9, expression levels of transgenes considerably even within a clonal population (Poon *et al.*, 2012). Hence, it is possible that this cell represents a cell with a very low expression of hairpin RNA targeting RSP4/6.

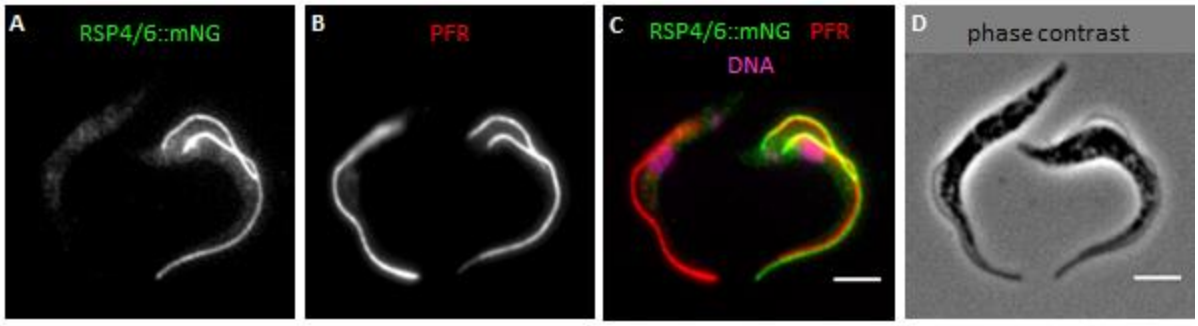

Figure 5.4. mNG::RSP4/6 (KD) cell line in 48 hrs after RNAi induction. A-D) KD cell (left) and RNAi resistant cell (right). **A**) RSP4/6::mNG; **B**) PFR; **C**) merge: RSP4/6::mNG (green), antibody against PFR – L8C4 (red), DNA stained by DAPI (magenta); **D**) Phase contrast. Scale bars represent 5 µm.

Table 5.3. Number of induced and RNAi resistant cells (cells with green signal). mNG::RSP-RNAi cell lines in three time points (48, 66, and 72 hrs) after RNAi induction. mNG = mNeonGreen, KD = knock down, cl = clone

Cell line	Time in hrs (after induction)	KD cells (without mNG signal)	RNAi resistant cells (with mNG signal)	Ratio of RNAi resistant cells to all (%)
RSP4/6::mNG – RNAi (cl01)	48	277	115	**28.2**
RSP4/6::mNG – RNAi (cl01)	66	196	46	**19.0**
RSP4/6::mNG – RNAi (cl01)	72	251	82	**24.6**
RSP4/6::mNG – RNAi (cl02)	48	492	115	**18.9**
RSP4/6::mNG – RNAi (cl02)	66	267	73	**21.5**
RSP4/6::mNG – RNAi (cl02)	72	369	89	**19.4**
RSP3::mNG – RNAi (cl01)	48	229	56	**19.6**
RSP3::mNG – RNAi (cl01)	66	721	299	**29.3**
RSP3::mNG – RNAi (cl01)	72	632	224	**26.2**
RSP3::mNG – RNAi (cl02)	48	166	61	**26.9**
RSP3::mNG – RNAi (cl02)	66	438	119	**21.4**
RSP3::mNG – RNAi (cl02)	72	486	368	**43.1**

Proportions of the cells with mNG signal in their flagella (i.e. RNAi resistant cells) in cell population were further quantified over time. Data were obtained at 48, 66, and 72 hours after RNAi induction of the four cell cultures (two clones of RSP4/6 KD and two clones of RSP3 KD). Results are summarised in Table 5.3. The proportion of cells with mNG signal did not decrease over time, as expected if these were only cells present in the population before RNAi induction, given the logarithmic growth of the culture over this time period. Hence, some of the cells with mNG signal must stem from division of RNAi resistant cells during the course of the experiment.

5.5 Depletion of RSP proteins causes shortening of the flagellum

At later time points after RNAi induction a substantial difference in the length of flagella between cells with and without mNG signal was observed (Fig. 5.6.; Table 5.4.). Visualisation of flagella was done by the MAb25 antibody against an axonemal protein (Fig. 5.5.).

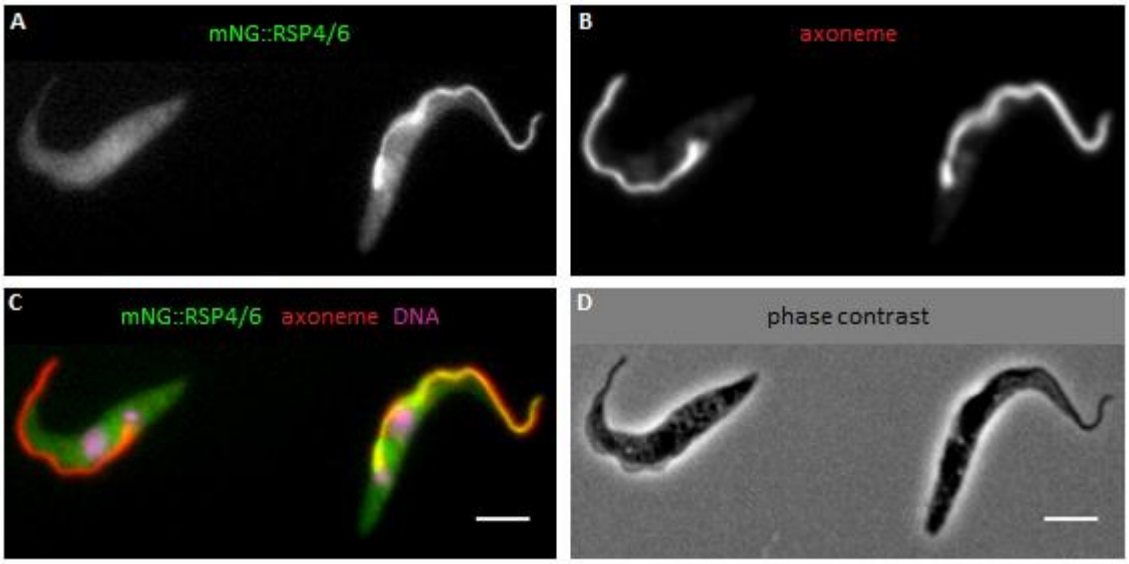

Figure 5.5. RSP4/6 (KD) cell line in 66 hrs after RNAi induction. A cell without the RSP4/6 protein (left) and a cell with the protein in the flagellum (right): **A**) RSP4/6::mNG signal; **B**) an axoneme stained by Mab25 antibody; **C**) merge: mNG::RSP4/6 (green), axoneme (red), DNA stained by DAPI (magenta); **D**) phase contrast. Scale bars represent 5 µm.

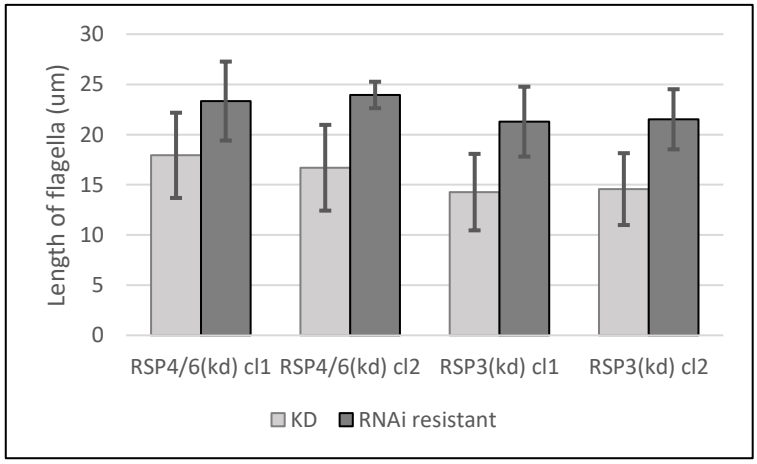

Figure 5.6. Length of flagella in 66 hrs after RNAi induction. KD = knock down phenotype, cl = clone culture

Table 5.4. Number of of analysed cells in Fig. 5.6.; cl = clone

Cell line	KD phenotype	RNAi resistant cells
RSP4/6-KD cl01	40	12
RSP4/6-KD cl02	75	12
RSP3-KD cl01	40	20
RSP3-KD cl02	32	23

Depletion of both RSP4/6 an RSP3 led to a mild decrease in a cell culture growth rate. This is apparent from cumulative growth curves shown in Figures 5.7.A and 5.7.B. Previously, it was shown that *T. brucei* cells with impaired flagellar motility, including cells depleted of RSP3, have problems to undergo cytokinesis. Most likely because the flagellar motility is involved in resolution of two daughters at the end of cytokinesis (Ralston *et al.*, 2005; Branche *et al.*, 2006). This can be overcome by growing the culture under shaking conditions (Ralston *et al.*, 2005; Branche *et al.*, 2006). To test this, the cells were cultured shaking at 80 rpm. However, no restoration of the growth rates to those of cultures not depleted of the RSP proteins was observed (Fig 5.7.).

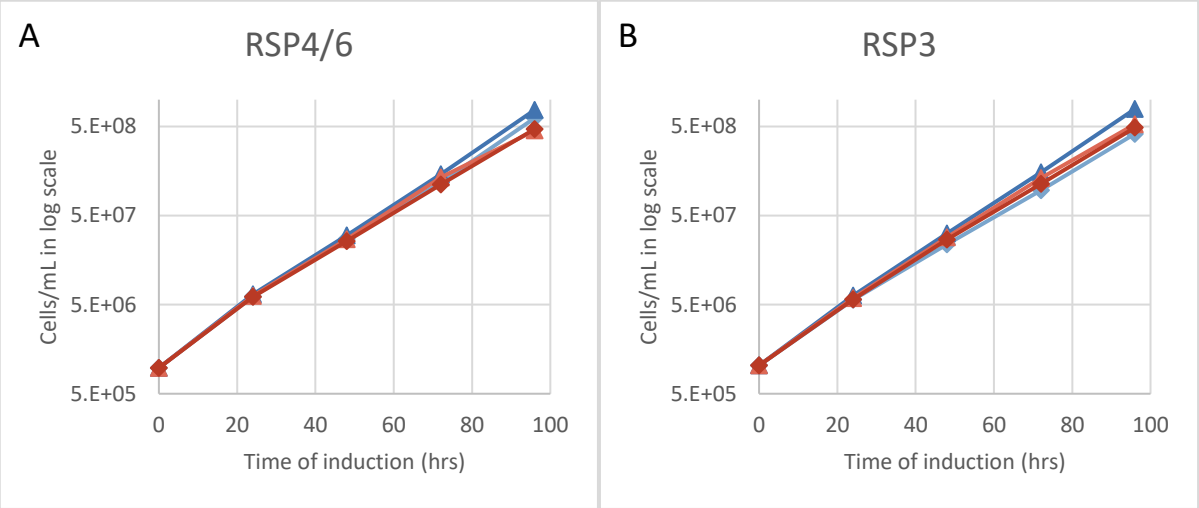

Figure 5.7. Non-induced (blue) and induced (red) cells in shaking condition (pale) and non-shaking conditions (dark).

5.6 Labelling of proteins with Halo ligands

A fluorescent protein tag, mNeonGreen, was used to visualize an entire population of a POI in a cell. A self-labelling tag, HaloTag, was employed to monitor behaviour of a cohort of molecules of the POI present in the cell at a specific time point (Fig 5.8.). As the interaction of the HaloTag with its fluorescently labelled ligand is covalent, there is no artificial decrease of labelling over time due to the ligand unbinding. The HaloTag approach was successfully applied in the past in *T. brucei* to study assembly and turnover of cytoskeletal structures (Dean *et al.*, 2016).

5.6.1 HaloTag labelling approach

Small (33 kDa), monomeric enzyme haloalkane dehalogenase originated from bacteria *Rhodococcus rhodochrous* (Kulakova *et al*., 1997), was modified to fusion tag – HaloTag, which uses its ability to covalently bind the substrate through chloroalkane groups. This stable ester bond displays high specificity and occurs quickly (Encell *et al.*, 2012). Possession accessibility of chloroalkane group, in the form of a chloroalkane linker, creates a variety of potential binding synthetics substrates. These substrates are diverse from fluorescent labels, which are available in various colours, to reactive ligands, or surfaces. This attribute makes HaloTag technology genuinely modular system, which employs an individual DNA vector (Los *et al*., 2008).

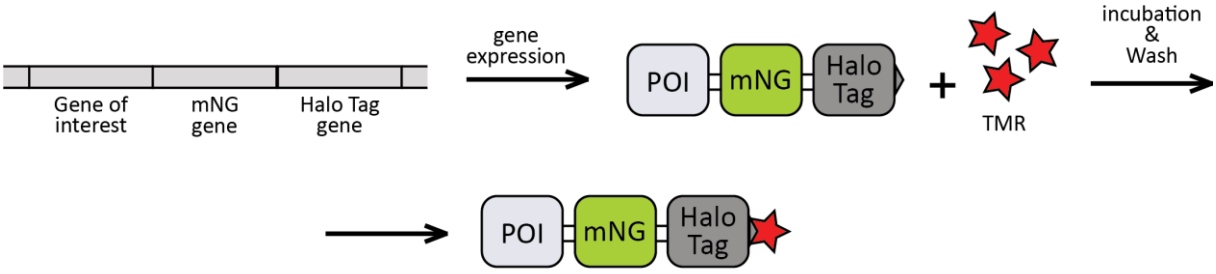

Figure 5.8. Schematic model of dual mNeonGreen - HaloTag labelling approach.
Firstly, DNA construct of mNG-HaloTag was incorporated into DNA, creating one expression casette with the gene of interest. Secondly, after gene expression, POI::mNG-HaloTag fusion protein (green fluorescence) was incubated with TMR HaloTag ligand (red fluorescence). Thirdly, washing procedure got rid of non-bounded TMR. Immediatelly after, all tagged POI in the cell was emerging green and red signal simultaneously.

5.7 mNG-HaloTag tagged proteins localise to the flagellum and the tag is functional

First, generated cell lines were incubated with TMR-Halo ligand for 1 hour (see 4.13). Excess TMR ligand was washed out, and cells were observed by fluorescent microscopy. The most prominent TMR signal was in all cases observed in the flagellum. Both mNG and TMR signals generally overlapped (Fig. 5.9.), demonstrating that the tagging does not interfere with localisation of tagged proteins and that the HaloTag is functional.

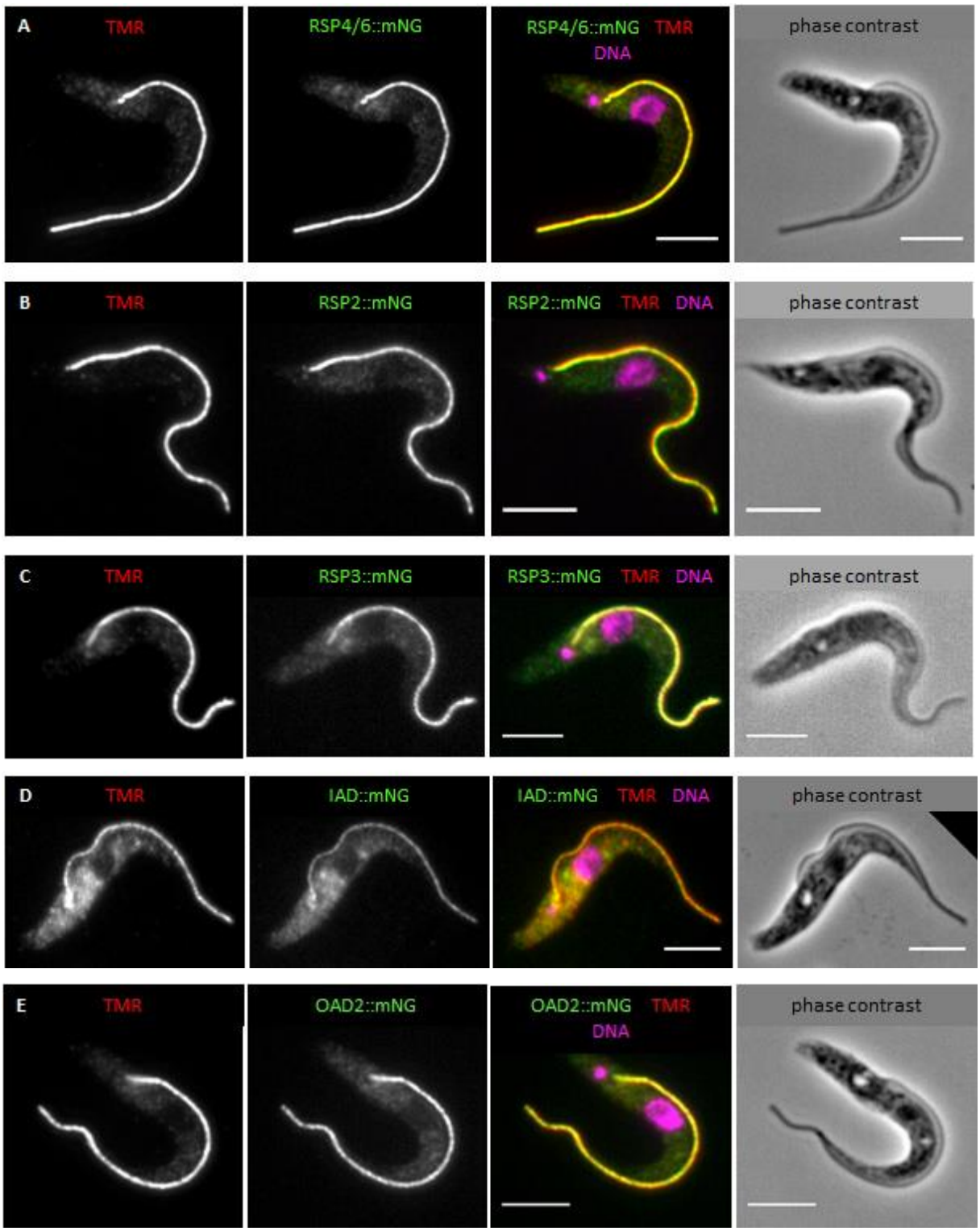

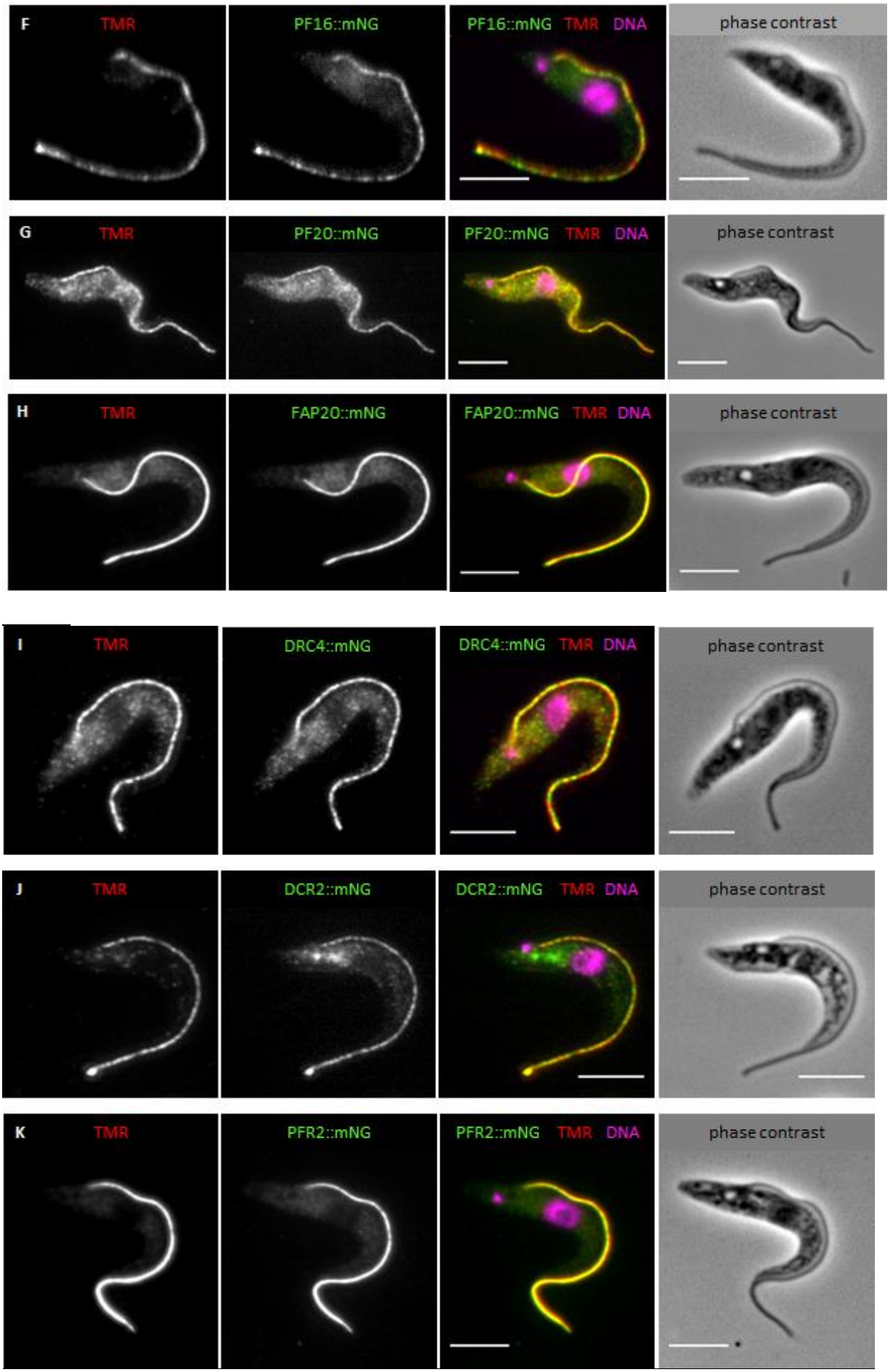
F
TMR
PF16::mNG
PF16::mNG TMR DNA
phase contrast
G
TMR
PF20::mNG
PF20::mNG TMR DNA
phase contrast
H
TMR
FAP20::mNG
FAP20::mNG TMR DNA
phase contrast
I
TMR
DRC4::mNG
DRC4::mNG TMR DNA
phase contrast
J
TMR
DCR2::mNG
DCR2::mNG TMR DNA
phase contrast
K
TMR
PFR2::mNG
PFR2::mNG TMR DNA
phase contrast

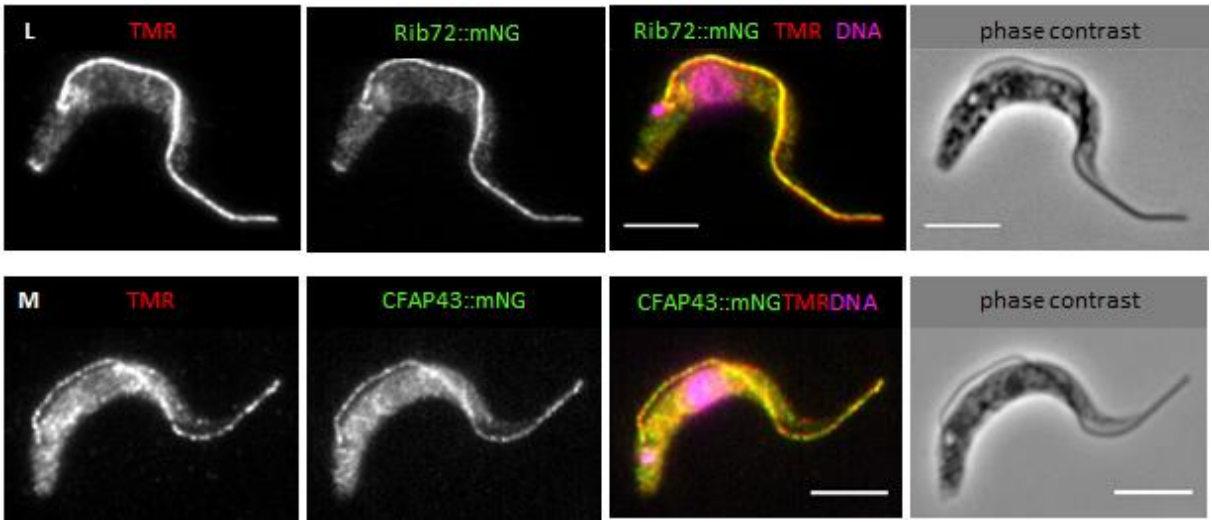

Figure 5.9. Visualisation of POI::mNG-HaloTag cell lines labelled with TMR ligand. mNG-HaloTag::POI cell lines were incubated with TMR ligand, washed, and immediately fixed on a glass slide **A-M**) Fluorescence images and cell phase contrast images. Scale bars represent 5 μm.

The intensities are not identical for each protein neither flagellar to cell body intensities (Fig 5.9.). This can be caused by variable expression of the individual proteins and subsequently by different cytosolic pool. Another explanation could be variable abundance of each protein in the flagellum.

In addition, cell lines expressing mNeonGreen-HaloTag tagged non-axonemal flagellar proteins, namely ACS1, which localises to the axonemal capping structure, and FCP4/TbKin15, which localises to the flagella connector (Varga *et al.*, 2017), were successfully prepared (Fig. 5.10.), but so far not fully validated and analysed.

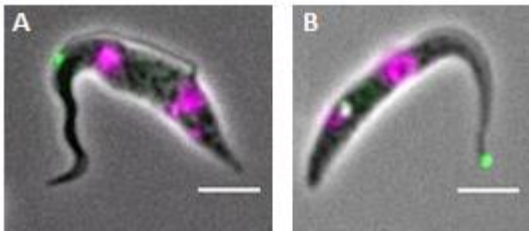

Figure 5.10. Cell lines expresing endogenously tagged POI::mNG-HaloTag. A) FCP4/TbKin15::mNG-HaloTag (green) expressing cell line is showing its localisation at he tip of new flagellum. **B**) ACS1::mNG-HaloTag (green) expressing cell line is showing localisation of ACS1 in the flagellar tip. **A**,**B**) DNA stained with DAPI (magenta). Scale bars represent 5 μm.

5.8 Tagged tubulin cannot be incorporated into the flagellum

Cell lines expressing α-tubulin endogenously tagged with either mNeonGreen-HaloTag or only HaloTag were prepared. It was possible to detect mNeonGreen signal in the cell body (Fig. 5.11.B). However, flagella were completely devoid of the signal, which was particularly apparent in the distal part of the flagellum overhanging the cell body (arrow in Fig. 5.11.). HaloTag tagged tubulin only behaved identical in these experiments.

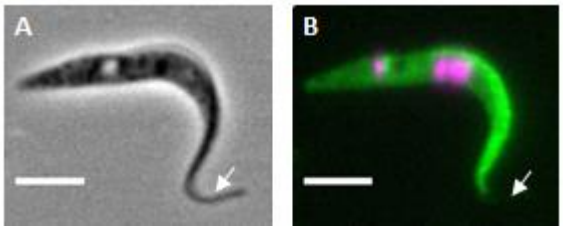

Figure 5.11. Cell line expresing endogenously tagged α-tubulin::mNG-HaloTag. Tagged α-tubulin is occuring only in cell body. Arrows indicate flagellum. **A**) Phase contrast. **B**) Fluorescence image of α-tubulin::mNG-HaloTag (green) expressing cell line, DNA stained by DAPI (magenta). Scale bars represent 5 μm.

This is consistent with previously published observations of tagged tubulin not entering the flagellum in *T. brucei* (Sheriff *et al.*, 2014). Hence, tubulin was not further studied in this work.

5.9 HaloTag tagging of protein enables their biotinylation

To further investigate the potential of the HaloTag technology, biotinylation experiments were performed. Biotin on the surface of an axoneme could be used, for example, to bind the axoneme in a defined way to surfaces of glass slides or beads with streptavidin or anti-biotin antibody. Two types of HaloTag ligands with attached biotin are available: HaloTag® Biotin Ligand and HaloTag® PEG-Biotin Ligand, which contains a polyethylene glycol spacer (Promega, 2019). Experimentally, binding of HaloTag® Ligands with biotin was tested using cell line with mNG-HaloTag tagged RSP4/6. It was not possible to biotinylate the axonemal proteins with neither ligand in living cells, indicating that the ligands may not enter the cell. Therefore, cells were first lysed with a detergent, and the cytoskeletal fraction was subsequently treated with the ligands. Biotinylation of cytoskeletons was validated using Streptavidin Cy5 Conjugate which can be visualised using a fluorescence microscope (Fig. 5.12.). A strong Cy5 signal was observed along flagellar cytoskeletons only in the case of HaloTag ligand-PEG-biotin, which overlapped with the signal of mNG. Hence, a protocol for efficient and specific biotinylation of axonemal proteins has been established.

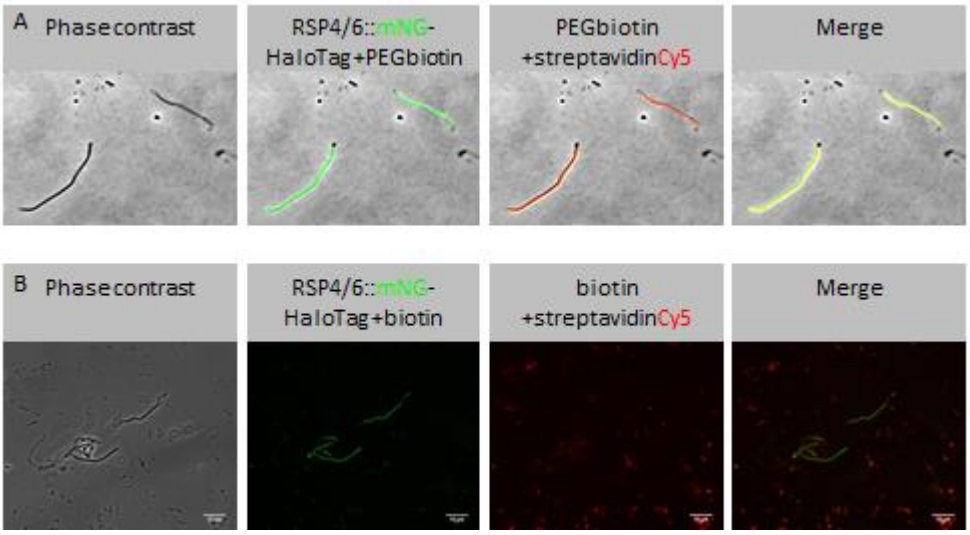

Figure 5.12. Biotinylation of HaloTag tagged axonemal proteins. A,B) Cytoskeletal flaction of cell line expresing RSP4/6::mNG-HaloTag (green) was treated with biotin binding to HaloTag, then washed out. Subsequently, biotinylated flagellar prep was incubated with Streptavidin Cy5 Conjugate (red). **A**) HaloTag® PEG-Biotin Ligand (PEGbiotin) bounds to HaloTag tagged protein. **B**) HaloTag® Biotin Ligand (biotin) does not bound to HaloTag tagged protein.

5.10 Incorporation of cytoskeletal proteins into the growing flagellum occurs exclusively at the distal end

Investigating the site of incorporation of proteins into the growing flagellum was done using dual mNeonGreen – HaloTag labelling approach. First, a protein present in the cell at a given time point was labelled with Coumarin HaloTag ligand. Although this fluorescent dye could not be visualised with presented microscope setup due to its low intensity, it blocks available HaloTag ligand binding sites. After washing the unbound ligand off (at t0), cells were allowed to grow for 2 hours. The protein incorporated into the flagellum since Coumarin washout was subsequently visualised by labelling with TMR HaloTag ligand (see Fig. 5.13.A for an outline of the experiment). There are three possibilities for the site of flagellar cytoskeleton construction (as well as combinations of them): it can be built from the distal end (Fig. 5.13.B); material can be incorporated along the flagellum (Fig. 5.13.C); or it can be built from the proximal end (Fig. 5.13.D). Possible outcomes of presented dual labelling experiment in regard to the possible modes of the flagellum construction are depicted in Fig. 5.13.

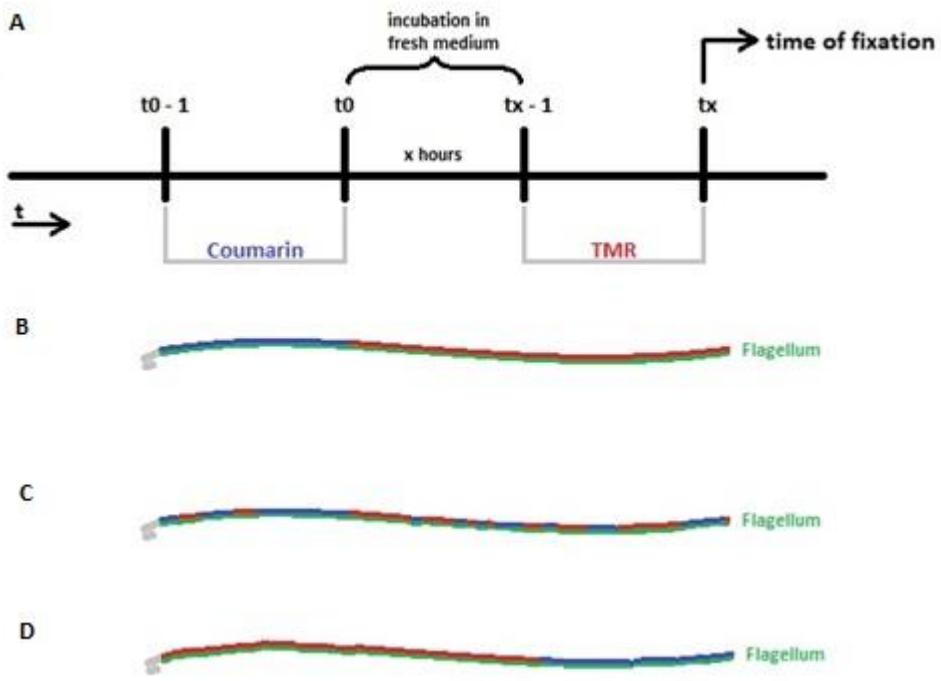

Figure 5.13. Dual labelling experiment. A) A schematic representation of sequenced labelling by Coumarin ligand and TMR ligand, which are binding to HaloTag tagged proteins in the flagellum. In the beginning, a cell was incubated with Coumarin ligand at time = t0 minus one hour. After the incubation and the wash (t0), cell grew in a fresh medium for X hours. Next, at time = tX minus one hour cell was treated by TMR ligand. **B-D**) three possible outcomes of the experiment: **B**) incorporation of material from the distal end, **C**) incorporation of new material along, **D**) incorporation of material from the proximal end. **A**) tX = time of fixation, **B-D**) flagellum with particular protein tagged by mNG (green), labelled by Coumarin (blue), and TMR (red).

The dual labelling experiment using Coumarin and TMR ligands was performed with RSP4/6 mNG-Halo tagged cell line. Out of 11 single flagellum cells in G1 phase (1F1K1N) 8 were devoid of the TMR signal, and in 3 cells flagella were labelled exclusively at their distal ends. In all 23 cells with two flagella, the TMR signal was identified exclusively at the distal end of their new flagellum (Fig. 5.14.).

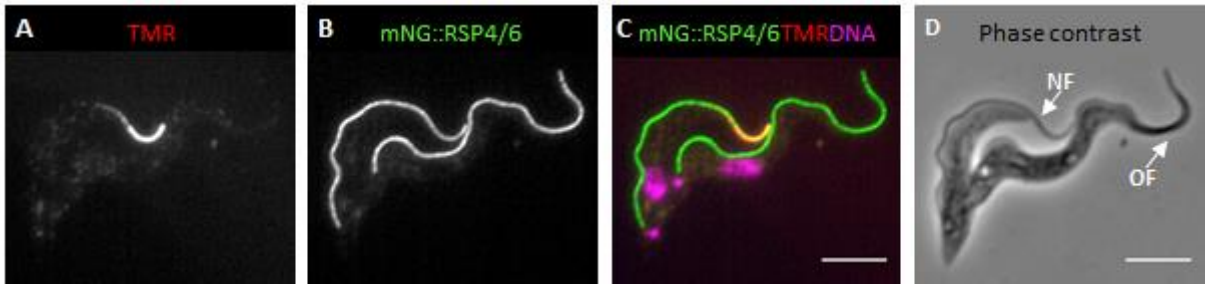

Figure 5.14. Site of incorporation of RSP4/6 protein into the new growing flagellum. RSP4/6::mNG-HaloTag cell line culture was incubated with Coumarin ligand, then washed and incubated with TMR ligand for two hours. **A-D**) A cell in 2F2K2N stage of the cell cycle. NF = new flagellum, OF = old flagellum. **E-H**) *T. brucei* cell in 2F1K1N (left). Scale bars represent 5µm.

In the case of RSP2 protein, seven hours after Coumarin ligand labelling, free HaloTag tagged proteins were marked by TMR ligand. Construction of the new/daughter flagellum within divided 2F2K2N cell can be seen in Fig. 5.15. Daughter flagellum is cumulatively labelled with TMR ligand; this indicates that the cells started to divide just after the Coumarin labelling.

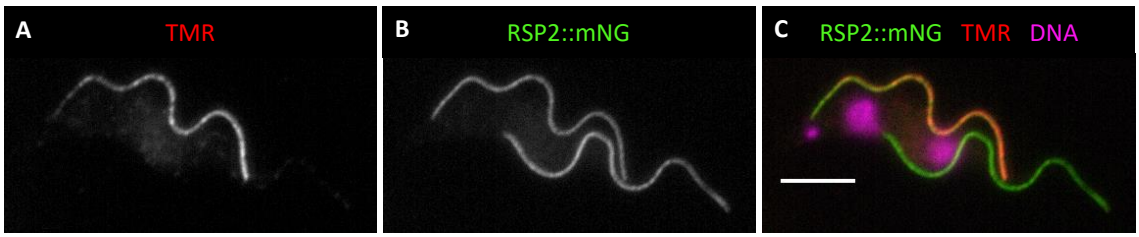

Figure 5.15. Site of incorporation of RSP2 protein into the new growing flagellum. **A-C**) *T. brucei* cells in 2F2K2N stadium. RSP2::mNG-HaloTag cell line culture was incubated with Coumarin ligand, then washed and set for 7 hrs; one hour before fixation cells were incubated with TMR ligand. Scale bars represent 5 µm.

To further examine the incorporation of protein constituents of various flagellum cytoskeleton structures, a TMR labelling experiment was done with 14 cell lines. The experimental set up differed from the Coumarin TMR double labelling experiment. Here, cells were initially incubated for 1 hour with TMR thereby labelling all Halo-tagged protein present at that point in the cell. Excess of TMR was washed out from the cells. Cells were incubated in fresh medium for 4 hours (or 2 hours in the case of PFR2) and examined. The protein synthesised since the washout and added to the flagellar cytoskeleton lately should be devoid of the TMR fluorescence signal.

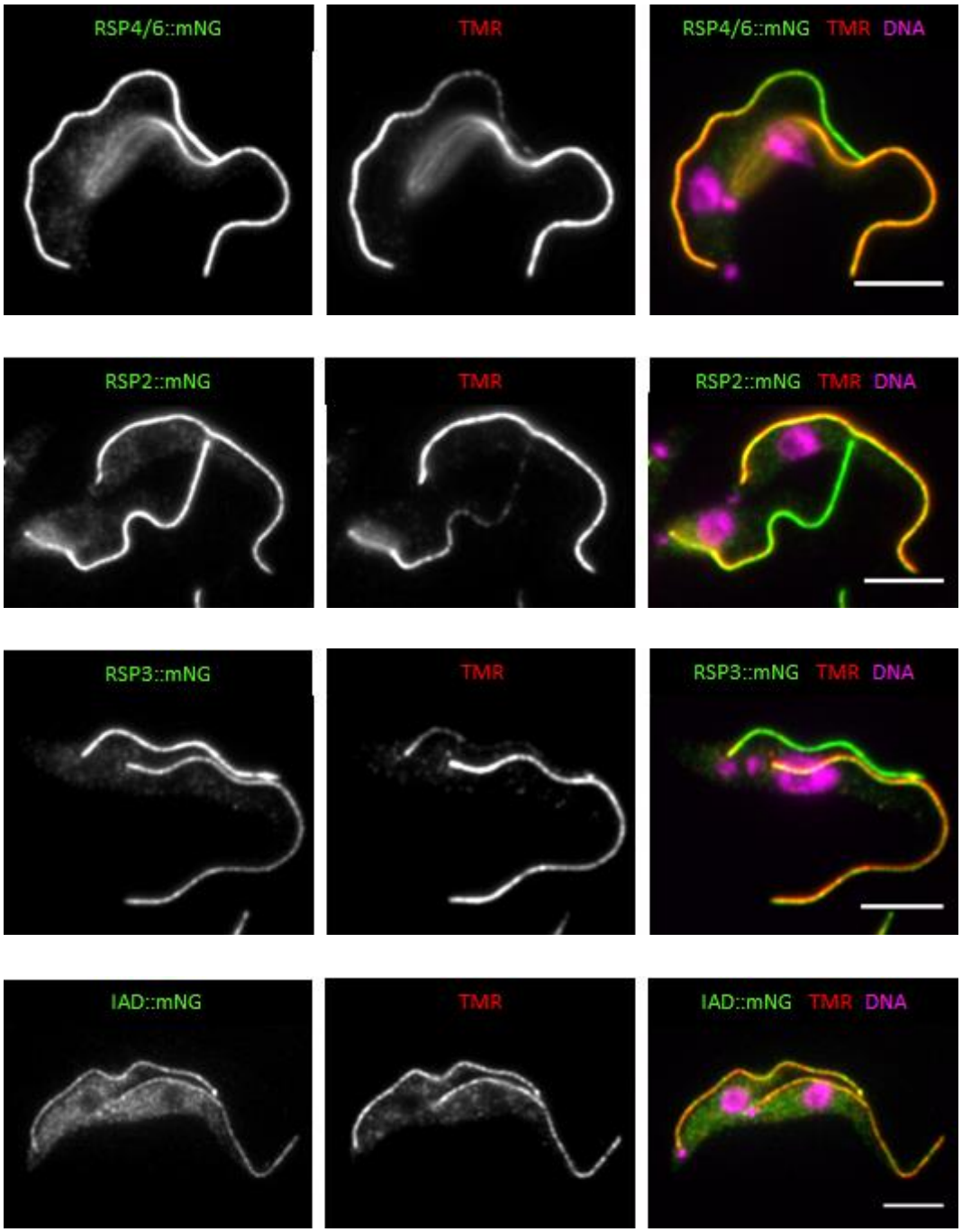

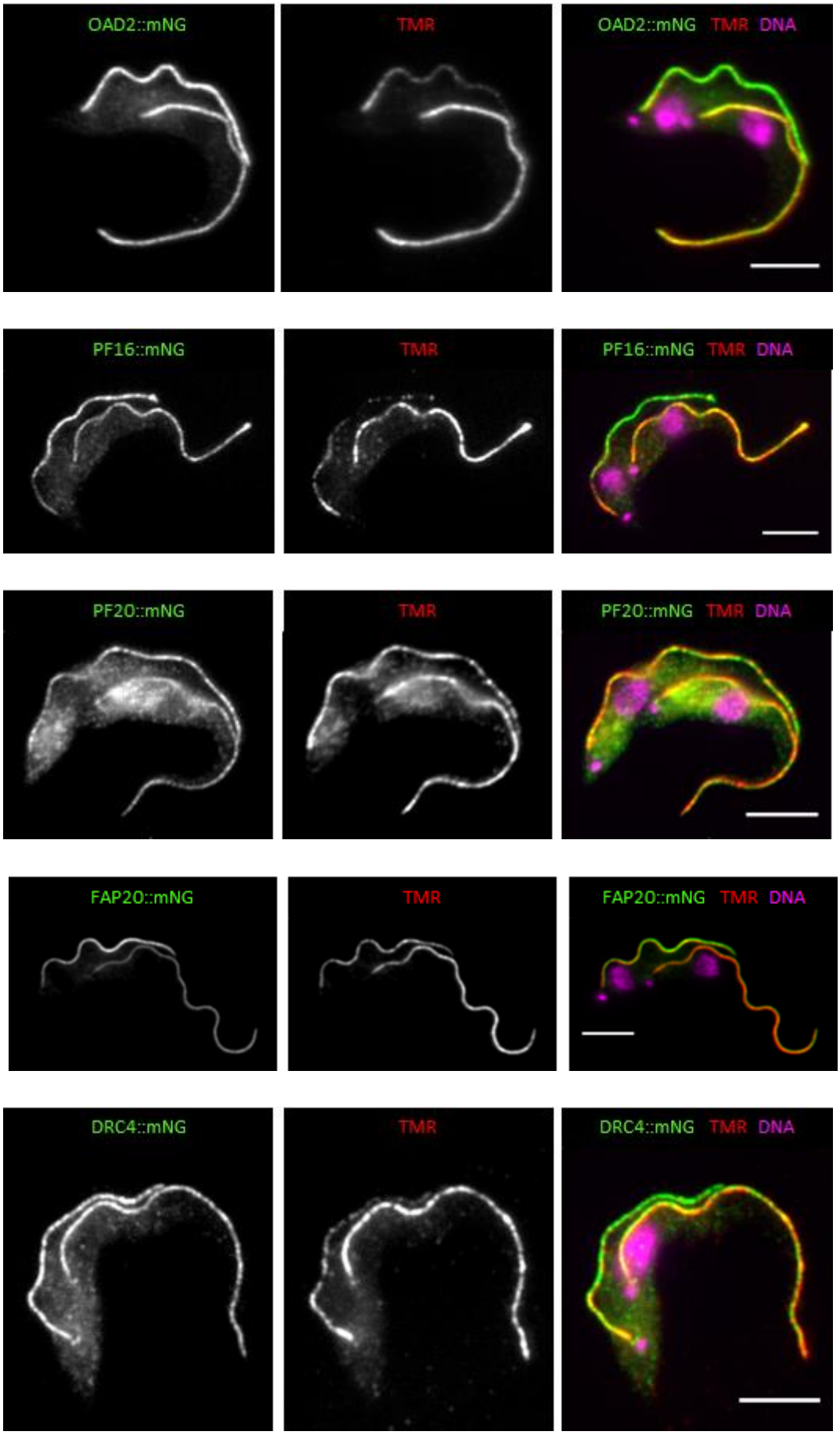
OAD2::mNG
TMR
OAD2::mNG TMR DNA
PF16::mNG
TMR
PF16::mNG TMR DNA
PF20::mNG
TMR
PF20::mNG TMR DNA
FAP20::mNG
TMR
FAP20::mNG TMR DNA
DRC4::mNG
TMR
DRC4::mNG TMR DNA

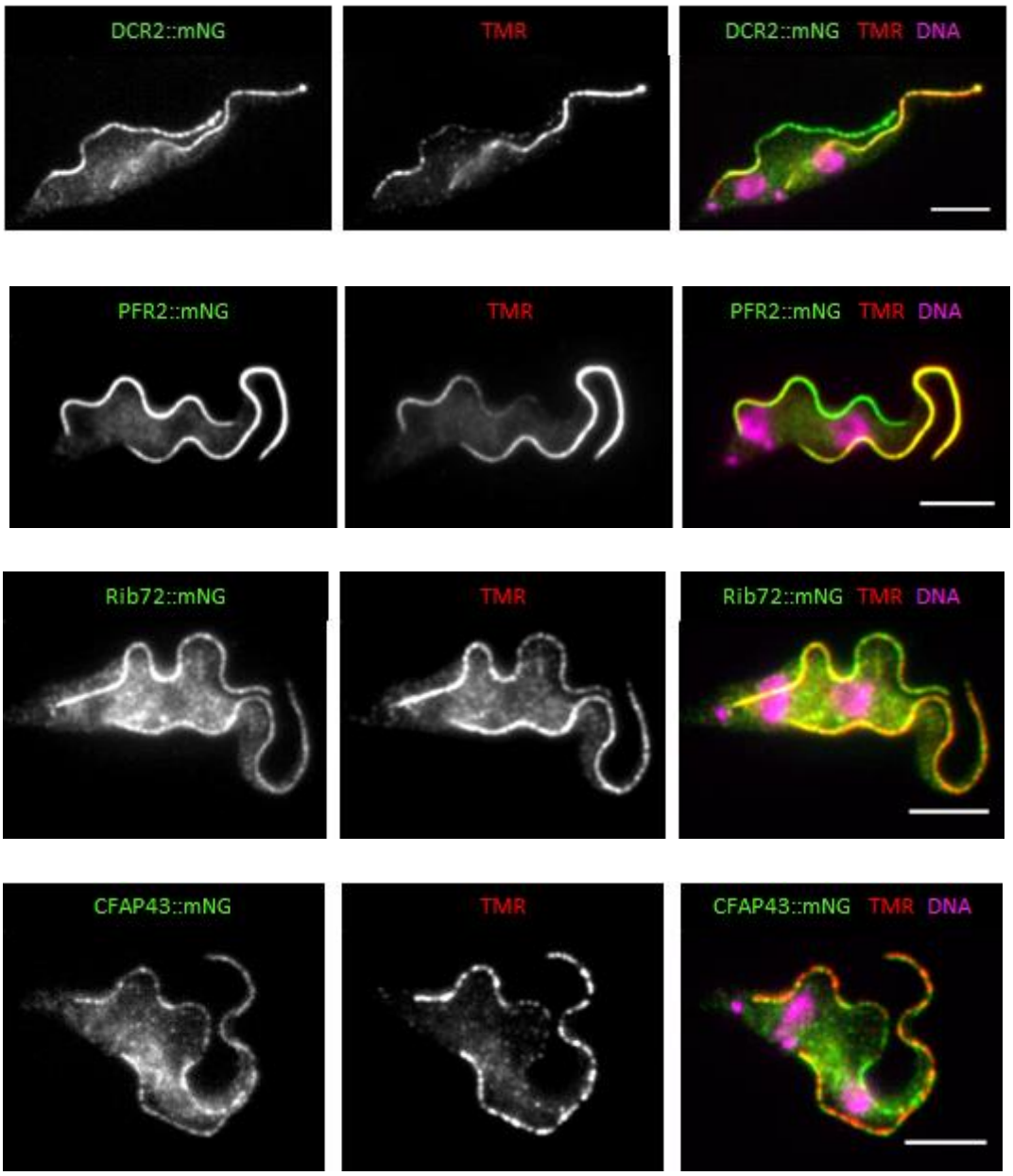

Figure 5.16. Incorporation constituents of various cytoskeletal complexes into the flagellum. POI::mNG-HaloTag cell lines were labelled with TMR ligand, then washed and examined 4 hours later. Scale bars represent 5 μm.

In the distal end, only mode of incorporation of cytoskeletal proteins into the new flagellum was detected in 76 out of 77 examined cells (Table 5.5.). In the remaining case it was not possible to recognise mode of incorporation.

Table 5.5. List of POIs and number of cells examined (n) for each cell line. In the case of PF20 5 of 6 cells show the distal end only incorporation.

POI	RSP4/6	RSP2	RSP3	IAD	OAD2	PF16	PF20	FAP20	DRC4	DCR2	PFR2	Rib72	CFAP43
n	9	6	4	5	9	10	5/6	4	3	8	6	4	3

5.11 Analysis of fluorescence intensity

To analyse the fluorescence intensity profile automatically, a custom-made R script, written and developed by Luděk Štěpánek Ph.D., from the Laboratory of Cell Motility at IMG, was used. First, background-corrected intensity profiles of TMR and mNeonGreen were normalised to the range of 0 - 1 to allow for comparison of their relative intensities. The mNeonGreen signal would remain relatively constant along the entire flagellum length, with a sharp decay at the distal end. In contrast, at later time points post TMR labelling the TMR signal often starts to decay closer to the proximal part of the flagellum, which results in the higher relative abundance of the green signal in the distal part. The point where the red signal intensity starts to steadily decrease below the normalised intensity of the green signal until it reaches near-zero values at the distal tip is referred to as the "**decay point**" hereafter. To decide whether the red and green intensity profiles differ significantly in each given flagellum, the difference between green and red values was summed up for all points between the decay point and the distal end of the flagellum. If the total difference was not greater than 2.5 arbitrary intensity units (A.U.), there was no alteration of the TMR compared to mNeonGreen labelling. This category of cells was designated as "fully labelled". The cells with a green and red signal difference greater than 2.5 A.U. were further characterised based on the length and slope of the red signal decay. **The decay length** was simply calculated as the distance of the decay point from the distal end of the flagellum (determined as the decay point of the mNeonGreen signal). The decay slope was quantified by fitting the asymptotic regression function to the decaying TMR signal. The logarithm of the exponential coefficient of this function used to characterise the decay slope, with values close to 0 indicating steep drop ("drop" hereafter) and values closer to -10 indicating gradual decrease ("gradient" hereafter). To simplify evaluation and discussion of the results, arbitrary thresholds were chosen for the decay length and slope: "short" and "long " are profiles with decay length shorter or longer than 7 µm, respectively, and "drop" and "gradient" are designated profiles with alpha exponent value above or below -3, respectively. Based on these criteria, all cell were sorted into five categories: fully labelled, short drop, short gradient, long drop, long gradient. In several cases, the regression function could not be fitted reliably due to the noise in the data, resulting in categorising the cell as "not determined". In addition, a region distal to the decay point, in which the cumulative intensity of TMR, when measured from the distal end, reached 0.05 of the maximum TMR intensity, was determined as devoid of the red signal.

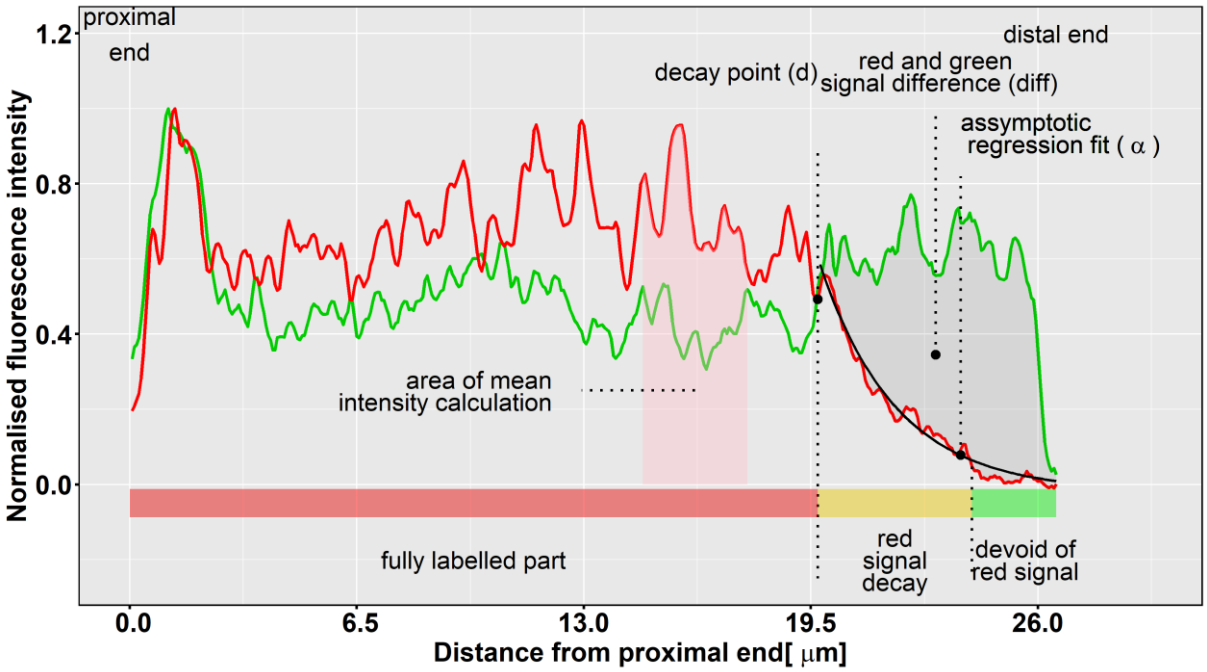

Figure 5.17. An explanation of intensity profile of Signal decay analysis.
Analysed flagellum is schematically delineated in the bottom, the proximal (left) to distal end (right). Green curve and red curve correspond to normalised fluorescent signal of mNeonGreen and TMR, respectivelly. Decay point (d) is showed where the red signal intensity starts to diverge from green signal intensity. The area where the difference between total red and green signal is above 2.5 A. U. is shown (diff) Red signal curve decay is fitted by assymptotic regression function (α) (black line).

For this analysis, only 'mature' flagella were used; these are single flagella of 1F cells and old flagella of 2F cells.

5.12 A categorisation of fluorescence intensity signal decay pattern

Based on the fluorescence intensity profile analysis five categories of red signal (TMR) decay on the flagellar distal end were determined: fully labelled (Fig. 5.18.), short gradient (Fig. 5.19.), long gradient (Fig. 5.20.), short drop (Fig. 5.21.), and long drop (Fig. 5.22.) category. These categories were observed across all cell lines and all time points. However, their proportions dramatically changed in time (see below).

Fully labelled:

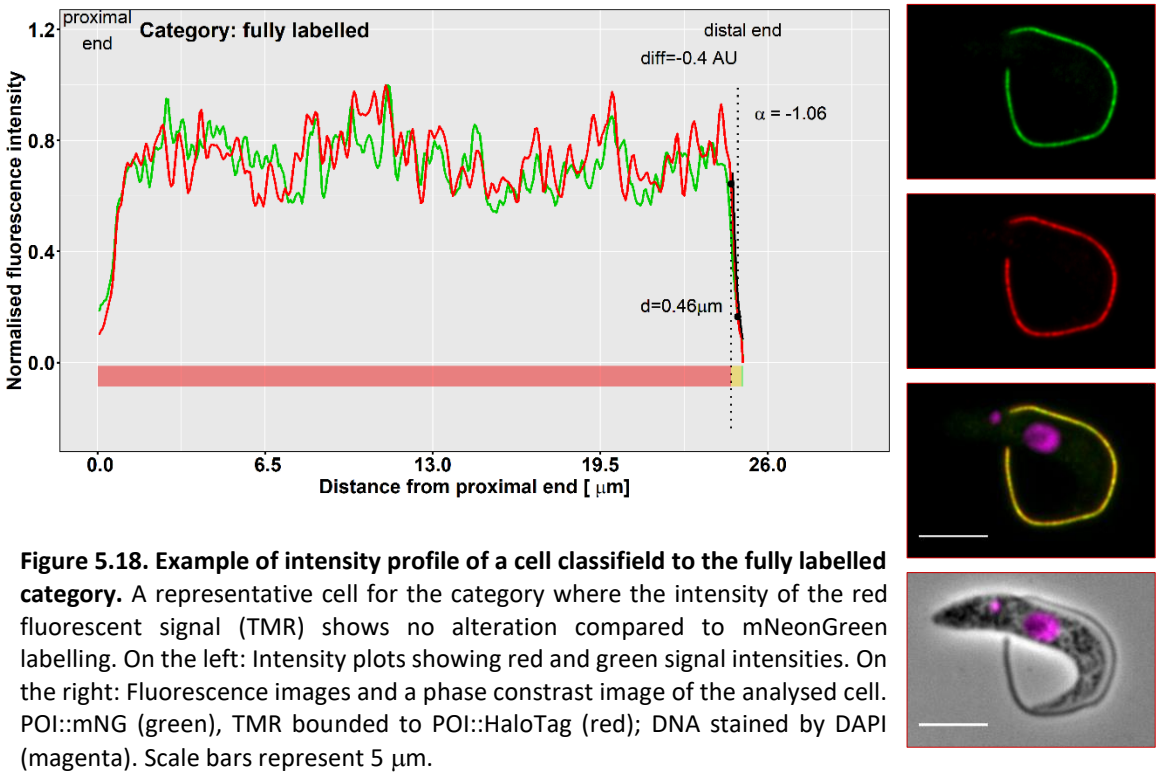

Figure 5.18. Example of intensity profile of a cell classifield to the fully labelled category. A representative cell for the category where the intensity of the red fluorescent signal (TMR) shows no alteration compared to mNeonGreen labelling. On the left: Intensity plots showing red and green signal intensities. On the right: Fluorescence images and a phase constrast image of the analysed cell. POI::mNG (green), TMR bounded to POI::HaloTag (red); DNA stained by DAPI (magenta). Scale bars represent 5 μm.

Short gradient:

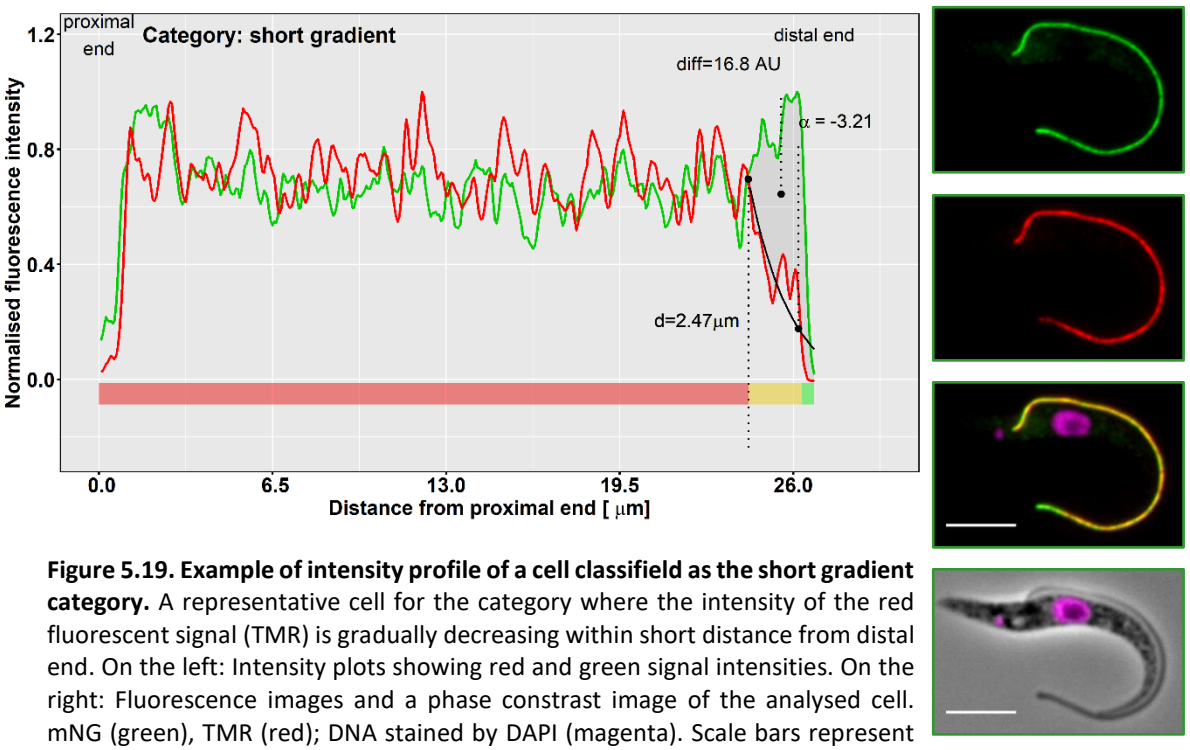

Figure 5.19. Example of intensity profile of a cell classifield as the short gradient category. A representative cell for the category where the intensity of the red fluorescent signal (TMR) is gradually decreasing within short distance from distal end. On the left: Intensity plots showing red and green signal intensities. On the right: Fluorescence images and a phase constrast image of the analysed cell. mNG (green), TMR (red); DNA stained by DAPI (magenta). Scale bars represent 5 μm.

Long gradient:

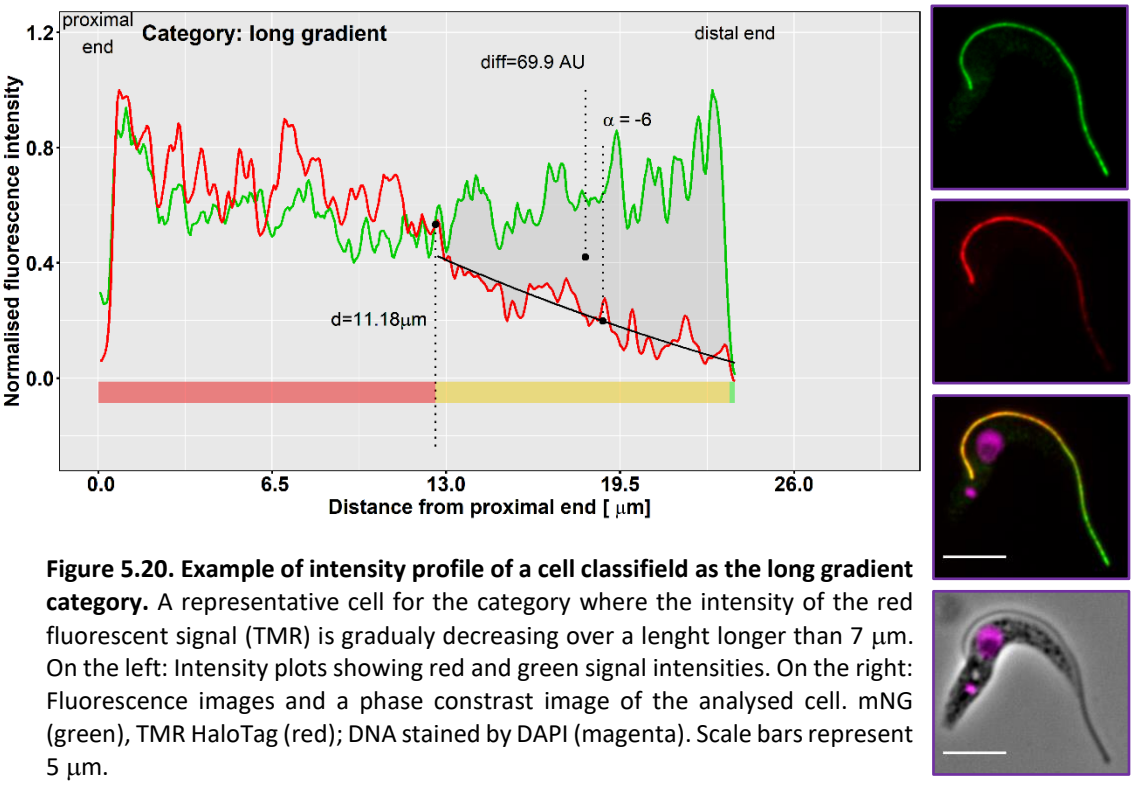

Figure 5.20. Example of intensity profile of a cell classifield as the long gradient category. A representative cell for the category where the intensity of the red fluorescent signal (TMR) is gradualy decreasing over a lenght longer than 7 μm. On the left: Intensity plots showing red and green signal intensities. On the right: Fluorescence images and a phase constrast image of the analysed cell. mNG (green), TMR HaloTag (red); DNA stained by DAPI (magenta). Scale bars represent 5 μm.

Short drop:

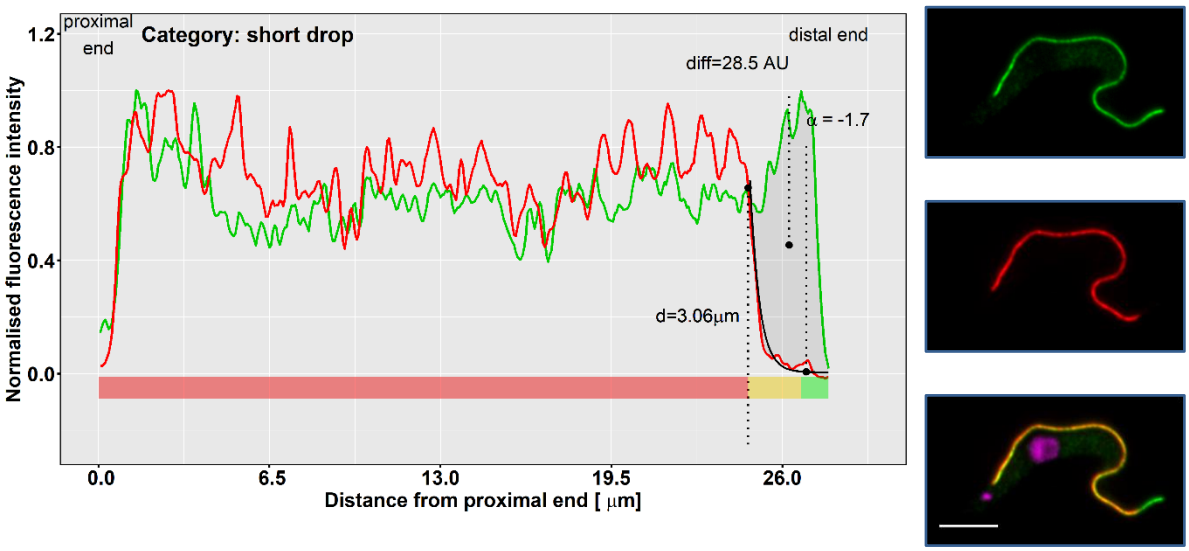

Figure 5.21. Example of intensity profile of a cell classifield to the short drop category. A representative cell for the category where the intensity of the red fluorescent signal (TMR) is sharply decreasing over short distance. On the left: Intensity plots showing red and green signal intensities. On the right: Fluorescence images and a phase constrast image of the analysed cell. mNG (green), TMR (red); DNA stained by DAPI (magenta). Scale bars represent 5 μm.

Long drop:

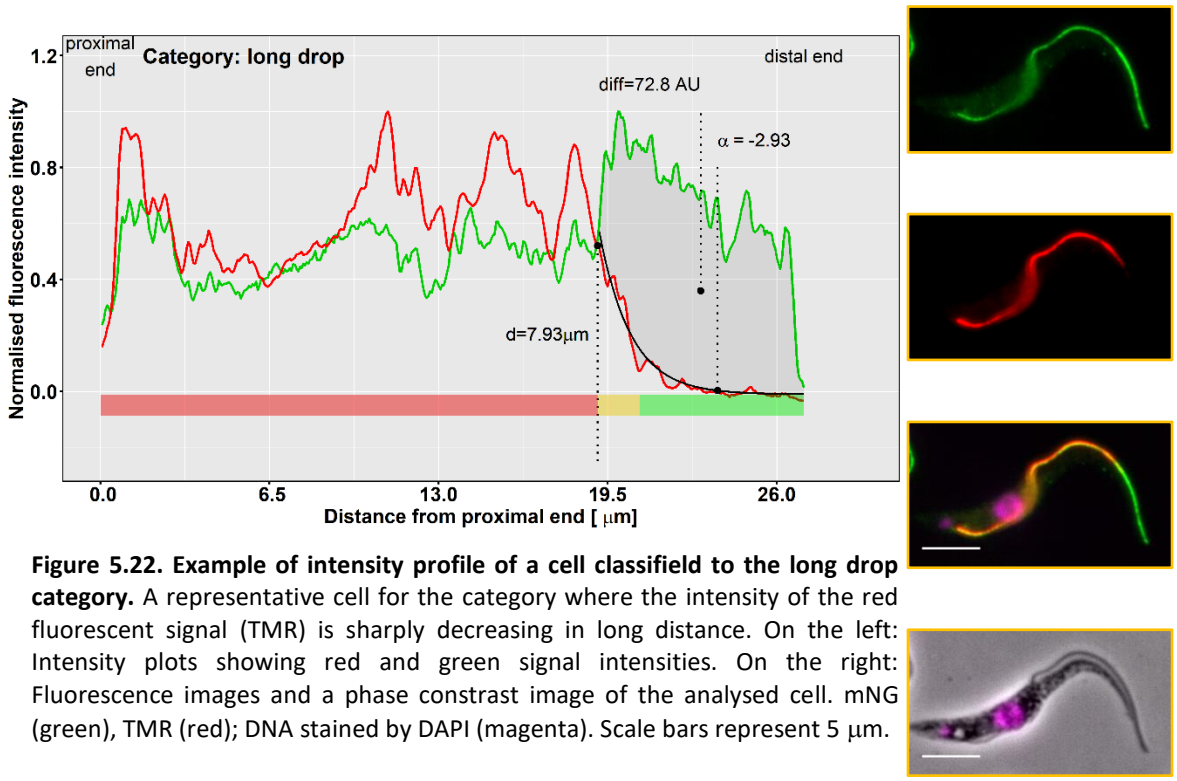

Figure 5.22. Example of intensity profile of a cell classifield to the long drop category. A representative cell for the category where the intensity of the red fluorescent signal (TMR) is sharply decreasing in long distance. On the left: Intensity plots showing red and green signal intensities. On the right: Fluorescence images and a phase constrast image of the analysed cell. mNG (green), TMR (red); DNA stained by DAPI (magenta). Scale bars represent 5 μm.

5.13 Distribution of categories for all analysed flagella

Together 1,798 cells were analysed across 10 cell lines and 6 time points. Distribution of all analysed cells into categories is shown in Fig. 5.23., where the majority of cells belong to the short drop category (N = 629), followed by short gradient (N = 303), long gradient (N = 296), and fully labelled (N = 479). Intriguingly, only a very limited number of cells (N = 7) were observed belonging to in the long drop category. Finally, some of the cells (N = 84) could not be determined based on the selected criteria.

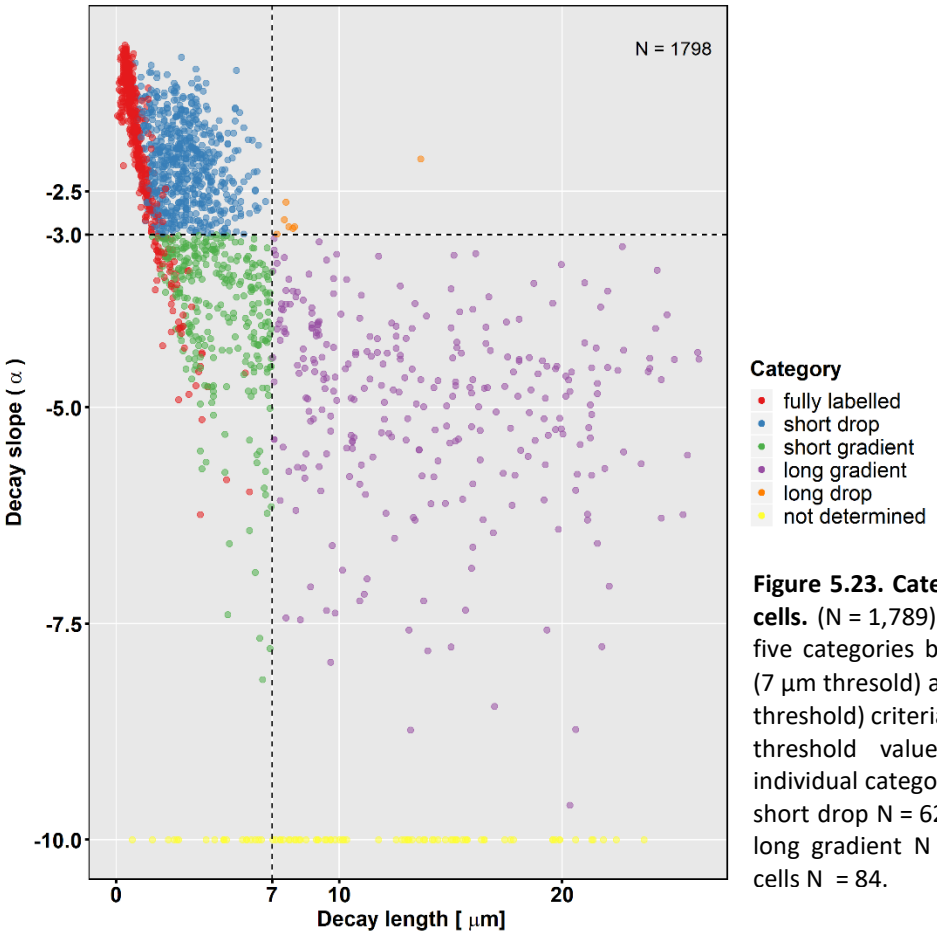

Figure 5.23. Categorisation of all analyzed cells. (N = 1,789). Cells were classified into five categories based on the decay length (7 μm thresold) and the decay slope (α = -3 threshold) criteria. Dotted lines indicate the threshold values. Number of cells in individual categories: fully labelled N = 479; short drop N = 629, short gradient N = 303, long gradient N = 7 cells. Not determined cells N = 84.

Representation of each category in different time points can be seen in Fig. 5.24.

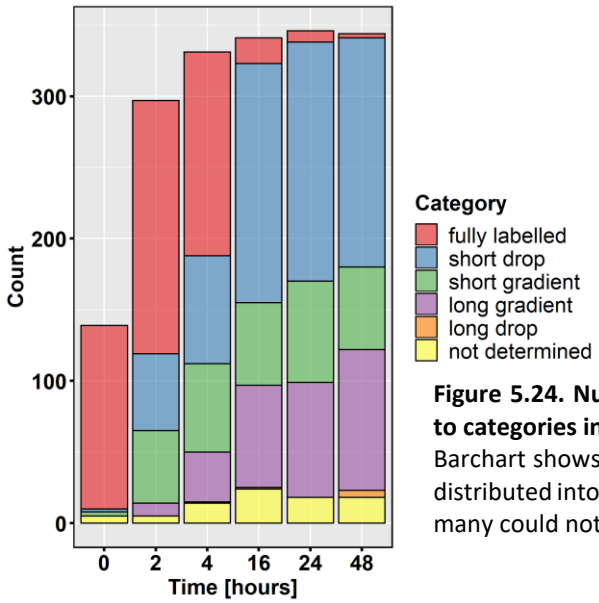

Figure 5.24. Number of all flagella sorted to categories in each time point (hours). Barchart shows how many of flagella were distributed into the five categories and how many could not be determined.

Although differences between individual cell lines do exist (see below) these aggregated data show that in general cells at t0 have their flagella fully labelled with TMR, as expected. 2 hours post labelling significant amounts of short drop category and the short gradient category are present and their amounts are similar, while long gradient category flagella are rate. At later time points, the fully labelled flagella are progressively reduced, becoming very rare at 48 hours. Concomitantly, amounts of short drop and long gradient category flagella increase.

5.13.1 Distribution of categories for individual cell lines

Together, 10 cell lines were analysed, and amounts of flagella in individual categories in time for each cell line are shown in Fig 5.25. Although there is some variability in patterns of cell distribution over time between individual cell line, for a majority of them the pattern is similar to the aggregated analysis (see above), as expected.

Major deviations from the generic pattern were seen in cell lines expressing tagged IAD and Rib72. In these cell lines, the distribution pattern remained constant during initial 4 hours of the experiment, thereafter resembling the generic pattern. In the FAP20 tagged cell line, unusually high amounts of cells that could not be classified (not determined) was observed. Finally, the cell lines with tagged FAP20, OAD2 and PFR2 showed the highest amounts of cells of the short gradient category at early time points (2 - 4 hours post labelling).

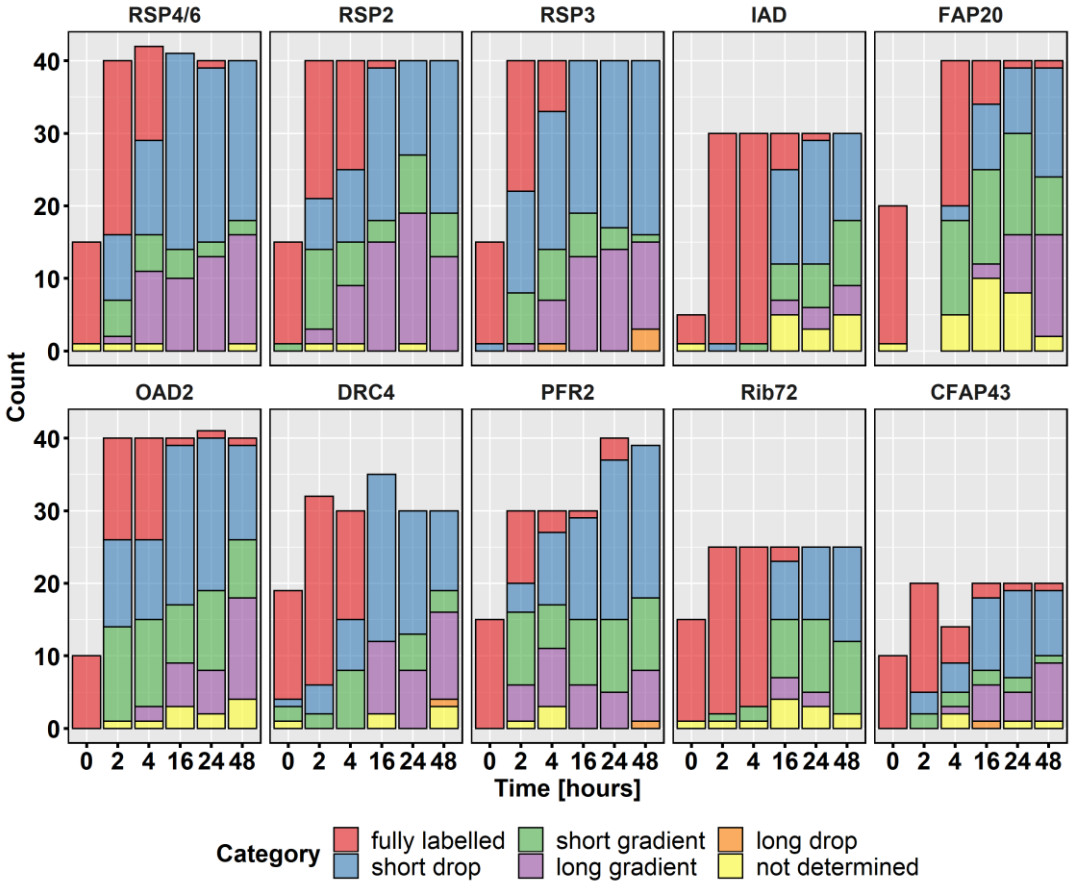

Figure 5.25. Categories represented in every cell line. Y-axis shows numbers of analysed cells. Y-axis shows time in hours.

Interestingly, in FAP20 cell line, the mNG-signal intensity plots differed from those of other tagged proteins. For example, an increase in the mNG signal towards the distal end was often observed.

In Fig. 5.26., two commonly observed phenotypes are shown. First, in a number of the cell TMR signal is constant along the whole flagellum. However, mNG fluorescent signal is slightly increased from the base to the tip (Fig. 5.26.A). Second, the cell where the distal part of the flagellum shows an interruption in mNG fluorescence signal followed by an increase of it at the very end of the flagellum (Fig. 5.26.B).

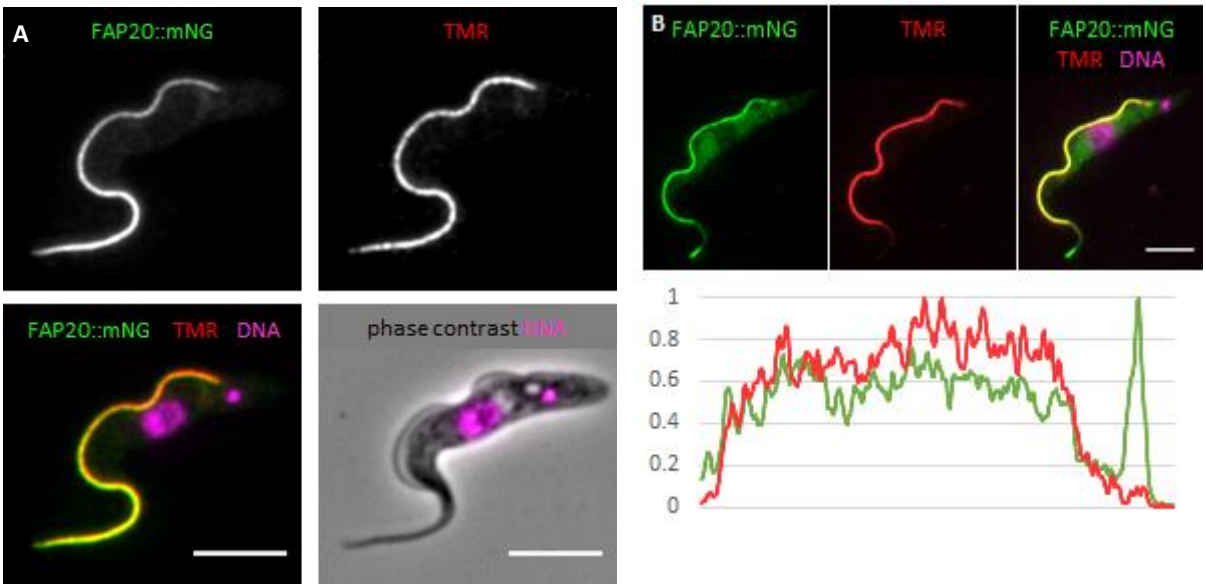

Figure 5.26. Cell line expresing endogenously tagged FAP20::mNG-HaloTag.
A) Colocalisation of TMR (red) labelled protein and mNG (green) tagged protein in time point 4 hours **B**) FAP20::mNG-Halo protein distribution in the flagellum in 48 hours past TMR labelling; normalised intensity profile (A.U.) of FAP20::mNG-Halo (green) and TMR (red) fluorescence signal is shown from base to the tip. **A,B**) DNA stained by DAPI (magenta). Scale bars represent 5 μm.

In the above-described experiment, only the mature flagella with some detectable TMR signal were considered. To assess how did proportions of flagella in individual categories change in time in a cell population mature flagella completely unlabelled, were also included in the analysis. Hence, for the cell line with tagged RSP4/6, all mature flagella were categorised at each time point (Fig 5.27 and Table 5.6.). This allowed determining a precise representation of each category across the duration of the experiment, which is depicted in Fig. 5.27.

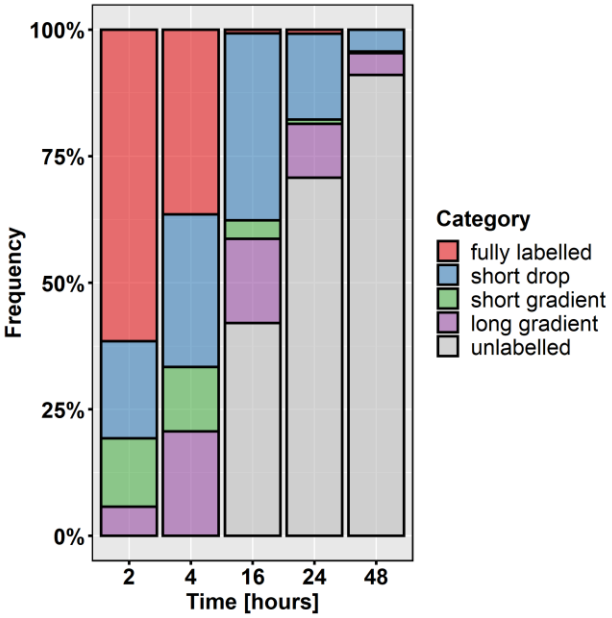

Table 5.6. Frequencies of cells in each category for the tagged RSP4/6 cell line

time point (hours)	2	4	16	24	48
number of total cells (flagella) analysed	52	63	138	253	257
fully labelled (%)	61.5	36.5	0.72	0.79	0
short drop (%)	19.2	30.2	37	17	4.28
short gradient (%)	13.5	12.7	3.62	0.79	0.39
long gradient (%)	5.77	20.6	16.7	10.7	4.28
unlabelled (%)	0	0	42	70.8	91.1

Figure 5.27. Frequencies of individual TMR signal categories in the RSP4/6 tagged cell line in the course of the experiment. X-axis shows time (hours), Y-axis shows frequency of individual categories. For data see Table 5.6.

It is apparent that the unlabelled mature flagella first appear in the cell population at some point between 4 and 16 hours post labelling. Their proportion in the population increases such that at 48 hours post labelling they constitute over 90% of the population.

It was attempted to predict the frequency of fully labelled mature flagella in a cell population at various time points post TMR labelling (Table 5.7.) based on an experimentally determined growth rate of the RSP4/6 tagged cell line in the course of the time-course experiment (Fig 5.28.).

Table 5.7. Frequencies of expected fully labelled mature flagella ocuring in the culture in different time points

time point (hours)	2	4	16	24	48
% of expected mature flagella	97.8	82.5	36.7	19.8	5.61
observed frequencies of labelled flagella					
fully labelled (%)	61.5	36.5	0.72	0.79	0
short drop (%)	19.2	30.2	37	17	4.28
short gradient (%)	13.5	12.7	3.62	0.79	0.39
long gradient (%)	5.77	20.6	16.7	10.7	4.28
unlabelled (%)	0	0	42	70.8	91.1

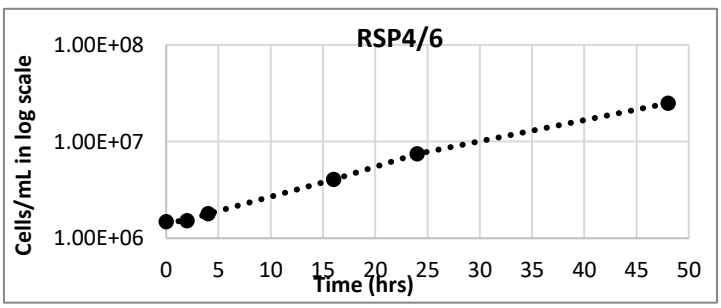

Figure 5.28. Growth curve for RSP4/6 cell line. Cell density was measured in each time point (in quadricats). Cell densities are plotted for every time point separately.

Assuming that all flagella of 1F cells and the old flagella of 2F cells stay do not change over time (stay fully labelled); 97.8% of mature flagella are expected to be fully labelled at 2 hours, with the remaining 2.2% corresponding to flagella of new flagellum daughter cells of a recent cytokinesis event. However, in the experiment, the proportion of the fully labelled flagella was lower (61.5%), with the remaining flagella classified as a short drop (19.2%), short gradient (13.5%) and long gradient (5.77%) category. Similarly, the fully labelled flagella were significantly underrepresented at all subsequent time points, and virtually lacking at 48 hours. This data indicates that there is a change to the TMR signal of mature flagella, which thereby fall into a different signal intensity category.

5.14 Comparison of average flagellar length in all categories and decay in short drop category for cell line RSP4/6

Proportions of flagella in the long gradient category at various time points is consistent with expected proportions of new-flagellum daughters. This resulted from cytokinesis events occurring since the TMR labelling. Protein molecules unlabelled with TMR are expected to be incorporated into the distal part of the flagellum. This happens for the time period from the removal of TMR ligand to cytokinesis, and possibly for a short amount of time thereafter, during which the new flagellum reaches its full length (Abeywickrema *et al.*, 2019).

On the other hand, the unexpectedly low amounts of fully labelled flagella are reflected by an unexpected appearance of flagella of the short drop and short gradient categories. Indeed, when all three categories summed up, numbers close to the expected frequencies of fully labelled flagella (at 2 hours 94.2 % versus 97.8% expected; at 4 hours 79.4% versus 82.5% etc.). This indicates that the fully labelled flagella transit to the short drop and short gradient categories.

This transition could happen by the turnover of the protein at the distal end of the flagellum, which could occur either by an exchange of protein molecules within an existing axoneme or by a shortening of the axoneme followed by its elongation. Alternatively, the transition could happen only by elongation of an existing mature axoneme. To distinguish between turnover and growth, total lengths of the studied mature flagella in time were plotted (Fig. 5.29.). The flagella length was approximately constant within the first 4 hours after TMR incubation, showing that the presence of the short drop and short gradient categories was not due to an axonemal elongation, but rather due to turnover in the distal end region. The median decay length (distance between the decay point and the distal end) was 1.43 µm in cells of the short drop category at 2 hours post TMR labelling, indicating the axonemal length subject to turnover (Fig. 5.30.).

Interestingly, a slight increase in the median flagellar length was observed at the later time points (for example flagella at 16 hours were on average 1.82 µm longer than the flagella at 0 hours) (see Fig. 5.29.).

Curious, a corresponding increase in the median length of the distance between the decay point of the TMR signal and the distal end of the flagellum was observed over time (Fig. 5.30). Similar observations were done when analysing aggregated data of all studied cell lines (Fig. 5.31, Fig. 5.32.).

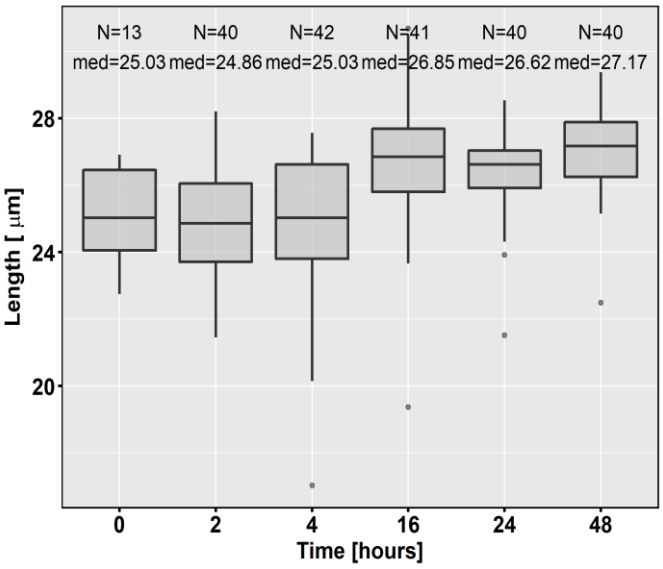

Figure 5.29. Median flagella lengths in the RSP4/6 tagged cell line.
Lenghts of flagella at each time point were measured and are plotted as median (inside the box). Upper and lower hinges are 75th and 25th percentiles. The whiskers extend up to values that lie inside 1.5X inter-quartile range from each hinge. Outlying values are plotted separately. Note that the Y-axis starts at 16 µm.

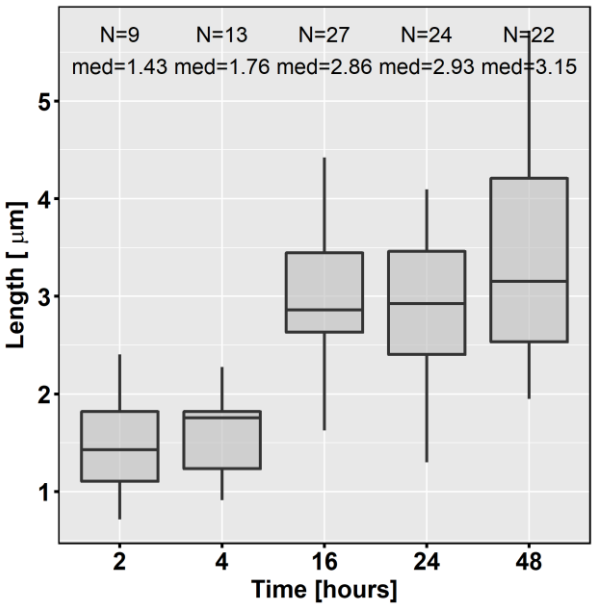

Figure 5.30. Distance between the decay point and the distal end of the flagellum in short drop category of RSP4/6 tagged cell line.
Lenghts are plotted as median (inside the box). Upper and lower hinges are 75th and 25th percentiles. The whiskers extend up to values that lie inside 1.5X inter-quartile range from each hinge. Outlying values are plotted separately.

Flagellar lengths were essentially constant in first 4 hours and increased after that (Fig 5.31.), which was mirrored by an increase in the distance between the decay point and the distal end of the flagellum (Fig 5.32.).

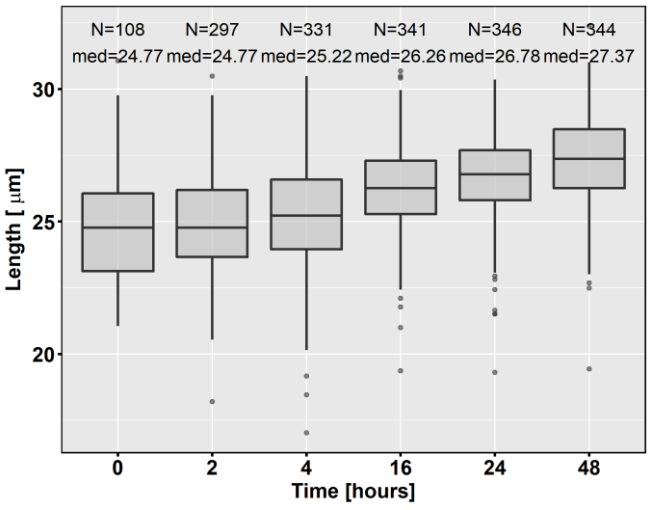

Figure 5.31. Median flagella length for all cell lines.
Lenghts of flagella at each time point were measured and are plotted as median (inside the box). Upper and lower hinges are 75th and 25th percentiles. The whiskers extend up to values that lie inside 1.5X inter-quartile range from each hinge. Outlying values are plotted separately. Note that the Y-axis starts at 15 µm.

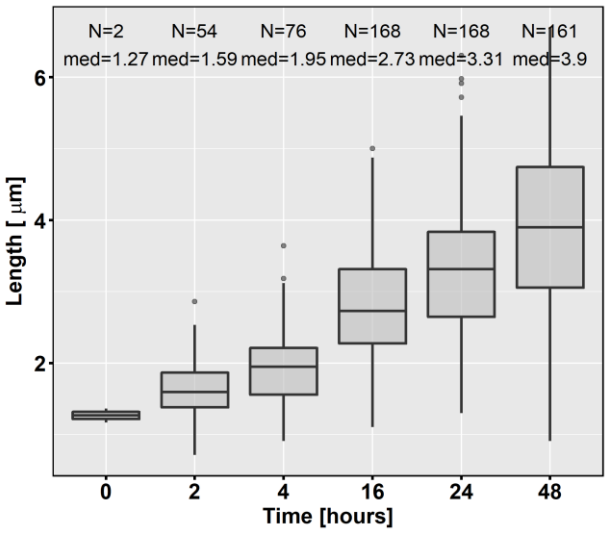

Figure 5.32. Distance between the decay point and the distal end of the flagellum in short drop category of all tagged cell lines.
Lenghts are plotted as median (inside the box). Upper and lower hinges are 75th and 25th percentiles. The whiskers extend up to values that lie inside 1.5X inter-quartile range from each hinge. Outlying values are plotted separately.

Next, aggregated data for lengths of flagellar parts as defined in Fig. 5.17., namely the fully labelled part, the red (TMR) signal decay part, and the part devoid of the red signal, were plotted at each time point and for major TMR signal categories (Fig 5.33.). Generally, the length of the fully labelled part stayed constant in all categories. The length of the red signal decay part slightly increased over time. In all categories except the fully labelled flagella, flagella with the very distal part devoid of the red signal started to occur at 2 hours post labelling, and the mean length of this region increased over time.

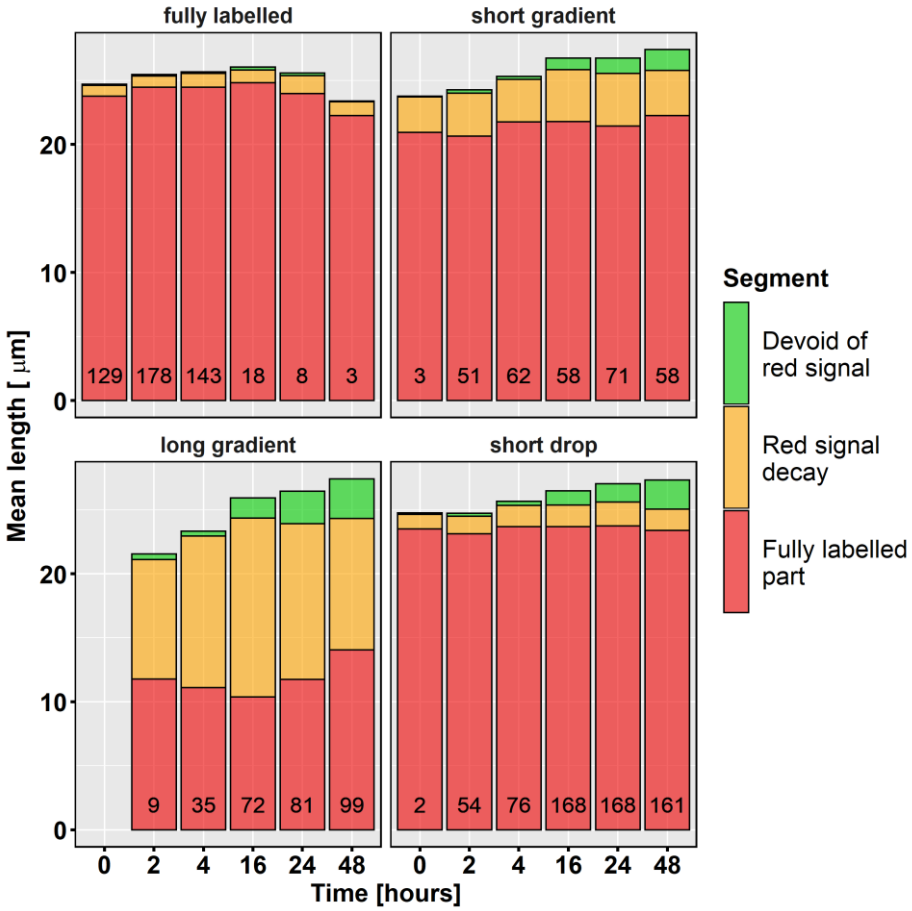

Figure 5.33. Mean lengths of flagellum parts for all cell lines.
On the Y-axis, the mean length of flagellum (μm) from its proximal end (base) to the distal end (tip) is indicated. On the X-axis, individual time points post labelling with TMR. **A**) Flagella in the fully labelled category. **B**) Flagella in the short gradient category. **C**) Flagella in the long gradient category. **D**) Flagella in the short drop category.

5.15 Changes to PFR2 signals at the proximal part of the flagellum

For none of the axonemal proteins included in the study a significant changes to the TMR signal were observed at the proximal end of the flagellum. The signal in this part of the flagellum is difficult to analyse as it is partially obstructed by the signal of the cell body (which may correspond to the cytosolic pool of the studied protein and a non-specific staining of the cytosol with TMR). However, in the cell line expressing tagged PFR2, a constituent of the paraflagellar rod, a non-axonemal cytoskeletal structure of the *T. brucei* flagellum, a region of TMR and mNeonGreen signal difference in the proximal part of the flagellum was observed from 2 hours on post TMR labelling (Fig. 5.34.). At 16 hours post labelling, this region was present in 75% of all examined cells (N = 20). Further experiments are needed to distinguish between the elongation of the PFR structure and its proximal turnover.

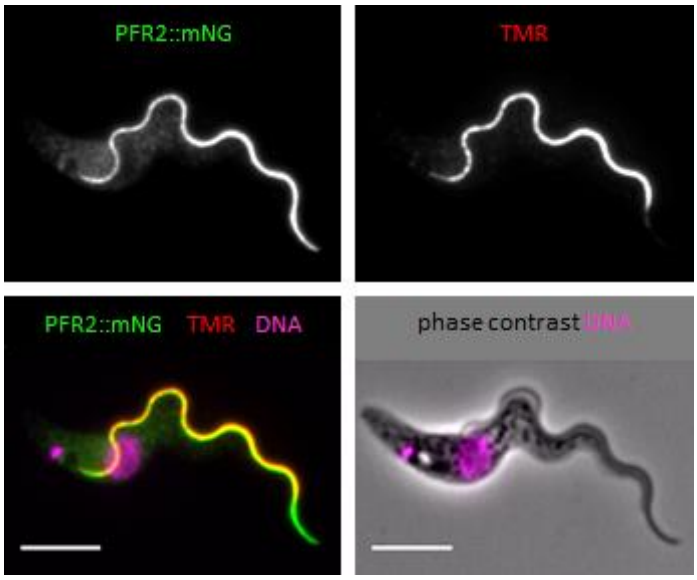

Figure 5.34. A region of TMR and mNeonGreen signal difference in the proximal part of the flagellum in PFR2::mNG-HaloTag cell line.
Cells expressing proteins tagged by mNG-HaloTag were labelled by TMR at the time point 0, then washed and observed at time point t = 16h. Fluorescence images show mNG (green) cell line, TMR (red), DNA stained by DAPI (magenta). Scale bars represent 5 μm.

5.16 Comparison of fluorescent intensities to assess turnover along flagella

To determine whether there is any turnover of cytoskeletal proteins along the flagellum, raw data from fluorescent microscopy images were used to obtain intensity plots for both green and red fluorescent signal. In theory, the plot of the green fluorescent signal should not change in time because it reflects the total population of a given protein in the flagellum. The red fluorescent signal, produced by TMR bound to HaloTag could decrease with time from TMR washout indicative of the protein turnover along the flagellum. Therefore, protein turnover would be detected as a decrease in the intensity of the TMR fluorescent signal compared to the intensity of the mNeonGreen signal in time.

TMR and mNG fluorescent intensities for 10 cell lines at 5 time points (0h, 2h, 4h, 16h, 24h, 48h) post labelling were analysed. The intensities were obtained by averaging an absolute intensity over a 3 μm region of the flagellum, located 3 μm from the point of decay towards the proximal end of the flagellum (area of mean intensity calculation in Fig. 5.17.). This particular region was selected because it was typically relatively close to the distal end of the flagellum where it was not blurred or obstructed by the second flagella, which could interfere with the observations. Moreover, it was far enough from the point of decay, the point where the intensities of the two signals diverge.

The analysis is summarised in Fig. 5.35. For each time point, mean intensities of TMR and mNeonGreen signals for all analysed cells of a particular cell line are plotted. In general, at t0 there is a clear correlation between TMR and mNeonGreen intensities across the cell lines (FAP20 and PFR2 show highest intensities in both channels, while CFAP43, DRC4, and IAD show the lowest intensities). Interestingly, all three RSP proteins show comparable intensities. FAP20 shows rather high variability in both intensities. In general, mNG intensities were relatively stable over time, with the exception of FAP20, in which an apparent decrease was observed. Some of the proteins show very stable TMR signal up to 48 hours (OAD2, DRC4, CFAP43). Other proteins (RSPs, IAD) show stable TMR intensities in the interval 0 – 24 hours followed by a decrease at 48 hours. For RSPs, the TMR signal at 48 hours was still above 50% of the initial intensity. In the case of FAP20 protein, the decrease in the TMR signal was mirrored by the decrease in the mNG intensity.

These observed variations in mNG signal between time points to technical limitations of the approach. Therefore, one solution to this problem would be an experiment where intensities of individual time points could be normalised by t0 intensities in the same image.

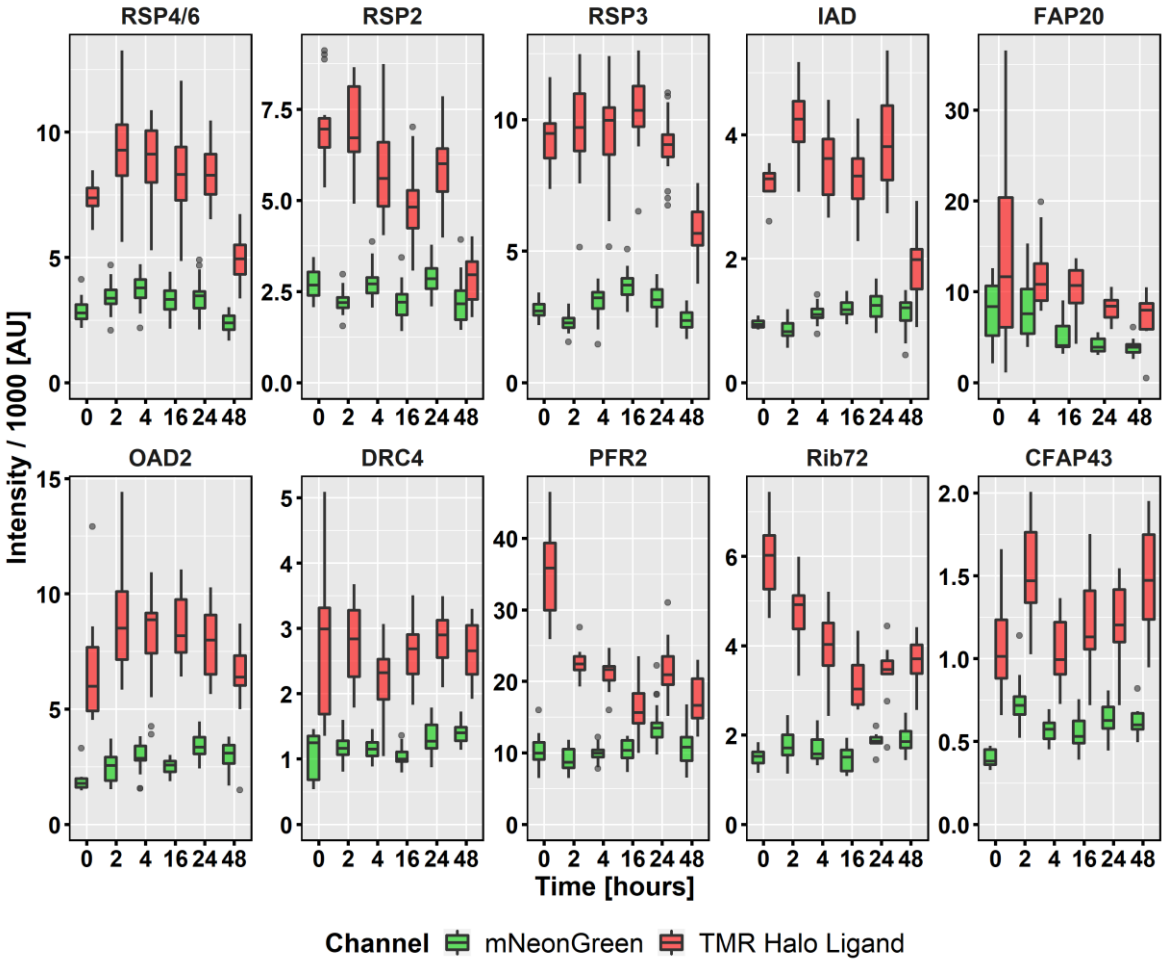

Figure 5.35. Fluorescence intensity plots comparisson of green (mNG) and red (TMR) signals.
Mean of absolute intensities in green and red fluorescent chanells for all cells at different time points (tx = 0, 2, 4, 16, 24, 48 hours).

Generally, the fluorescence intensities of red and green signals correlates (Fig. 5.36.). However, in the case of FAP20 cell line, intensities are dispersed, which could be explained by frequently observed phenotypes in case of FAP20 (Fig 5.26.).

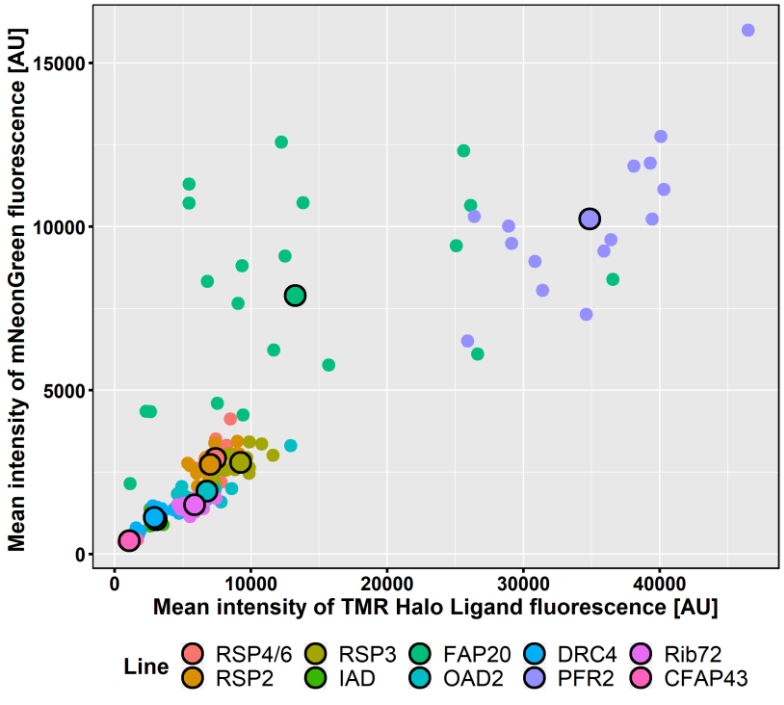

Figure 5.36. Fluorescence intensity corelation between green (mNG) and red (TMR) signals.
Layout of mean intensities (absolute) in green and red fluorescent chanells for all flagella analysed.

5.17 Differentiation fluorescence staining allows simultaneous imaging of cells from different time points

In order to distinguish between two cell populations mixed together in a single microscopic sample, a differentiation staining with a fluorescence-staining marker was applied. As living cells are being settled on a microscope slide, it was critical to identify a membrane-permeant dye/label able to stain living cells.

First, the staining of DNA with Hoechst 33342 Solution was tested. However, it was observed that although initially only one cell population was labelled, the dye was rapidly detectable also in nuclei of nearby cells of the second population upon cell fixation. It is possible that Hoechst used for staining of one population has leaked from the cells and caused undesired staining of all of the cells. As alternative, fluorescent markers: MTT CMX Ros and MTT Deep Red staining mitochondria were tested. In principle, both dyes were suitable; they were both present in mitochondria of only the initially labelled population, allowing for efficient differentiation of the two populations. MTT CMX Ros, however, emits in both TRITC and Cy5 emission spectra, which is problematic given usage of TMR in our experiments. MTT Deep Red emits only in the Cy5 and hence does not interfere with the TMR signal (Fig. 5.37.).

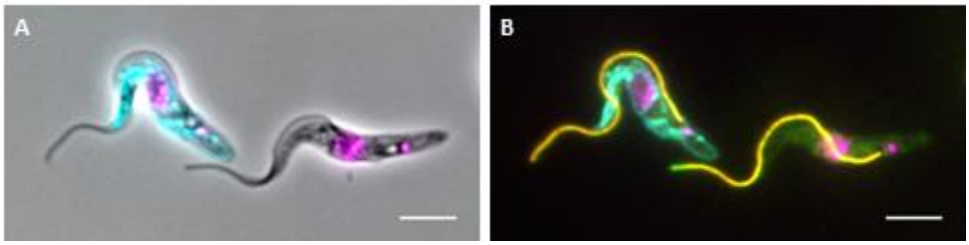

Figure 5.37. Differentiation between two cell populations by mitotracker staining. A,B) Cells from two populations in one field of view. On the left is a cell from a population stained with TMR ligand at the time point 0 and subsequently stained with mitotracker MT Deep Red. On the right is cell at time 4 hrs after TMR labelling. **A**) Phase contrast, mitochondrion stained with MT Deep Red (cyan) and DNA stained with DAPI (magenta). **B**) **Merge:** RSP4/6::mNG-HaloTag (green), TMR bound to HaloTag (red), DNA stained with DAPI (magenta), mitochondrion (cyan). Scale bars represent 5 μm.

Hence, a protocol enabling normalisation of intensities at different time points by t0 was successfully developed and when applied should decrease variability of signals due to technical limitations (changes in intensities of excitation light in time etc.).

6 Discussion

Cilia and flagella are eukaryotic organelles, which significance has been increasingly recognised. This has been boosted by discoveries of ciliary involvement in many developmental and physiological processes in the human body. As well as diseases resulting from malfunctioning of cilia. The number of identified proteins, in which mutations cause these diseases, increases rapidly over time. At the same time, new cutting edge technologies have been applied to newly identified questions of cilia biology. On the other hand, some of the knowledge regarding very basic biology of these organelles, such as the assembly and maintenance of the ciliary cytoskeleton, has not been systematically revisited since the initial experiments in the 70s and 80s of the last century.

To address the question of the ciliary cytoskeleton assembly and maintenance, this thesis utilised some of the recently developed approaches. These enabled an efficient and rapid tagging of *T. brucei* proteins in their endogenous loci (Poon *et al.*, 2012), thus preserving their native regulation. This allowed for protein constituents of a number of complexes of the flagellar cytoskeleton to be tagged without affecting their cellular levels, which may be critical for interpretation of some observations, and which is an improvement over past experiments. Another technology utilised in this work has been based on the HaloTag. This tag is in itself not fluorescent, but covalently binds fluorescently tagged membrane-permeable ligands. Therefore enabling to follow a population of a tagged protein present in a cell at a particular time point and to monitor the addition of newly synthesised protein molecules. This system was already successfully used to study the assembly and turnover of flagellar transition zone proteins in *T. brucei* (Dean *et al.*, 2016). In the presented work, a modification of this approach was used. Studied proteins of interest were tagged by the HaloTag and by mNeonGreen, which was a marker of an entire population of a protein in the cell as well as in the flagellum. Another advantage of using *T. brucei* is the fact that in this organism the flagellar assembly cycle is tightly linked to the cell cycle. Hence, both the old flagellum of a constant length and the new growing flagella may be present in one cell (McKean, 2003).

6.1 Generating and validating cell lines

In the course of this work, two approaches were used to tag trypanosome proteins in their endogenous loci. Initially, an approach based on cloning targeting sequences for homologous recombination into a vector was used (Poon *et al.*, 2012). At some point, an approach for tagging proteins using only a PCR product with the targeting sequences introduced by long primers *(Dean et al.*, 2015) was successfully set up in the laboratory, and due to its speed, it was also used in this work.

In total, 16 cell lines expressing endogenously tagged proteins of the axoneme, PFR, or structures at the distal end of the axoneme, were prepared. The correct integration of the tagging DNA was confirmed in each cell line by the tagging validation PCR on genomic DNA. Expression of tagged proteins of predicted molecular weights was confirmed for selected proteins by SDS-PAGE and western blotting using an antibody against the tag. Moreover, proper localisation of the tagged proteins was confirmed by fluorescence microscopy. In general, localisation of all the tagged proteins agreed with data in the whole *T. brucei* genome localisation project TrypTag.org. It was also consistent with previously published data, e.g. localisation of FCP4/TbKin15 and ASC1 to the flagellar distal end (Varga *et al.*, 2017), or localisation of RSP3 along the flagellum (Ralston *et al.*, 2006). Tubulin tagged with a large tag, such as a fluorescent protein, does no longer localises to the flagellum in *T. brucei,* which was previously also described (Sheriff *et al.*, 2014). This can be solved by using an extremely short tag, only 4 amino acid-long TC-tag (Crivat *et al.*, 2011). This tag binds a fluorescent ligand similarly to the HaloTag. Such a cell line has already been prepared but not tested yet, due to time limitations. A disadvantage of this system is high non-specific labelling, however, this can be reduced using BAL wash in mammalian cells (Martin *et al.*, 2005). This protocol can be optimised also in trypanosomes. Similar to *C. reinhardtii*, tubulin in *T. brucei* is very likely to be incorporated into the axoneme at its distal end (Johnson & Rosenbaum, 1992). It was shown that there is a gradient of tyrosinylated tubulin towards the distal end of the trypanosome axoneme. Detyrosinylation is known to occur after tubulin incorporation into the structure (Sherwin & Gull, 1989).

Another method of verification of correctly tagged proteins of interest was inducible depletion of selected tagged proteins (RSP4/6 and RPS3) by RNAi. A fluorescent signal of the tagged proteins was not detectable in a majority of cells upon RNAi induction. However, it persisted

in some cells, probably because they did not express the hairpin RNA targeting the respective mRNA. This may be related to an already described heterogeneity of the used system (Poon *et al.*, 2012).

The functioning of HaloTag labelling approach was confirmed by successful labelling of proteins with TMR-labelled HaloTag ligand. First, cells incubated with Coumarin, which prevented TMR labelling. Second, by using biotin-PEG HaloTag ligand. This biotin labelling did not work on living cells, most likely because the ligand could not enter them. However, it was possible to label proteins in flagella cytoskeletons after dissolving membranes by detergent, as shown by visualisation of biotin by addition of Streptavidin-Cy5 (Fig. 5.12). Flagellar cytoskeletons with biotinylated specific proteins will be useful in the future to attach them in a defined way to glass slides for microscopy experiments. In conclusion, it was confirmed that the HaloTag labelling approach is a useful and robust protein labelling method.

6.2 Incorporation of proteins into a growing axoneme occurs exclusively at its distal end

Using the HaloTag approach on 13 constituents of various axonemal complexes, it was found that an axoneme is built exclusively at the distal end. This is consistent with previously published observations in *T. brucei* (Subota *et al.*, 2014; Vincensini *et al.*, 2018) and *C. reinhardtii* (Johnson & Rosenbaum, 1992). Typically, there was no sharp boundary between the fully TMR-labelled part and the part devoid of the TMR signal in growing flagella. Instead, gradual decay of signal intensity was observed, similar to the long gradient category of mature flagella. Since the TMR-HaloTag ligand was removed after labelling, the existence of these gradients could indicate that a fraction of proteins can move in the flagellum even after their assembly into the axoneme. However, in the case of mature flagella a short drop category was prominent with a sharp decrease in TMR intensities, arguing against this possibility (although a change to protein mobility depending on whether the flagellum is being constructed or mature would be possible). Another possible explanation for the presence of the gradients in the new flagella is the existence of a cytosolic pool of the tagged proteins. This pool would also get labelled with TMR and hence would contribute to axonemal construction also after labelling. The intensity gradient would reflect the rate at which a particular protein is synthesised in the cell, the size of the cytosolic pool, the rate of protein import into the flagellum etc. The gradients could be caused by the addition of proteins at decreasing labelled to un-labelled ratio to the distal end of the axoneme. Alternatively, it could be explained by filling in gaps in a recently formed axonemal lattice, the process previously shown for DRC4. This protein was also demonstrated to be a cargo of IFT but can dissociate before reaching the distal end (Wren *et al*., 2013). Similar processes could also exist in the case of other axonemal proteins. Consistent with the fact that these new flagella become mature, similar gradients were observed also in the analysis of mature flagella. Intriguingly, not all proteins behaved the same way in time. For a majority of the studied proteins, the gradient categories were present already at 2 hours post TMR labelling. However, in the case of IAD and Rib72, the cells were very rare up to 4 hours after labelling (Fig. 5.25.). This was matched by a lack of gradients in new flagella of 2F cells at those time points (see Fig. 5.25.). This points towards these proteins having a relatively large cytoplasmic pool. Which should be tested by biochemical fractionation experiments in the future.

All three studied RSPs show similar patterns of incorporation into an axoneme. It was previously shown, that the radial spokes are assembled in subcomplexes in the cell body, and then imported into the flagellum (Qin *et al.*, 2004). This could explain the similarities observed

in this work. It is possible that constituents of other large complexes, such as the axonemal dynein complexes, will also behave in a similar way.

One protein that behaved differently in this analysis is FAP20. This protein is thought to form a junction of A and B tubules of MTDs. In many instances, the TMR intensity signal at various time points post labelling did not decay to zero in the distal part of the flagellum (Fig. 5.26). Which was observed in flagella belonging to short drop, short gradient and long gradient categories. This could indicate higher mobility of the protein in the axoneme than in the case of other studied proteins. Which may be caused by a smaller size of FAP20 (34.6 kDa), although the mNeonGreen-Halo tag would significantly increase it. Another difference of FAP20 was that an increase of the mNeonGreen signal starting approximately halfway along the flagellum towards the distal end was observed, while the TMR signal stayed constant (Fig. 5.26.). This was observed at all time points, except t0, during the experiment. An explanation for this could be a gradual increase in amounts of added protein to the distal end of the axoneme, possibly in combination with longitudinal incorporation in the distal half. Previously, it was reported in *C. reinhardtii* that FAP20 gets incorporated into the axoneme from its proximal end (Yanagisawa *et al.*, 2014). In the current work, no indication of this was observed in *T. brucei*, although as mentioned above in some ways this protein behaved differently to all other studied axonemal proteins.

In cells at later time points post TMR labelling, the old mature flagellum belonged to short drop or short gradient categories, containing a substantial part fully labelled with TMR. In these cells, the new flagellum was completely devoid of TMR signal (or this was below the level detectable in our experiments). This shows that there is no recycling of axonemal material from the old flagellum to the new one. This is different from *C. reinhardtii* (Song & Dentler, 2001), but consistent with previous reports of the two flagella being isolated organelles in *T. brucei* (Fort *et al.*, 2016).

6.3 Turnover at the distal end of the flagellum

One surprising observation was that proportions of fully labelled flagella at early time points dropped quicker than expected if all flagella, which were mature at the point of TMR labelling, stayed fully labelled. Therefore, these mature flagella must transit to different categories. Most likely they quickly transit to a short drop and short gradient categories, because a sum of the observed fully labelled, short drop and short gradient at various time points is similar to the expected proportions of the fully labelled category. Mean flagella length was almost constant up to 4 hours post labelling. Therefore, the decay of the TMR signal in the distal part of the flagellum was not caused by flagellar elongation. Instead, it must be caused by the turnover of the last approximately 1.5 µm of the axoneme. This could happen either by an exchange of protein within the distal part of the axoneme or by its disassembly followed by assembly of the same length. This is a very surprising finding, given that unlike in *C. reinhardtii* mature flagella are thought to be very stable and of constant length in *T. brucei* (Fort *et al.*, 2016; Vincensini *et al.*, 2018). Precise nature of this turnover will be studied in the future.

Interestingly, microtubule-depolymerising proteins from the kinesin-13 family do localise to the distal end of the axoneme (Chan & Ersfeld, 2010) and could be involved in this process. Also, a hint of a decrease in the length of mature old flagella in cells of 2F2K2N stage (just before cytokinesis) can be seen in a recently published work (Figure 4 in Abeywickrema *et al.*, 2019). Based on data presented here, the point in the cell cycle, when does this turnover event happen can be estimated. The short drop and short gradient mature flagella are present in cell culture already two hours post TMR labelling, and they are present only in cells with one flagellum. Hence, the turnover event happens at the latest two hours before the end of the 1F stage, and at earliest two hours before cells enter this stage (by going through cytokinesis). In the future, it would be interesting to improve this estimation by analysing earlier time points post labelling than 2 hours. It would also be possible to find out whether immediately after cytokinesis the cells inheriting the old flagellum already belong to the short drop or short gradient category. As well as whether the cells inheriting the new flagellum belong to the long gradient category as expected. Fortunately, markers were recently developed for distinguishing these cell types (Abeywickrema *et al.*, 2019).

6.4 Mature flagella elongation at later time points

After 16 hours post labelling, the total length of the flagella increased. As the fully labelled part of the flagella in the short drop and short gradient category did not change in length (Fig. 5.33.), the flagella growth must occur in the distal part past the decay point. This observation further shows that the length of mature flagella in procyclic cells is not absolutely set, and can be changed under specific conditions. The fact that the elongation occurred in the experiment makes interpreting data from later time points more complicated. Under standard conditions for culturing of *T. brucei* procyclic cells (typically in 5-10 mL of a liquid medium in culture flasks), no such elongation has been reported (over the range of cell densities used in the experiment). However, it has been noticed, that when cell cultures of procyclic cells reach stationary phase at high cell densities (around 3×10^7 cells/mL), their flagellum elongates. Although this was not adequately investigated yet. During experiments described in this work, cells were cultured in relatively small volumes of 200 µL on 96-well plates to reduce the amount of used HaloTag ligands. However, the growth rates decreased between 24 – 48 hours post labelling (Fig. 5.28.), although the densities of cells at 48 hours were only 2.5×10^7 cells/mL. Perhaps the cell cultures grow differently in the small volume on the plate than in larger volumes in flasks, approaching stationary phase at lower densities. In the future, the cell growth on a 96-well plate should be optimised or alternatively larger volumes of media used.

6.5 Turnover in other parts of the flagellum

Elucidation of possible turnover at the proximal end of the flagellum was not easy. Mainly because the signal from the cell body and the new flagellum interfered with measurements. However, no evidence for the proximal turnover of axonemal proteins was observed, which is consistent with published data in *C. reinhardtii* (Song & Dentler, 2001). However, changes to the signal at the proximal end, in addition to the distal end, were observed in the case of the PFR2 protein (Fig. 5.34). PFR is an extra-axonemal structure associated with the axonemal MTD (4 – 7) and connected directly with outer dyneins (Hughes *et al.*, 2012). Already at 4 hours post labelling the mNeonGreen signal extended beyond the TMR signal at its proximal end. This indicates elongation of PFR at this end However it is important to note that in the new flagella, only addition of PFR2 to the distal end was shown (Bastin *et al.*, 2000). Alternatively, there could be a short region of PFR2 turnover at the proximal end. Interestingly, CFAP43, which localises between PFR and the axoneme (Coutton *et al.*, 2018) did not show changes to proximal intensity and behaved like axonemal proteins.

Finally, assessing the turnover of proteins along the flagella in time was attempted. However, a significant variability, even in mNeonGreen signal in time, was observed. This indicates technical limitations (e.g. fluctuations in intensities of fluorescence excitation). One possible solution would be to image cells at each time point together with cells from t0 in a single field of view and use the t0 intensities to correct for the fluctuations.

7 Conclusions

This thesis contributed to knowledge about selected ciliary proteins behaviour and answered question about site of cilium constitution using modulatory labelling approach.

- Incorporation of proteins into a growing axoneme occurs explicitly at its distal end
- Protein turnover occurs at the short region at the distal end of the flagellum and happens around cytokinesis

8 References

Abeywickrema, M., Vachova, H., Farr, H., Mohr, T., Wheeler, R. J., Lai, D., … Varga, V. (2019). Non-equivalence in old- and new-flagellum daughter cells of a proliferative division in Trypanosoma brucei. *Molecular Microbiology*, *0*(0), 1–18. https://doi.org/10.1111/mmi.14345

Absalon, S., Blisnick, T., Bonhivers, M., Kohl, L., Cayet, N., Toutirais, G., … Bastin, P. (2008). Flagellum elongation is required for correct structure, orientation and function of the flagellar pocket in Trypanosoma brucei. *Journal of Cell Science*, *121*, 3704–3716. https://doi.org/10.1242/jcs.035626

Afzelius, B. A. (2004). Cilia-related diseases. *J. Pathol.* https://doi.org/10.1002/path.1652

Afzelius, Björn A. (1976). A Human Syndrome Caused by Immotile Cilia. *Science*, *193*(4250), 317–319. https://doi.org/doi:10.13102/sociobiology.v62i3.422 or http://periodicos.uefs.br/ojs/index.php/sociobiology/issue/archive

Banizs, B., Pike, M. M., Millican, C. L., Ferguson, W. B., Komlosi, P., Sheetz, J., … Yoder, B. K. (2005). Dysfunctional cilia lead to altered ependyma and choroid plexus function, and result in the formation of hydrocephalus. *Development*, *132*(23), 5329–5339. https://doi.org/10.1242/dev.02153

Barnes, R. L., Shi, H., Kolev, N. G., Tschudi, C., & Ullu, E. (2012). Comparative genomics reveals two novel RNAi factors in Trypanosoma brucei and provides insight into the core machinery. *PLoS Pathogens*, *8*(5). https://doi.org/10.1371/journal.ppat.1002678

Bastin, P., Ellis, K., Kohl, L., & Gull, K. (2000). Flagellum ontogeny in trypanosomes studied via an inherited and regulated RNA interference system. *Journal of Cell Science, 18*, 3321–3328.

Benz, C., Dondelinger, F., McKean, P. G., & Urbaniak, M. D. (2017). Cell cycle synchronisation of Trypanosoma brucei by centrifugal counter-flow elutriation reveals the timing of nuclear and kinetoplast DNA replication. *Scientific Reports*, *7*(1), 1–10. https://doi.org/10.1038/s41598-017-17779-z

Berriman, M., Ghedin, E., Hertz-fowler, C., Blandin, G., Renauld, H., Bartholomeu, D. C., … Carrington, M. (2005). The genome of the African trypanosome Trypanosoma brucei. *Science*, *309*(5733), 416–422.

Bloodgood, R. A. (2010). Sensory reception is an attribute of both primary cilia and motile cilia. *Journal of Cell Science*, *123*(4), 505–509. https://doi.org/10.1242/jcs.066308

Bloodgood, Robert A. (2009). *Background From Central to Rudimentary to Primary : The History of an Underappreciated Organelle Whose Time Has Come . The Primary Cilium*. *Methods in Cell Biology: VOLUME 94* (First edit, Vol. 94). Elsevier. https://doi.org/10.1016/S0091-679X(08)94001-2

Blyth, M., & Wellesley, D. (2008). Ectopic pregnancy in primary ciliary dyskinesia. *Journal of Obstetrics and Gynaecology*, *28*(3), 358. https://doi.org/10.1080/01443610802058742

Boulter, C., Mulroy, S., Webb, S., Fleming, S., Brindle, K., & Sandford, R. (2001). Cardiovascular, skeletal, and renal defects in mice with a targeted disruption of the Pkd1 gene. *Proceedings of the National Academy of Sciences*, *98*(21), 12174–12179. https://doi.org/10.1073/pnas.211191098

Bower, R., Tritschler, D., VanderWaal, K., Perrone, C. A., Mueller, J., Fox, L., … Porter, M. E. (2013).

The N-DRC forms a conserved biochemical complex that maintains outer doublet alignment and limits microtubule sliding in motile axonemes. *Molecular Biology of the Cell*, *24*(8), 1134–1152. https://doi.org/10.1091/mbc.E12-11-0801

Bower, Raqual, Tritschler, D., Mills, K. V., Heuser, T., Nicastro, D., & Porter, M. E. (2018). DRC2/CCDC65 is a central hub for assembly of the nexin–dynein regulatory complex and other regulators of ciliary and flagellar motility. *Molecular Biology of the Cell*, *29*(2), 137–153. https://doi.org/10.1091/mbc.E17-08-0510

Branche, C., Kohl, L., Toutirais, G., Buisson, J., Cosson, J., & Bastin, P. (2006). Conserved and specific functions of axoneme components in trypanosome motility. Journal of *Cell Science.*, *119*, 3443–3455. https://doi.org/10.1242/jcs.03078

Brun, R., & Schönenberger. (1979). Cultivation and in vitro cloning or procyclic culture forms of Trypanosoma brucei in a semi-defined medium. Short communication. *Acta Tropica*, *36*(1979), 289–292. https://doi.org/10.5169/seals-312533

Carbajal-González, I. B., Heuser, T., Fu, X., Lin, J., Smith, B. W., Mitchell, D. R., & Nicastro, D. (2013). Conserved structural motifs in the central pair complex of eukaryotic flagella. *Cytoskeleton*, *70*(2), 101–120. https://doi.org/10.3899/jrheum.121180.Response

Carvalho-Santos, Z., Azimzadeh, J., Pereira-Leal, J. B., & Bettencourt-Dias, M. (2011). Tracing the origins of centrioles, cilia, and flagella. *Journal of Cell Biology*, *194*(2), 165–175. https://doi.org/10.1083/jcb.201011152

Chan, K. Y., & Ersfeld, K. (2010). The role of the Kinesin-13 family protein TbKif13-2 in flagellar length control of Trypanosoma brucei. *Molecular and Biochemical Parasitology*, *174*(2), 137–140. https://doi.org/10.1016/j.molbiopara.2010.08.001

Coutton, C., Vargas, A. S., Amiri-Yekta, A., Kherraf, Z. E., Ben Mustapha, S. F., Le Tanno, P., … Ray, P. F. (2018). Mutations in CFAP43 and CFAP44 cause male infertility and flagellum defects in Trypanosoma and human. *Nature Communications*, *9*(1), . https://doi.org/10.1038/s41467-017-02792-7

Crivat, G., Tokumasu, F., Sa, J. M., Hwang, J., & Wellems, T. E. (2011). Tetracysteine-based fluorescent tags to study protein localization and trafficking in plasmodium falciparum-infected erythrocytes. *PLoS ONE*. 6(8): e22975. https://doi.org/10.1371/journal.pone.0022975

Croft, J. T., Zabeo, D., Subramanian, R., & Hoog, J. L. (2018). Composition, structure and function of the eukaryotic flagellum distal tip. *Essays Biochem*, *62*(October), 815– 828. https://doi.org/10.1042/EBC20180032

Curry, A. M., Williams, B. D., & Rosenbaum, J. L. (1992). Sequence analysis reveals homology between two proteins of the flagellar radial spoke. *Molecular and Cellular Biology*, *12*(9), 3967–3977. https://doi.org/10.1128/MCB.12.9.3967.Updated

Dabdoub, A., & Kelley, M. W. (2005). Planar cell polarity and a potential role for a Wnt morphogen gradient in stereociliary bundle orientation in the mammalian inner ear. *Journal of Neurobiology*, *64*(4), 446–457. https://doi.org/10.1002/neu.20171

Dallai, R., Afzelius, B. A., & Mamaev, B. (1996). Flagellar axonemes with 10 microtubular doublets in spermatozoa from gall-midges (Diptera, Cecidomyiidae). *Acta Zoologica*, *77*(2), 153–160. https://doi.org/10.1111/j.1463-6395.1996.tb01259.x

Dawe, H. R., Shaw, M. K., Farr, H., & Gull, K. (2007). The hydrocephalus inducing gene product, Hydin, positions axonemal central pair microtubules. *BMC Biology*, *5*(33), 1–10. https://doi.org/10.1186/1741-7007-5-33

Dean, S., Moreira-Leite, F., Varga, V., & Gull, K. (2016). Cilium transition zone proteome reveals compartmentalization and differential dynamics of ciliopathy complexes. *Proceedings of the National Academy of Sciences of the United States of America*, *113*(35), E5135-43. https://doi.org/10.1073/pnas.1604258113

Dean, S., Sunter, J. D., & Wheeler, R. J. (2017). TrypTag.org: A Trypanosome Genome-wide Protein Localisation Resource. *Trends in Parasitology*, *33*(2), 80–82. https://doi.org/10.1016/j.pt.2016.10.009

Dean, S., Sunter, J., Wheeler, R. J., Hodkinson, I., Gluenz, E., & Gull, K. (2015). A toolkit enabling efficient, scalable and reproducible gene tagging in trypanosomatids. *Open Biology*, *5*(1), 140197. https://doi.org/10.1098/rsob.140197

Deflorin, J., Rudolf, M., & Seebeck, T. (1994). The major components of the paraflagellar rod of Trypanosoma brucei are two similar, but distinct proteins which are encoded by two different gene loci. *Journal of Biological Chemistry*, *269*(46), 28745–28751.

Dymek, E. E., & Smith, E. F. (2007). A conserved CaM- and radial spoke-associated complex mediates regulation of flagellar dynein activity. *Journal of Cell Biology*, *179*(3), 515–526. https://doi.org/10.1083/jcb.200703107

Edwards, B. F. L., Wheeler, R. J., Barker, A. R., Moreira-Leite, F. F., Gull, K., & Sunter, J. D. (2018). Direction of flagellum beat propagation is controlled by proximal/distal outer dynein arm asymmetry. *Proceedings of the National Academy of Sciences*, *115*(31), E7341–E7350. https://doi.org/10.1073/PNAS.1805827115

El-Sayed, N. M., Myler, P. J., Blandin, G., Berriman, M., Crabtree, J., Aggarwal, G., … Hall, N. (2005). Comparative genomics of trypanosomatid parasitic protozoa. *Science*, *309*(5733), 404–409. https://doi.org/10.1126/science.1112181

Encell, L. P., Ohana, R. F., Zimmerman, K., Otto, P., Vidugiris, G., Wood, M. G., … Wood, K. V. (2012). Development of a Dehalogenase-Based Protein Fusion Tag Capable of Rapid, Selective and Covalent Attachment to Customizable Ligands. *Current Chemical Genomics*, *6*(1), 55–71. https://doi.org/10.2174/1875397301206010055

Eriksson, M., Ansved, T., Anvret, M., & Carey, N. (2001). A mammalian Radial Spokehead-Like gene, RSHL1, at the myotonic dystrophy-1 locus. *Biochemical and Biophysical Research Communications*, *281*(4), 835–841. https://doi.org/10.1006/bbrc.2001.4465

Fliegauf, M., Benzing, T., & Omran, H. (2007). When cilia go bad: cilia defects and ciliopathies. *Nat Rev Mol Cell Biol*, *8*(11), 880–893. https://doi.org/10.1038/nrm2278

Flock, A., & Duvall, A. J. (1965). The ultrastructure of the kinocilium of the sensory cells in the inner ear and lateral line organs. *The Journal of Cell Biology*, *25*, 1–8. https://doi.org/10.1083/jcb.25.1.1

Fort, C., Bonnefoy, S., Kohl, L., & Bastin, P. (2016). Intraflagellar transport is required for the maintenance of the trypanosome flagellum composition but not length. *Journal of Cell Science*, jcs.188227. https://doi.org/10.1242/jcs.188227

Froger, A., & Hall, J. E. (2007). Transformation of Plasmid DNA into E. coli Using the Heat Shock Method. *Journal of Visualized Experiments*, (6), 2007. https://doi.org/10.3791/253

Garcia-gonzalo, F. R., & Reiter, J. F. (2016). Open Sesame: How transition fibers and the transition zone control ciliary composition. *Cold Spring Harb. Perspect. Biol.*, *9*, a028134.

Garcia, G., Raleigh, D. R., & Reiter, J. F. (2018). How the ciliary membrane is organized inside-out to communicate outside-in. *Current Biology*, *28*(8), 421–434.

https://doi.org/10.1016/j.cub.2018.03.010

Gibson, W., Peacock, L., Ferris, V., Fischer, K., Livingstone, J., Thomas, J., & Bailey, M. (2015). Genetic Recombination between Human and Animal Parasites Creates Novel Strains of Human Pathogen. *PLoS Neglected Tropical Diseases*, *9*(3), 1–16. https://doi.org/10.1371/journal.pntd.0003665

Gilliam, J. C., Chang, J. T., Sandoval, I. M., Zhang, Y., Li, T., Pittler, S. J., … Wensel, T. G. (2012). Three-dimensional architecture of the rod sensory cilium and its disruption in retinal neurodegeneration. *Cell*, *151*(5), 1029–1041. https://doi.org/10.1016/j.cell.2012.10.038

Gonçalves, J., & Pelletier, L. (2017). Molecules and Cells The Ciliary Transition Zone : Finding the Pieces and Assembling the Gate, *40*(4), 243–253.

Gresh, L., Fischer, E., Reimann, A., Tanguy, M., Garbay, S., Shao, X., … Pontoglio, M. (2004). A transcriptional network in polycystic kidney disease. *EMBO Journal*, *23*(7), 1657–1668. https://doi.org/10.1038/sj.emboj.7600160

Hayes, P., Varga, V., Olego-Fernandez, S., Sunter, J., Ginger, M. L., & Gull, K. (2014). Modulation of a cytoskeletal calpain-like protein induces major transitions in trypanosome morphology. *Journal of Cell Biology*, *206*(3), 377–384. https://doi.org/10.1083/jcb.201312067

Heuser, T., Dymek, E. E., Lin, J., Smith, E. F., & Nicastro, D. (2012). The CSC connects three major axonemal complexes involved in dynein regulation. *Molecular Biology of the Cell*, *23*(16), 3143–3155. https://doi.org/10.1091/mbc.E12-05-0357

Hodges, M. E., Wickstead, B., Gull, K., & Langdale, J. A. (2011). Conservation of ciliary proteins in plants with no cilia. *BMC Plant Biology*, *11*(1), 185. https://doi.org/10.1186/1471-2229-11-185

Hughes, L. C., Ralston, K. S., Hill, K. L., & Zhou, Z. H. (2012). Three-dimensional structure of the trypanosome flagellum suggests that the paraflagellar rod functions as a biomechanical spring. *PLoS ONE*, *7*(1). https://doi.org/10.1371/journal.pone.0025700

Ichikawa, M., Liu, D., Kastritis, P. L., Basu, K., Hsu, T. C., Yang, S., & Bui, K. H. (2017). Subnanometre-resolution structure of the doublet microtubule reveals new classes of microtubule-associated proteins. *Nature Communications*, *8*(May), 1–12. https://doi.org/10.1038/ncomms15035

Ikeda, K., Brown, J. A., Yagi, T., Norrander, J. M., Hirono, M., Eccleston, E., … Linck, R. W. (2003). Rib72, a conserved protein associated with the ribbon compartment of flagellar A-microtubules and potentially involved in the linkage between outer doublet microtubules. *Journal of Biological Chemistry*, *278*(9), 7725–7734. https://doi.org/10.1074/jbc.M210751200

Inoue, M., Nakamura, Y., Yasuda, K., Yasaka, N., Hara, T., Schnaufer, A., … Fukuma, T. (2005). The 14-3-3 proteins of Trypanosoma brucei function in motility, cytokinesis, and cell cycle. *Journal of Biological Chemistry*, *280*(14), 14085–14096. https://doi.org/10.1074/jbc.M412336200

Ishikawa, T. (2017). Axoneme structure from motile cilia. *Cold Spring Harbor Perspectives in Biology*, *9*(1). https://doi.org/10.1101/cshperspect.a028076

Jackson, A. P. (2007). Evolutionary consequences of a large duplication event in Trypanosoma brucei: Chromosomes 4 and 8 are partial duplicons. *BMC Genomics*, *8*(432), 1-17. https://doi.org/10.1186/1471-2164-8-432

Jékely, G., & Arendt, D. (2006). Evolution of intraflagellar transport from coated vesicles and autogenous origin of the eukaryotic cilium. *BioEssays*, *28*(2), 191–198. https://doi.org/10.1002/bies.20369

Johnson, K. A., & Rosenbaum, J. L. (1992). Polarity of flagellar assembly in Chlamydomonas. *Journal*

of Cell Biology, *119*(6), 1605–1611. https://doi.org/10.1083/jcb.119.6.1605

Kabututu, Z. P., Thayer, M., Melehani, J. H., & Hill, K. L. (2010). CMF70 is a subunit of the dynein regulatory complex. *Journal of Cell Science*, *123*(20), 3587–3595. https://doi.org/10.1242/jcs.073817

Keil, T. A. (2012). Sensory cilia in arthropods. *Arthropod Structure and Development*, *41*(6), 515–534. https://doi.org/10.1016/j.asd.2012.07.001

Kempeneers, C., & Chilvers, M. A. (2018). To beat, or not to beat, that is question! The spectrum of ciliopathies. *Pediatric Pulmonology*, *53*(8), 1122–1129. https://doi.org/10.1002/ppul.24078

Khan, S., & Scholey, J. M. (2018). Assembly, functions and evolution of archaella, flagella and cilia. *Current Biology*, *28*(6), 278–292. https://doi.org/10.1016/j.cub.2018.01.085

King, S. M. (2016). Axonemal dynein arms. *Cold Spring Harbor Perspectives in Biology*, *8*(11), 1–12. https://doi.org/10.1101/cshperspect.a028100

Kohl, L., Sherwin, T., & Gull, K. (1999). Assembly of the paraflagellar rod and the flagellum attachment zone complex during the Trypanosoma brucei cell cycle. *J Eukaryot Microbiol*, *46*, 105–109. https://doi.org/10.1111/j.1550-7408.1999.tb04592.x

Koyfman, A. Y., Schmid, M. F., Gheiratmand, L., Fu, C. J., Khant, H. A., Huang, D., … Chiu, W. (2011). Structure of Trypanosoma brucei flagellum accounts for its bihelical motion. *Proceedings of the National Academy of Sciences*, *108*(27), 11105–11108. https://doi.org/10.1073/pnas.1103634108

Kozminski, K. G., Beech, P. L., & Rosenbaum, J. L. (1995). *Chlamydomonas Kinesin-like protein FLA10 is involved in motility associated with the flagellar membrane*.

Kuehni, C. E., Frischer, T., Strippoli, M. P. F., Maurer, E., Bush, A., Nielsen, K. G., … Barbato, A. (2010). Factors influencing age at diagnosis of primary ciliary dyskinesia in European children. *European Respiratory Journal*, *36*(6), 1248–1258. https://doi.org/10.1183/09031936.00001010

Kulakova, A. N., Larkin, M. J., & Kulakov, L. A. (1997). The plasmid-located haloalkane dehalogenase gene from Rhodococcus rhodochrous NCIMB 13064. *Microbiology*, *143*(1), 109–115. https://doi.org/10.1099/00221287-143-1-109

Lacomble, S., Portman, N., & Gull, K. (2009). A protein-protein interaction map of the Trypanosoma brucei paraflagellar rod. *PLoS ONE*, *4*(11), e7685. https://doi.org/10.1371/journal.pone.0007685

Laemmli, U. K. (1970). Cleavage of structural proteins during the assembly of the head of bacteriophage T4. *Nature*, *227*(August 15th), 680–685.

Langousis, G., & Hill, K. L. (2014). Motility and more: the flagellum of Trypanosoma brucei. *Nature Reviews. Microbiology*, *12*(7), 505–518. https://doi.org/10.1038/nrmicro3274

Lechtreck, Karl F., Van De Weghe, J. C., Harris, J. A., & Liu, P. (2017). Protein transport in growing and steady-state cilia. *Traffic*, *18*(5), 277–286. https://doi.org/10.1111/tra.12474

Lechtreck, Karl Ferdinand, Gould, T. J., & Witman, G. B. (2013). Flagellar central pair assembly in Chlamydomonas reinhardtii. *Cilia*, *2*(15), 1–19. https://doi.org/10.1186/2046-2530-2-15

Li, X., Xu, L., Li, J., Li, B., Bai, X., Strauss, J. F., … Wang, H. (2014). Otitis media in sperm-associated antigen 6 (Spag6)-deficient mice. *PLoS ONE*, *9*(11), 2–9. https://doi.org/10.1371/journal.pone.0112879

Los, G. V, Encell, L. P., Mcdougall, M. G., Hartzell, D. D., Karassina, N., Zimprich, C., … Wood, K. V.

(2008). HaloTag: A novel protein labeling technology for cell imaging and protein analysis. *ACS Chem. Biol.*, *3*(6), 373–382.

Lyons, R. A., Saridogan, E., & Djahanbakhch, O. (2006, July). The reproductive significance of human Fallopian tube cilia. *Human Reproduction Update*. https://doi.org/10.1093/humupd/dml012

Mao, S., Shah, A. S., Moninger, T. O., Ostedgaard, L. S., Lu, L., Tang, X. X., … Welsh, M. J. (2018). Motile cilia of human airway epithelia contain hedgehog signaling components that mediate noncanonical hedgehog signaling. *Proceedings of the National Academy of Sciences*, *0*, 201719177. https://doi.org/10.1073/pnas.1719177115

Marshall, W. F., & Rosenbaum, J. L. (2001). Intraflagellar transport balances continuous turnover of outer doublet microtubules: implications for flagellar length control. *The Journal of Cell Biology*, *155*(3), 405–414. https://doi.org/10.1083/jcb.200106141

Martin, B. R., Giepmans, B. N. G., Adams, S. R., & Tsien, R. Y. (2005). Mammalian cell-based optimization of the biarsenical-binding tetracysteine motif for improved fluorescence and affinity. *Nature Biotechnology*, *23*(10), 1308–1314. https://doi.org/10.1038/nbt1136

Matthews, K. R. (2005). The developmental cell biology of Trypanosoma brucei. *Journal of Cell Science*, *118*(2), 283–290. https://doi.org/10.1242/jcs.01649

McKean, P. G. (2003). Coordination of cell cycle and cytokinesis in Trypanosoma brucei. *Current Opinion in Microbiology*, *6*(6), 600–607. https://doi.org/10.1016/j.mib.2003.10.010

Mitchell, D. R. (2003). Reconstruction of the projection periodicity and surface architecture of the flagellar central pair complex. *Cell Mot Cytoskeleton.*, *55*(3), 188–199. https://doi.org/10.1002/cm.10121

Mitchison, H. M., Schmidts, M., Loges, N. T., Freshour, J., Dritsoula, A., Hirst, R. A., … Mitchell, D. R. (2012). Mutations in axonemal dynein assembly factor DNAAF3 cause primary ciliary dyskinesia. *Nature Genetics*, *44*(4), 381–389. https://doi.org/10.1038/ng.1106

Nauli, S. M., Alenghat, F. J., Luo, Y., Williams, E., Vassilev, P., Li, X., … Zhou, J. (2003). Polycystins 1 and 2 mediate mechanosensation in the primary cilium of kidney cells. *Nature Genetics*, *33*(2), 129–137. https://doi.org/10.1038/ng1076

Neugebauer, D. C., Neuwinger, J., Jockenhövel, F., & Nieschlag, E. (1990). “9 + 0” Axoneme in Spermatozoa and Some Nasal Cilia of a Patient With Totally Immotile Spermatozoa Associated With Thickened Sheath and Short Midpiece. *Human Reproduction*, *5*(8), 981–986. https://doi.org/10.1093/oxfordjournals.humrep.a137232

Nguyen, H. K. T., Sandhu, J., Langousis, G., & Hill, K. L. (2013). CMF22 is a broadly conserved axonemal protein and is required for propulsive motility in Trypanosoma brucei. *Eukaryotic Cell*, *12*(9), 1202–1213. https://doi.org/10.1128/EC.00068-13

Nicastro, D., Fu, X., Heuser, T., Tso, A., Porter, M. E., & Linck, R. W. (2011). Cryo-electron tomography reveals conserved features of doublet microtubules in flagella. *Proceedings of the National Academy of Sciences*, *108*(42), E845–E853. https://doi.org/10.1073/pnas.1106178108

Nicastro, Daniela, Schwartz, C., Pierson, J., Gaudette, R., Porter, M. E., & Mcintosh, J. R. (2007). The molecular architecture of axonemes revealed by cryoelectron tomography. *Science*, *313*(2006), 944–948. https://doi.org/10.1126/science.1128618

Nonaka, S., Shiratori, H., Saijoh, Y., & Hamada, H. (2002). Determination of L-R patterning of mouse embryo by nodal flow. *Nature*, *418*(July), 96–99. https://doi.org/10.1038/nature00849

Nonaka, S., Tanaka, Y., Okada, Y., Takeda, S., Harada, A., Kanai, Y., … Hirokawa, N. (1998).

Randomization of left–right asymmetry due to loss of nodal cilia generating a leftward flow of extraembryonic fluid in mice. *Cell*, *95*, 829–837.

Oda, T., Yanagisawa, H., Kamiya, R., & Kikkawa, M. (2014). A molecular ruler determines the repeat length in eukaryotic cilia and flagella. *Science*, *346*(6211), 857–860. https://doi.org/10.1126/science.1260214

Ohashi, Y., Nakai, Y., Kihara, S., Maruoka, K., Ikeoka, H., & Uemura, Y. (1985). The ciliary activity of the middle ear lining-functional and morphological observation. *Auris Nasus Larynx*, *12*, S123–S125. https://doi.org/10.1016/S0385-8146(85)80122-X

Okada, Y., Takeda, S., Tanaka, Y., Belmonte, J. C. I., & Hirokawa, N. (2005). Mechanism of nodal flow: A conserved symmetry breaking event in left-right axis determination. *Cell*, *121*(4), 633–644. https://doi.org/10.1016/j.cell.2005.04.008

Okamoto, S., Chaya, T., Omori, Y., Kuwahara, R., Kubo, S., Sakaguchi, H., & Furukawa, T. (2017). Ick ciliary kinase is essential for planar cell polarity formation in inner ear hair cells and hearing function. *The Journal of Neuroscience*, *37*(8), 2073–2085. https://doi.org/10.1523/jneurosci.3067-16.2017

Olbrich, H., Schmidts, M., Werner, C., Onoufriadis, A., Loges, N. T., Raidt, J., … Omran, H. (2012). Recessive HYDIN mutations cause primary ciliary dyskinesia without randomization of left-right body asymmetry. *American Journal of Human Genetics*. https://doi.org/10.1016/j.ajhg.2012.08.016

Orbach, R., & Howard, J. (2019). The dynamic and structural properties of axonemal tubulins support the high length stability of cilia. *Nature Communications*. https://doi.org/10.1038/s41467-019-09779-6

Owa, M., Uchihashi, T., Yanagisawa, H. aki, Yamano, T., Iguchi, H., Fukuzawa, H., … Kikkawa, M. (2019). Inner lumen proteins stabilize doublet microtubules in cilia and flagella. *Nature Communication*, *10*(1), 1–10. https://doi.org/10.1038/s41467-019-09051-x

Panigrahy, A., Lee, V., Ceschin, R., Zuccoli, G., Beluk, N., Khalifa, O., … Lo, C. W. (2016). Brain dysplasia associated with ciliary dysfunction in infants with congenital heart disease. *Journal of Pediatrics*, *178*, 141-148.e1. https://doi.org/10.1016/j.jpeds.2016.07.041

Pazour, G. J., Agrin, N., Walker, B. L., & Witman, G. B. (2006). Identification of predicted human outer dynein arm genes: Candidates for primary ciliary dyskinesia genes. *J Med Genet.*, *43*(1), 62–73. https://doi.org/10.1136/jmg.2005.033001

Pazour, Gregory J. (2004). Comparative genomics: Prediction of the ciliary and basal body proteome. *Current Biology*, *14*(14), 575–577. https://doi.org/10.1016/j.cub.2004.07.017

Pigino, G., & Ishikawa, T. (2012). Axonemal radial spokes: 3D structure, function and assembly. *Bio Architecture*, *2*(2), 50–58. https://doi.org/10.1083/jcb.201106125

Poon, S. K., Peacock, L., Gibson, W., Gull, K., & Kelly, S. (2012). A modular and optimized single marker system for generating Trypanosoma brucei cell lines expressing T7 RNA polymerase and the tetracycline repressor. *Open Biology*, *2*(FEBRUARY). https://doi.org/10.1098/rsob.110037

Qin, H., Diener, D. R., Geimer, S., Cole, D. G., & Rosenbaum, J. L. (2004). Intraflagellar transport (IFT) cargo: IFT transports flagellar precursors to the tip and turnover products to the cell body. *The Journal of Cell Biology*, *164*(2), 255–266. https://doi.org/10.1083/jcb.200308132

Ralston, K., Lerner, A., & Hill, K. (2006). Flagellar motility is essential for cytokinesis in Trypanosoma brucei and is modulated by an evolutionarily-conserved dynein regulatory system. *Eukaryotic Cell*, *5*(4), 696–711. https://doi.org/10.1128/EC.5.4.696

Rawlins, E. L., & Hogan, B. L. M. (2008). Ciliated epithelial cell lifespan in the mouse trachea and lung. *American Journal of Physiology- Lung Cellular Molecular Physiology*, *295*, 231–234. https://doi.org/10.1152/ajplung.90209.2008

Redmond, S., Vadivelu, J., & Field, M. C. (2003). RNAit: An automated web-based tool for the selection of RNAi targets in Trypanosoma brucei. *Molecular and Biochemical Parasitology*, *128*(1), 115–118. https://doi.org/10.1016/S0166-6851(03)00045-8

Satir, P., Pedersen, L. B., & Christensen, S. T. (2010). The primary cilium at a glance. *Journal of Cell Science*, *123*(4), 499–503. https://doi.org/10.1242/jcs.050377

Satir, Peter. (1995). Landmarks in Cilia Research From Leeuwenhoek to Us, *Cell Motil Cytoskeleton*. *32*(2), 90-94.

Sawamoto, K., Wichterle, H., Gonzalez-Perez, O., Cholfin, J. A., Yamada, M., Spassky, N., … Alvarez-Buylla, A. (2006). New neurons follow the flow of cerebrospinal fluid in the adult brain. *Science*, *311*(5761), 629–632. https://doi.org/10.1126/science.1119133

Schneider, C. A., Rasband, W. S., & Eliceiri, K. W. (2012). NIH Image to ImageJ: 25 years of Image Analysis HHS Public Access. *Nature Methods*, *9*(7), 671–675. https://doi.org/10.1038/nmeth.2089

Shah, A. S., Ben-Shahar, Y., Moninger, T. O., Kline, J. N., & Welsh, M. J. (2009). Motile Cilia of Human Airway Epithelia Are Chemosensory. *Science*, 325(5944): 1131-1134. https://doi.org/10.1126/science.1173869

Sheriff, O., Lim, L.-F., & He, C. Y. (2014). Tracking the Biogenesis and Inheritance of Subpellicular Microtubule in Trypanosoma brucei with Inducible YFP-alpha-Tubulin. *BioMed Research International, 6(12), 312-328.* https://doi.org/10.1155/2014/893272

Sherwin, T., & Gull, K. (1989). Visualization of detyrosination along single microtubules reveals novel mechanisms of assembly during cytoskeletal duplication in trypanosomes. *Cell*, *57*, 211–221. https://doi.org/10.1016/0092-8674(89)90959-8

Soares, H., Carmona, B., Nolasco, S., Melo, L. V., & Gonçalves, J. (2019). Cilia distal domain : diversity in evolutionarily conserved structures. *Cells*, *8*(160). https://doi.org/10.3390/cells8020160

Song, L., & Dentler, W. L. (2001). Flagellar protein dynamics in chlamydomonas. *Journal Biological Chemistry*, *276*(32), 29754–29763. https://doi.org/10.1074/jbc.M103184200

Sorokin, S. P. (1968). Reconstructions of centriole formation and ciliogenesis in mammalian lungs. *Journal of Cell Science*, *3*, 207–230.

Stepanek, L., & Pigino, G. (2016). Microtubule doublets are double-track railways for intraflagellar transport trains, *Science. 352*(6286), 721-724.

Stripp, B. R., & Reynolds, S. D. (2008). Maintenance and repair of the bronchiolar epithelium. *Proceedings of the American Thoracic Society*. https://doi.org/10.1513/pats.200711-167dr

Subota, I., Julkowska, D., Vincensini, L., Reeg, N., Buisson, J., Blisnick, T., … Bastin, P. (2014). Proteomic analysis of intact flagella of procyclic *trypanosoma brucei* cells identifies novel flagellar proteins with unique sub-localization and dynamics. *Molecular & Cellular Proteomics*, *13*(7), 1769–1786. https://doi.org/10.1074/mcp.M113.033357

Sunter, J. D., Varga, V., Dean, S., & Gull, K. (2015). A dynamic coordination of flagellum and cytoplasmic cytoskeleton assembly specifies cell morphogenesis in trypanosomes. *Journal of Cell Science*, *128*(8), 1580–1594. https://doi.org/10.1242/jcs.166447

Tilney, L. G., & Gibbins, J. R. (1968). Differential effects of antimitotic agents on the stability and behavior of cytoplasmic and ciliary microtubules. *Protoplasma*, *65*(1–2), 167–179. https://doi.org/10.1007/BF01666377

Toyama, Y., Sumiya, H., Fuse, H., & Shimazaki, J. (2009). A case of an infertile man with short-tailed spermatozoa. *Andrologia*, *28*(2), 81–87. https://doi.org/10.1111/j.1439-0272.1996.tb02761.x

Trindade, S., Rijo-ferreira, F., Pinto-neves, D., Guegan, F., Aresta-Branco, F., Bento, F., … Figueiredo, L. M. (2016). Trypanosoma brucei parasites occupy and functionally adapt to the adipose tissue in mice. *Cell Host Microbe*, *19*, 837–848. https://doi.org/10.1016/j.chom.2016.05.002

Varga, V., Moreira-Leite, F., Portman, N., & Gull, K. (2017). Protein diversity in discrete structures at the distal tip of the trypanosome flagellum. *Proceedings of the National Academy of Sciences*. https://doi.org/10.1073/pnas.1703553114

Vaughan, S., & Gull, K. (2008). The structural mechanics of cell division in Trypanosoma brucei. *Biochemical Society Transactions*, *36*(3), 421–424. https://doi.org/10.1042/BST0360421

Vesteg, M., Hadariová, L., Horváth, A., Estraño, C. E., Schwartzbach, S. D., & Krajčovič, J. (2019). Comparative molecular cell biology of phototrophic euglenids and parasitic trypanosomatids sheds light on the ancestor of Euglenozoa. *Biological Review*, 000–000. https://doi.org/10.1111/brv.12523

Vincensini, L., Blisnick, T., Bertiaux, E., Hutchinson, S., Georgikou, C., Ooi, C. P., & Bastin, P. (2018). Flagellar incorporation of proteins follows at least two different routes in trypanosomes. *Biology of the Cell*, *110*(2), 33–47. https://doi.org/10.1111/boc.201700052

Wallmeier, J., Al-Mutairi, D. A., Chen, C. T., Loges, N. T., Pennekamp, P., Menchen, T., … Omran, H. (2014). Mutations in CCNO result in congenital mucociliary clearance disorder with reduced generation of multiple motile cilia. *Nature Genetics*, *46*(6), 646–651. https://doi.org/10.1038/ng.2961

Wang, J., & Barr, M. M. (2018). Cell-cell communication via ciliary extracellular vesicles: clues from model systems. *Essays Biochem*, *62*, 205–213.

Wanner, A., Salathe, M., & Riordan, T. G. O. (1996). Mucociliary clearance in the airways. *Am. J. Respir. Crit. Care Med.*, (154), 1868–1902.

Wheway, G., Nazlamova, L., & Hancock, J. T. (2018). Signaling through the Primary Cilium. *Frontiers in Cell and Developmental Biology*, *6*(February), 1–13. https://doi.org/10.3389/fcell.2018.00008

Wickstead, B., & Gull, K. (2007). Dyneins across eukaryotes: A comparative genomic analysis. *Traffic*, *8*(12), 1708–1721. https://doi.org/10.1111/j.1600-0854.2007.00646.x

Winet, H. (1980). On the mechanism for flow in the efferent ducts. *Journal of Andrology*, *1*(6), 304–311. https://doi.org/10.1002/j.1939-4640.1980.tb00046.x

Wren, K. N., Craft, J. M., Tritschler, D., Schauer, A., Patel, D. K., Smith, E. F., … Lechtreck, K. . (2013). A differential cargo loading model of ciliary length regulation by IFT. *Curr. Biol.*, *23*(24), 2463–2471. https://doi.org/10.1016/j.cub.2013.10.044. A

Xia, W., Zhang, D., Ouyang, J., Liang, Y., Zhang, H., Huang, Z., … Zhang, J. (2018). Effects of pelvic endometriosis and adenomyosis on ciliary beat frequency and muscular contractions in the human fallopian tube. *Reproductive Biology and Endocrinology*, *16*(1). https://doi.org/10.1186/s12958-018-0361-y

Yanagisawa, H. -a., Mathis, G., Oda, T., Hirono, M., Richey, E. A., Ishikawa, H., … Qin, H. (2014). FAP20 is an inner junction protein of doublet microtubules essential for both the planar asymmetrical

waveform and stability of flagella in Chlamydomonas. *Molecular Biology of the Cell*, *25*(9), 1472–1483. https://doi.org/10.1091/mbc.E13-08-0464

Yang, P., Diener, D. R., Yang, C., Kohno, T., Pazour, G. J., Dienes, J. M., … Witman, G. B. (2006). Radial spoke proteins of Chlamydomonas flagella. *Journal of Cell Science*, *119*(6), 1165–1174. https://doi.org/10.1242/jcs.02811

Yeung, C. H., Cooper, T. G., Bergmann, M., & Schulze, H. (1991). Organization of tubules in the human caput epididymidis and the ultrastructure of their epithelia. *American Journal of Anatomy*, *191*(3), 261–279. https://doi.org/10.1002/aja.1001910306

Zhu, X., Liu, Y., & Yang, P. (2017). Radial spokes—a snapshot of the motility regulation, assembly, and evolution of cilia and flagella. *Cold Spring Harbor Perspectives in Biology*, *9*(5), 1–14. https://doi.org/10.1101/cshperspect.a028126

Supplementary Data

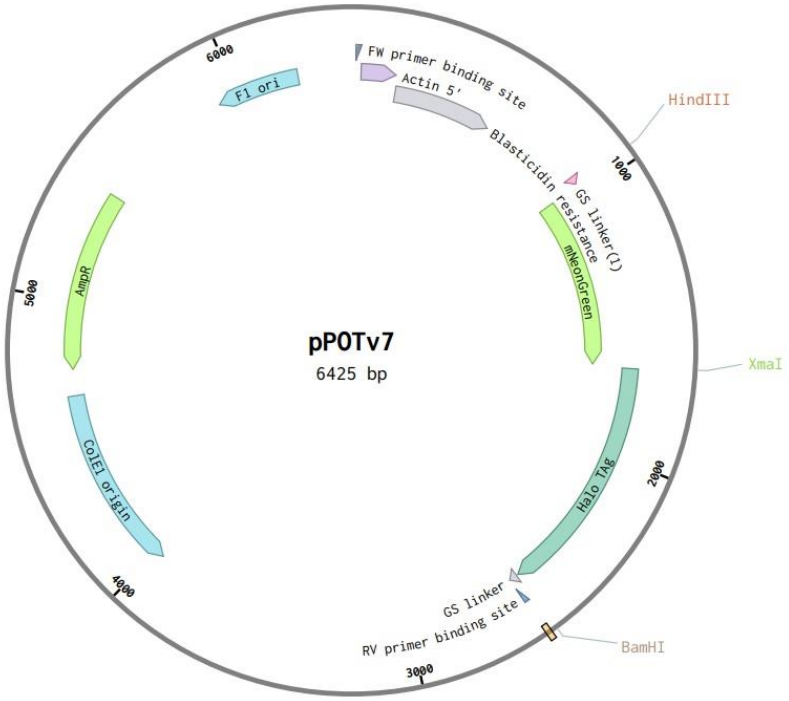

Supplementary Figure 9.1. General constitution of pPOT vector.

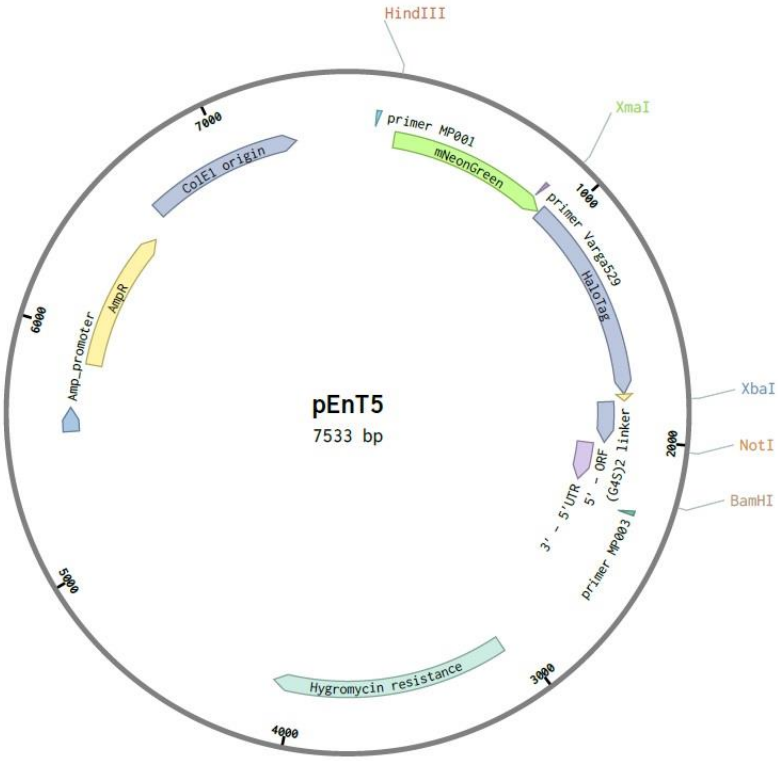

Supplementary Figure 9.2. General constitution of pEnT5 vector

Supplementary Table 9.1. List of generated *T. brucei* cell lines and their specifications; N = N-terminal, C = C-terminal

#	Protein name	Gene DB accession number	Tag position	Cell line specification (vector and tag)
1	RSP4/6	**Tb927.11.4480**	N	pPOTv4-mNG-HaloTag::
2	RSP4/6	**Tb927.11.4480**	N	pPOTv4-mNG-HaloTag:: RNAi by pQuadra
3	RSP4/6	**Tb927.11.4480**	N	pPOTv7-TCtag-mNG::
4	RSP2	**Tb927.5.2850**	N	pPOTv7-mNG-HaloTag::
5	RSP3	**Tb927.11.1150**	N	pPOTv4-mNG-HaloTag::
6	RSP3	**Tb927.11.1150**	N	pPOTv4-mNG-HaloTag:: RNAi by pQuadra
7	IAD	**Tb927.4.870**	N	pEnT5-mNG-HaloTag::
8	OAD2	**Tb927.3.930**	N	pEnT5-mNG-HaloTag::
9	OAD2	**Tb927.3.930**	N	pEnT5-HaloTag::
10	PF16	**Tb927.1.2670**	N	pPOTv7-mNG-HaloTag::
11	PF20	**Tb927.10.13960**	N	pEnT5-mNG-HaloTag::
12	FAP20	**Tb927.10.2190**	N	pEnT5-mNG-HaloTag::
13	FCP4/TbKin15	**Tb927.10.890**	N	pEnT5-mNG-HaloTag::
14	DRC4	**Tb927.9.15050**	N	pPOTv7-mNG-HaloTag::
15	DCR2	**Tb927.11.7240**	C	::mNG-HaloTag-pPOTv7
16	PFR2-2	**Tb927.8.4980**	N	pEnT5-mNG-HaloTag::
17	Rib72	**Tb927.10.7690**	N	pEnT5-mNG-HaloTag::
18	Rib72	**Tb927.10.7690**	N	pPOTv7-TCtag-mNG::
19	ACS1	**Tb927.7.6180**	N	pEnT5-mNG-HaloTag::
20	αtubulin	**Tb927.1.2360**	N	pEnT5-mNG-HaloTag::
21	αtubulin	**Tb927.1.2360**	N	pEnT5-HaloTag::
22	αtubulin	**Tb927.1.2360**	N	pPOTv7-TCtag::
23	Hydin	**Tb927.6.3150**	N	pEnT5-mNG-HaloTag::
24	CFAP43	**Tb927.4.5380**	N	pPOTv7-mNG-HaloTag::

Supplementary Table 9.2. pPOT tagging primers; FW = forward, RV = reverse, ORF = open reading frame, UTR = untranslated region

Oligonucleotide name	Gene of interest	Gene ID	Starting position	FW/RV	Sequence (5' to 3')	Length (nt)	Annealing temperature
Varga519	**Tb927.11.4480**	A	_80nt of 5'UTR	FW	**GTGAAGTGGAGGTGGAAAGGAGAGCCAGTTGGAGAGAAAAACCACGTACACAAGTTTTACAGAATAAATCAAGGTCAGATgtataatgcagacctgctgc**	100	63°C
Varga520	**Tb927.11.4480**	A	1nt of ORF	RV	**TCCTTATTCGCGCACATGAGATATGCCTTTGTCCTTGCGAACATCGCCTCAAGATCCTGTGGTTCAGGATTTACTGGCATactacccgatcctgatcc**	98	63°C
MP025	**Tb927.5.2850**	B	_80nt of 5'UTR	FW	**ATTATTGACTATAGCTTTTGTTTCTTTTCTTTCCACTCTTTTTTTTTGTATTTCTGAATCGAGTAGAAACAAGAAACTAAgtataatgcagacctgctgc**	100	63°C
MP026	**Tb927.5.2850**	B	1nt of ORF	RV	**GGTTGAGCAAGAACTGTTTCAGCGACGGCTTTCGCAAGCACAGGACCAACACTGCATTTGAGGTATGCACTCTCAGTCATactacccgatcctgatcc**	98	63°C
Varga521	**Tb927.11.1150**	C	_80nt of 5'UTR	FW	**AAAAAAAGAGGAAAAGAAGAGGGCGAAAGAAGAGTCAAAATAAACAATCAAGATATTGGTGGTAGAAAGTGTTTTGAATCgtataatgcagacctgctgc**	100	63°C
Varga522	**Tb927.11.1150**	C	1nt of ORF	RV	**GCGTGTAAGAACCCCTGTGGTGGGTGCTGAAAGGTGTAGGCCATAGTGCCATCCACTGCTGCTTGGTTTTGCCCTTGCATactacccgatcctgatcc**	98	63°C
TT09	**Tb927.1.2670**	G	_80nt of 5'UTR	FW	**GGGCGGAAGATTCTTCTTTTCCCTTTTTATCTAAGAGCAGGAAAAAGAATTTTTAAAAAAAAAAAAAACTATCACATCACAgtataatgcagacctgctgc**	100	63°C
TT10	**Tb927.1.2670**	G	1nt of ORF	RV	**AAATCTGCCACCGTCTGTACAAACTTGACACGGGCCCTTTGGTATTCCTCAAATACCTGAATGATCTGCCTGTTGGGCATactacccgatcctgatcc**	98	63°C
TT33	**Tb927.9.15050**	M	_80nt of 5'UTR	FW	**GGCCATCCTCTCCATTCCCTTCTCCCCCTTTCTTTCACTTAGTTTAGTCGTTTCCTTTCTTTGGAAGCCACCATTGGTTGgtataatgcagacctgctgc**	100	63°C
TT34	**Tb927.9.15050**	M	1nt of ORF	RV	**TCAGGTGCCTGCTTCTTCCCCTTCCCACCCTTTCCTGATCCCTTGGCCTTCGCTGCCGCTGCTTCCTTCTTTGGTGGCATactacccgatcctgatcc**	98	63°C
TT35	**Tb927.11.7240**	N	1442nt of ORF	FW	**CTGGGCGCGGGGCTACTGGCGGAAGACGTGAGTACACGACAGCGATAGAGGGCAACAAGTTCGTCTCCGACATGACGAGGggttctggtagtggttcc**	98	62°C
TT36	**Tb927.11.7240**	N	1443nt of 3'UTR	RV	**TAAACTCTACATTGCCATTTCCCCATATTGCTTAAAGGAGGAAACGATGAAAAGTGTGCTCATACCCCAACAGGAATTGCccaatttgagagacctgtgc**	100	63°C
Varga525	**Tb927.10.7690**	R	_80nt of 5'UTR	FW	**TGCACTTTATTTTGCTTTGTCCCAATGCTGCATTTATAAGGGCTGAGTGACGGCAGGAGCAACGGCGCGCTTCCACACTAgtataatgcagacctgctgc**	100	63°C
Varga526	**Tb927.10.7690**	R	1nt of ORF	RV	**TTAGTTGGGGGTGGGTTAAGCTCAGGGAAACTAAACCCCGGAAGCTTGGGGAGTGCATCATAAATGGTCCGGTCCGTCATactacccgatcctgatcc**	98	63°C
TT62	**Tb927.1.2360**	T	_80nt of 5'UTR	FW	**GACTATTCATCCGTTTATATTAGCAACAGTAGGTACTAGCACCACTAACAACAACAACAAAGCACTTCTATTTATTTATCgtataatgcagacctgctgc**	100	63°C
TT63	**Tb927.1.2360**	T	1nt of ORF	RV	**TCCAGGCAGAACAATTCCCAGCAGGCGTTACCAACCTGGCAACCAGCCTGACCAATGTGGATGCAGATAGCCTCACGCATactacccgatcctgatcc**	98	63°C
MP027	**Tb927.4.5380**	43	_80nt of 5'UTR	FW	**TAAACTTTCGTTGTTGCTCCATCCGCGCGCTCCGTGCCAAACATTATAGGGTATTATTACGCAGTGTACTTTTATATTAGgtataatgcagacctgctgc**	100	63°C
MP028	**Tb927.4.5380**	43	1nt of ORF	RV	**GCTCCTAGGAGAAAGTCGTCACCCGCAGCGACGAGAGCAGAGGGAGAGTTGAACCCTAGAATGCGCGCGTTGGTTGCCATactacccgatcctgatcc**	98	63°C

Supplementary Table 9.3. pEnT5 tagging primers; FW = forward, RV = reverse, ORF = open reading frame, UTR = untranslated region

Oligonucleotide name	Gene of interest	Gene ID	Starting position	FW/RV	Sequence (5' to 3')	Length (nt)	Annealing temperature
Varga538	**Tb927.3.930**	F	4nt of ORF	FW	**ACTGTCTAGAAAGGCAGTTCAGAGGGTG**	28	65°C
Varga539	**Tb927.3.930**	F	251nt of ORF	RV	**CAGTGCGGCCGCTTCTGCGGATTCACAACAC**	31	63°C
Varga540	**Tb927.3.930**	F	-263nt of 5'UTR	FW	**ACTGGCGGCCGCgcgctacagcatatttgcg**	31	65°C
Varga541	**Tb927.3.930**	F	-46nt of 5'UTR	RV	**CAGTGGATCCcaggaacactccaagctgc**	29	66°C
MP004	**Tb927.1.2670**	G	4nt of ORF	FW	**ACTGTCTAGACCCAACAGGCAGATCATTC**	29	63°C
MP005	**Tb927.1.2670**	G	195nt of ORF	RV	**CAGTGCGGCCGCGTAATTGGCAAGCCTTCCC**	31	64°C
MP006	**Tb927.1.2670**	G	-321nt of 5'UTR	FW	**ACTGGCGGCCGCAGATAGACACGTAAAGAag**	31	52°C
MP007	**Tb927.1.2670**	G	-38nt of 5'UTR	RV	**CAGTGGATCCttcctgctcttagataa**	27	52°C
MP008	**Tb927.10.13960**	H	4nt of ORF	FW	**ACTGTCTAGAGCGCAGGTCGGCGAGGTTT**	29	74°C
MP009	**Tb927.10.13960**	H	252nt of ORF	RV	**CAGTGCGGCCGCGGTTCGGTGCATTCCATTCCGAAG**	36	71°C
MP010	**Tb927.10.13960**	H	-258nt of 5'UTR	FW	**ACTGGCGGCCGCCCTTACTTACTCCACAGCT**	31	61°C
MP011	**Tb927.10.13960**	H	-29nt of 5'UTR	RV	**CAGTGGATCCGGGCGGCACTAATTCTAC**	28	63°C
MP012	**Tb927.10.7690**	R	4nt of ORF	FW	**ACTGTCTAGAACGGACCGGACCATTTATG**	29	65°C
MP013	**Tb927.10.7690**	R	252nt of ORF	RV	**CAGTGCGGCCGCAGAGCCTTATCGTCCAGTGA**	32	65°C
MP014	**Tb927.10.7690**	R	-191nt of 5'UTR	FW	**ACTGGCGGCCGCGCGCGCTTAACGTACGACA**	31	68°C
MP015	**Tb927.10.7690**	R	-1n of 5'UTR	RV	**CAGTGGATCCTAGTGTGGAAGCGCGCCG**	28	71°C
MP016	**Tb927.4.870**	E	4nt of ORF	FW	**ACTGTCTAGAAACGGGAATGAAGAGATG**	28	59°C
MP017	**Tb927.4.870**	E	165nt of ORF	RV	**CAGTGCGGCCGCTGTGACAGCAATGAATGAC**	31	60°C
MP018	**Tb927.4.870**	E	-244nt of 5'UTR	FW	**ACTGGCGGCCGCGGAGATGGAACCGTTGAG**	30	62°C
MP019	**Tb927.4.870**	E	-56nt of 5'UTR	RV	**CAGTGGATCCACCAACGCGATTGTTTCA**	28	62°C
MP020	**Tb927.8.4980**	P	4nt of ORF	FW	**ACTGTCTAGAAGCGGAAAGGAAGTTGAAGGT**	31	67°C
MP021	**Tb927.8.4980**	P	222nt of ORF	RV	**CAGTGCGGCCGCGGCAAGCAATTCATGCGCT**	31	67°C
MP022	**Tb927.8.4980**	P	-261nt of 5'UTR	FW	**ACTGGCGGCCGCTATCCTTCGGCATTAGAGA**	31	59°C
MP023	**Tb927.8.4980**	P	-1nt of 5'UTR	RV	**CAGTGGATCCTGATGCTTTATTGCTTTCTC**	30	57°C
MP031	**Tb927.10.2190**	J	4nt of ORF	FW	**ACTGTCTAGATTCCACAACAGTTACCA**	27	57°C
MP032	**Tb927.10.2190**	J	205nt of ORF	RV	**CAGTGCGGCCGCGGAAGCTTAATACCAAG**	29	57°C
MP033	**Tb927.10.2190**	J	-218nt of 5'UTR	FW	**ACTGGCGGCCGCcacgtatatcaaagaaggg**	31	61°C
MP034	**Tb927.10.2190**	J	-1nt of 5'UTR	RV	**CAGTGGATCCatgttggacctttcgagt**	29	58°C
MP035	**Tb927.6.3150**	Y	4nt of ORF	FW	**ACTGTCTAGACCCGTAAAGCAACCGC**	26	64°C
MP036	**Tb927.6.3150**	Y	189nt of ORF	RV	**AGTGCGGCCGCTAAGGGCAACTTCATAGCTT**	31	61°C
MP037	**Tb927.6.3150**	Y	-166nt of 5'UTR	FW	**ACTGGCGGCCGCCTCCCGGTTGTTGGCG**	28	67°C
MP038	**Tb927.6.3150**	Y	-1nt of 5'UTR	RV	**CAGTGGATCCGGTTGTTGTTCCTACTCTACTCC**	33	64°C

Supplementary Table 9.4. Tagging validation primers; FW = forward, RV = reverse

Oligonucleotide name	Gene of interest	Gene ID	Starting position	FW/RV	Sequence (5' to 3')	Length (nt)	Annealing temperature
Varga529	**mNeonGreen**	mNG	653nt of mNG	FW	**AAGAGTGGCAGAAGGCG**	17	58°C
MP039	**Tb927.11.4480**	A	335nt of gene	RV	**GGCTGTTCTATGGTAGTCTGGAT**	23	59°C
MP040	**Tb927.5.2850**	B	420nt of gene	RV	**AGCAGCTGCATCATCGACAT**	20	61°C
MP041	**Tb927.11.1150**	C	297nt of gene	RV	**TTGGGCTGCGTCAAGTTCTT**	20	61°C
MP042	**Tb927.4.870**	E	811nt of gene	RV	**GTGGATCAAGGGACATAGCCA**	21	60°C
MP043	**Tb927.3.930**	F	707nt of gene	RV	**TGCACCACGTCATAGACAGC**	20	61°C
MP044	**Tb927.1.2670**	G	453nt of gene	RV	**CACATAACCCAACGCCCATAC**	20	60°C
MP045	**Tb927.10.13960**	H	364nt of gene	RV	**CGTCGATTCGATTGTGGAGTG**	21	59°C
MP046	**Tb927.10.2190**	J	475nt of gene	RV	**AGTTCGCATGAAGTTGCACG**	20	60°C
MP047	**Tb927.10.890**	K	479nt of gene	RV	**TCTTCCACTACTCGCGGTAC**	20	60°C
MP048	**Tb927.9.15050**	M	372nt of gene	RV	**ACTTGTCATTTCAGCCAGTTGC**	22	59°C
MP049	**Tb927.8.4980**	P	460nt of gene	RV	**CGATGGCATTGTCGATCATGC**	21	60°C
MP050	**Tb927.10.7690**	R	576nt of gene	RV	**GAAGGTGTCACTCGGATAGTC**	21	58°C
MP051	**Tb927.7.6180**	S	391nt of gene	RV	**GATCAACTAGCAGATGGCAGTC**	22	59°C
MP052	**Tb927.1.2360**	T	350nt of gene	RV	**CAGAGGTCGACGATCTCCTTAC**	22	60°C
MP053	**Tb927.6.3150**	Y	746nt of gene	RV	**GACAATTCCATTGCACTACCCGA**	23	61°C
MP054	**Tb927.4.5380**	c43	467nt of gene	RV	**GCTATACAGTCATGCCGATGC**	21	59°C
MP055	**Tb927.11.7240**	N	357nt of gene	FW	**GATGCAGGAAGGCCAAGTGA**	22	61°C
MP024	**mNeonGreen**	mNG	248nt of mNG	RV	**GTCCACCATAGCTGCTTGGA**	20	61°C

Supplementary Table 9.5. RNAi target primers; FW = forward, RV = reverse

Oligonucleotide name	Gene of interest	Gene ID	Starting position	FW/RV	Sequence (5' to 3')	Length (nt)	Annealing temperature
HV69	**Tb927.11.1150**	C	140nt	FW	**atcataccaatgtgatggACCGTCGTGTGTATCGCG**	36	58°C
HV70	**Tb927.11.1150**	C	925nt	RV	**atcataccatagagttggCGCCCGCTGCTTCTTTTC**	36	58°C
HV71	**Tb927.11.4480**	A	63nt	FW	**atcataccaatgtgatggATGTGCGCGAATAAGGACGG**	38	59°C
HV72	**Tb927.11.4480**	A	1043nt	RV	**atcataccatagagttggCCACTGCGTTACATCACTCT**	38	56°C

Supplementary Table 9.6. List of primer used for sequencing; FW = forward, RV = reverse, ORF = open reading frame, UTR = untranslated region, - = upstream, + = downstream

Oligonucleotide name	FW/RV	Sequence (5' to 3')	Length (nt)	Annealing temperature (°C)	Specifications
Varga529	FW	**AAGAGTGGCAGAAGGCG**	17	58	starts n653 of mNeonGreen
Varga530	RV	**AGGTCTGGAGCAATACAGC**	19	57	starts n176 of HaloTag
MP001	FW	**GCGATAGCTTAGCTATCAGC**	20	55	pEnT5 starts n-67 mNG
MP002	RV	**ACCATCGGGTTGAATGC**	17	55	tubulin only
MP003	RV	**TGTGCCATCAGATTACTCC**	19	54	pEnT5 starts n+62 UTR
MP061	RV	**CGTCAGATGTGCAAGCG**	17	64	CFAP43 identification

Supplementary Table 9.7. List of primers used for cloning; FW = forward, RV = reverse

Oligonucleotide name	FW/RV	Sequence (5' to 3')	Length (nt)	Annealing temperature (°C)	Specifications
Varga527	FW	**ATCGAAGCTTATGGTCTCGAAAGGTGAGGAAGACA**	35	65°C	pPotV4 insert mNG-Halo for cloning into pEnT5
Varga533	RV	**CAGTTCTAGATGATCCTCCTCCTCCTGATCCTCCTCCTCCACCAGAAATTTCAAGTGTCGAAAG**	64	62°C	pPotV4 insert mNG-Halo for cloning into pEnT5
Varga534	FW	**ATCGAAGCTTATGTCGGCTGAGATTGGTACG**	31	63°C	insert HaloTag for cloning into pEnT5
MP056	FW	**CATGTGCTGCCCAGGGTGTTGCG**	23	//	TC tag preparation
MP057	RV	**GATCCGCAACACCCTGGGCAGCACATGGTAC**	31	//	TC tag preparation

Supplementary Table 9.8. List of reagents

Chemical	manufacturer	catalogue number
Acetic acid	P-lab	--
Acrylamide/BIS-Acrylamide 30% sol.	Sigma	K15101
Agarose	Sigma	A3699-100ml
Ammonium persulfate (APS)	Sigma	A9539-500G
BAL buffer	Molecular probes	A3678-100 g
Bromphenol Blue	Sigma	--
Calcium Chloride (CaCl2)	P-lab	114391-5G
DAPI	Sigma	Q10102
Deoxynucleotide mix 10mM	Sigma	D9542-10MG
ddH_2O = double-distilled water	special water tap	D7295-20X.2ML
DMSO = dimethyl sulfoxide	P-lab	--
E-64-d = Calpain and cathepsin inhibitor	Enzo Life Sciences	D 06101
EDTA = Ethylendiaminetetraacetic acid	P-lab	BML-PI107
EGTA = Ethylene-bis (oxyethylenenitrilo)tetraacetic acid	P-lab	Q19101
Ethanol absolute	VWR	R30542
Fetal Bovine Serum (FBS)	Gibco	20816
Glycerol Glycerol anhydrous G.R.	Lachner	--
Haemin	Sigma	40058-AT0
HaloTag® Biotin Ligand	Promega	H9039-1G
HaloTag® Coumarin Ligand	Promega	G8282
HaloTag® PEG-Biotin Ligand	Promega	G8582
HaloTag® TMR direct Ligand	Promega	G8592
HCl = Hydrochloric acid	Lachner	G8252
Hepes	P-lab	10033-A35
Hoechst 33342 Solution (20 mM)	Thermo Fisher	R91054
Igepal CA630	Sigma	62249
Immersion oil Immersol 518 F - fluorescence free	Carl Zeiss spol. s r.o.	I3021-50ml
KCl = Potassium chloride	P-lab	444960-0000-000
KOH = Potassium hydroxide	P-lab	Q04101
LB = Lysogeny Broth (přípravna médií IMG) core facility at IMG		H 14102
Leupeptin hemisulfate salt	Sigma	--
MetOH = Methanol	Lachner	--
NaCl = Sodium chloride	Lachner	20038-AT0
NaH_2PO_4 = Sodium Dihydrogen Phosphate Dihydrate		30093-AP0
Na2HPO4 = Disodium Hydrogen Phosphate Dodecahydrate	P-lab	R.T879.2
Pepstatin A	Sigma	H08102
Phosphate Buffer Saline = PBS	media facility at IMG, CAS, CR	P5318-25MG
PIPES = piperazine-N,N'-bis (2-ethanesulfonic acid)	P-lab	--
PMSF = phenylmethylsulfonyl fluoride	Roche	R91564
ReAsH dye	Molecular Probes	10837091001
RedSafe™ Nucleic Acid Staining Solution	iNtRON	--
Powdered Milk	P-lab	--
SDM79 Powder	(Gibco®)	R.T145.2
SDM-79 cGMP DPM (5L)	life technologies –gibco	
SDS = Sodium dodecyl sulphate		2-07490916 N
Sodium bicarbonate ($NaHCO_3$)	Sigma	--
Sodium hydroxide (NaOH)	Mach chemikálie spol. s.r.o.	S5761-500G
Sulfuric acid 96% (H2SO4) p.a.	P-lab	--
Trizma base (Tris)	Sigma	K18101
Tween 20		T1503-1KG